

MEASUREMENT OF THE NEWLY DEFINED “CONSTRAINED POLYMER
REGION” IN POLYMER CLAY NANOCOMPOSITES

THESIS

Presented to the Graduate Council
of Texas State University-San Marcos
in Partial Fulfillment
of the Requirement

for the Degree

Master of SCIENCE

by

Daniel Adame, B.S.

San Marcos, Texas
December 2006

To Erika

ACKNOWLEDGEMENTS

I would first like to acknowledge the creator, our Lord, who has and will eternally surround me with divine love.

This work is not entirely the work of one individual, but of many, in particular the author owes a debt of gratitude to Dr. Gary W. Beall for his guidance in directing and supporting this master's research and essay. In addition I am grateful to the committee members; Dr. Chad J. Booth and Dr. Heather C. Galloway for offering many valuable suggestions and improvements for the completion of this work.

I thank my friends for understanding the meaning of their definition and for always being there, in times of sorrow and in times of bliss. David Adame, Mark Miller, Andrew Carroll, and Sergio Crosby, you hold a large place in my heart. Jeremy Bartels, Jesse Hancock, Phil Goodman, Eric Bierschenk, and Maheedhar Guntapalli, I could not have asked for better friends to have worked with in the laboratory.

My family has taught me the benefits of self-sacrifice, hard work, and faith in God. Their unconditional love was the driving force toward my success. I thank my entire family for their love, kindness, and support.

I wish to express my deepest appreciation to Erika Kay Lugo, for her unconditional love and support. You have filled my life with a joy I would not have otherwise known. You have convinced me of my worth. Thank you for inspiring me and believing in me. I will always love you.

This manuscript was submitted on 1, September 2006.

TABLE OF CONTENTS

	Page
ACKNOWLEDGEMENTS.....	iv
LIST OF TABLES.....	viii
LIST OF FIGURES	ix
ABSTRACT.....	xi
CHAPTER 1	
1. INTRODUCTION	1
1.1 Background.....	1
1.1.1 Barrier Properties.....	2
1.2 Polymer Layered Silicates	3
1.2.1 Montmorillonite.....	4
1.2.2 Cation Exchange Character of Montmorillonite.....	5
1.2.3 Formation of Polymer Clay Systems	7
1.3 Tortuous Pathway	9
1.4 Conceptual Model.....	11
1.5 Analysis.....	13
CHAPTER 2	
2. EXPERIMENTAL.....	14
2.1 Materials	14
2.2 Organoclay Formation	15

2.3	Extrusion of Nylon 6 PLS Nanocomposite.....	15
2.3.1	Nylon 6 PLS Nanocomposite Monofilament Formation	16
2.3.2	Nylon 6 PLS Nanocomposite Film Formation	17
2.4	Extrusion of Nylon-MXD6 PLS Nanocomposite.....	18
2.4.1	Nylon-MXD6 PLS Nanocomposite Monofilament Formation	18
2.4.2	Nylon-MXD6 PLS Nanocomposite Film Formation.....	18
2.5	Characterization Techniques.....	19
2.5.1	Thermogravimetric Analysis	19
2.5.2	X-ray Diffraction	19
2.5.3	Atomic Force Microscopy	20

CHAPTER 3

3.	RESULTS AND DISCUSSION.....	22
3.1	Monofilaments and Films Visual Appearance	22
3.2	Thermogravimetric Analysis	22
3.2.1	TGA of Nylon 6 and Nanocomposites.....	23
3.2.2	TGA of Nylon-MXD6 and Nanocomposites.....	25
3.2.3	Experimental Clay Loadings.....	27
3.3	X-ray Diffraction	27
3.3.1	X-ray Diffraction of Nylon 6 and Nanocomposties.....	28
3.3.2	X-ray Diffraction of Nylon-MXD6 and Nanocomposties	31
3.4	Atomic Force Microscopy	32
3.4.1	AFM Analysis of Nylon-MXD6 PCNs.....	33
3.4.2	AFM Analysis of Nylon 6 PCNs	35

3.4.3	Constrained Polymer Region	36
CHAPTER 4		
4.	CONCLUSION.....	40
APPENDICES		42
APPENDIX 1: X-ray Diffraction.....		43
APPENDIX 2: Atomic Force Microscopy Analysis		48
REFERENCES		97

LIST OF TABLES

	Page
Table 1. Experimental Materials.....	14
Table 2. Temperature and RPM Parameters for Extruding Nylon 6 Nanocomposites into Monofilaments.....	16
Table 3. Temperature and RPM Parameters for Extruding Nylon 6 Nanocomposites into Thin Films.....	17
Table 4. Temperature and RPM Parameters for Extruding Nylon-MXD6 Nanocomposites into Monofilaments	18
Table 5. Temperature and RPM Parameters for Extruding Nylon-MXD6 Nanocomposites into Thin Films	19
Table 6. Standard and Modified Embedding Formulations.....	20
Table 7. TGA Results of Nylon 6 and PCNs	24
Table 8. TGA Results of Nylon-MXD6 and PCNs	26
Table 9. Theoretical Clay Distances in an Oriented-Exfoliated PCN	33
Table 10. Constrained Polymer Region at Time 2 Hours for Nylon-MXD6 at 0.5 % Clay Loading.....	37
Table 11. Constrained Polymer Region at Time 2 Hours for Nylon-MXD6 at 2 % Clay Loading.....	38
Table 12. Constrained Polymer Region at Time 2 Hours for Nylon-MXD6 at 5 % Clay Loading.....	38
Table 13. Constrained Polymer Region at Time 2 Hours for Nylon 6 at 2 % Clay Loading	38

LIST OF FIGURES

	Page
Figure 1. Structure of Montmorillonite : 2 Tetrahedral Sheets Surrounding a Central Octahedral Sheet.....	5
Figure 2. Dimensions of Montmorillonite	5
Figure 3. Ions Balance the Negative Charge on the Surface of Montmorillonite.....	6
Figure 4. Cation Exchange of Alkylammonium Ions for Sodium Cations.....	7
Figure 5. Melt Compounding Intercalation Process	8
Figure 6. Intercalated and Exfoliated Polymer Layered Silicate Nanocomposite	9
Figure 7. Tortuous Pathway in PLS Nanocomposites	10
Figure 8. Thermogravimetric Analysis of Nylon 6.....	23
Figure 9. TGA Overlay of Nylon 6 and PCNs.....	24
Figure 10. Thermogravimetric Analysis of Nylon-MXD6.	25
Figure 11. TGA Overlay of Nylon-MXD6 and PCNs.....	26
Figure 12. SEM Image of Etched Nylon 6 (top) and Nylon-MXD6 (bottom) at 5 % Clay Loading	28
Figure 13. X-ray Diffraction Data of Nylon 6 and Nanocomposites.....	30
Figure 14. Conformational Crystal Structures of Nylon 6.....	31
Figure 15. X-ray Diffraction Data of Nylon-MXD6 and Nanocomposites.	32
Figure 16. Typical Topographical Surface Measurements for all PCNs.	39
Figure 17. Typical Topographical Surface Measurements for the Constrained Polymer Region	39

Figure 18. Increase of Topographical Features with an Increase in Clay Loading ... 40

ABSTRACT

MEASUREMENT OF THE NEWLY DEFINED “CONSTRAINED POLYMER REGION” IN POLYMER CLAY NANOCOMPOSITES

by

Daniel Adame, B.S.

Texas State University-San Marcos

December 2006

SUPERVISING PROFESSOR: GARY W. BEALL

Measurements on two exfoliated polymer-clay nanocomposites systems, Nylon 6 and Nylon-MXD6, were conducted to determine the size of the constrained polymer regions. Analysis performed through Atomic Force Microscopy established that the range fell in agreement with speculated values proposed by Beall, which extend 50 – 100 nm away from the surface of the clay. With an increase in clay loading, topographical hills and valleys became more frequent for a given area. In higher clay loaded samples the clay plates were closer to each other and as a result the frequency of hills and valleys were higher than on those of the lower clay loaded PCNs. Experimentally measured distances between clay plates were in reasonable agreement with the expected values. In systems with lower clay loading, the distances between clay plates were higher. Lower

distances between clay plates were seen in systems with higher clay contents. The swelling behavior of the studied PCNs is attributed to their crystalline makeup along with H-bonding. The addition of clay turns the amorphous Nylon-MXD6 polymer into one with a pseudo-crystalline character. This crystalline behavior is observed in areas which are in close proximity to the surface of the clay, the constrained polymer region. When comparing the unconstrained to the constrained polymer region of Nylon-MXD6, a decrease in free volume is observed in the areas which act crystalline. As a result the swelling effect caused by the solvent is amplified in the areas in which clay is absent, the unconstrained polymer region. The distinct amplitude of hills and valleys of Nylon-MXD6 was a result of a transition from a crystalline domain to an amorphous one. The swelling imparted by the solvent on Nylon 6, already in a crystalline state, was more uniform. The topographical relief on the surface was significantly lower than those on Nylon-MXD6. In Nylon 6 the transition was between two crystalline forms and therefore the swelling amplitude for both areas acted quite similarly.

CHAPTER 1

INTRODUCTION

1.1 Background

The incorporation of nanotechnology for improving the physical and mechanical properties of polymers has become an emerging trend in polymer chemistry. The addition of nano-fillers to polymeric materials significantly increases modulus and strength, increases solvent and heat resistance, and decreases flammability and gas permeability.¹ The most commonly applied system incorporates organic polymers and inorganic smectic clay minerals that have been organically modified. The enhancements produced by these systems greatly depend on the large aspect ratio and large surface area of the clay mineral, the strong interactions between the polymer chains and layered silicate, and the nano-scale structure of the newly formed polymer “nanocomposite”.^{2,3} The nano-scale structure is normally divided into two types including intercalated and exfoliated. The exfoliated system is preferred since the optimum interaction between clay and polymer is observed.

Polymer clay interactions have been extensively studied since the mid-20th century.⁴ In 1974, Shepard proposed the first single layered aluminum silicate, mica, as an excellent candidate for the reinforcement of polymers.⁵ In Shepard’s study, the

properties of acrylonitrile butadiene styrene polymer, acrylonitrilestyrene polymer, and nylon 66 were improved by the addition of mica. These improvements included a higher modulus, comparable tensile strength, and lower impact strength than conventional reinforced polymers. This proposal was supported by mica's ideal nanometer thick single clay layer and high aspect ratio.

The first organoclay-polyamide nanocomposite hybrid was reported by Fujiwara and Sakamoto in 1976.⁶ Nylon clay systems were refined in the late 1980s by Toyota Central Research and Development Labs. In 1990 a major breakthrough was reported by Okada at Toyota Central R&D Labs, with the first in-situ polymerization of Nylon 6 nanocomposite.⁷ Toyota reported a doubling in the tensile modulus and strength with a clay loading of 4.7 %. These properties extended to relatively higher temperatures allowing for the application of the material such as a timing belt cover on the Toyota Camry. Later research on these systems would reveal improvements in many physical and mechanical properties.

1.1.1 Barrier Properties

Gas permeability rates are of great interest for food packaging. The food packaging industry is regularly searching for ways to reduce the gas permeability rate of packaging materials to extend the shelf life of products. The lower the gas permeability, the longer a product will stay fresh. Lowered gas permeability not only improves the shelf life of products, but it can open up many other applications, such as beer bottles to plastics where the escape of carbon dioxide is the issue rather than the ingress of oxygen. The addition of clay to a conventional polymer, thus creating a polymer-clay

nanocomposite (PCN), significantly lowers the gas permeation. This improvement in barrier performance depends strongly on the aspect ratio (the ratio between two dimensions of an object) of the “impermeable” dispersed clay filler. Increasing the aspect ratio increases the effective path length, of the permeant, to penetrate through the system. The gas permeability rates of polymer nanocomposites are reduced extensively at very low clay loading rates as low as 0.5 % by weight of the nanoparticles.

Current theories of gas diffusion through these nanocomposites assume a tortuous path around the clay particle. The increase in barrier performance of PCNs is correlated with the highly tortuous pathway that particles must travel through to permeate a film. The simple tortuous path model fails in many cases, as pointed out by Beall, and a more complex model was proposed that involved a constrained polymer effect.⁸ A better understanding of the tortuous pathway through PCNs is needed to properly predict diffusion characteristics. Predicting the diffusion characteristics of PCNs will greatly benefit consumers and the packaging industry.

1.2 Polymer Layered Silicates

Polymer layered silicates (PLS) have been observed to exhibit remarkable improvements on numerous physical properties. These improvements include flame resistance, improved tensile strength and modulus, and decreased gas permeability rates.^{9,10,11}

1.2.1 Montmorillonite

Smectite clays, like montmorillonite, $(\text{Na,Ca})_{0-33}(\text{Al,Mg})_2\text{Si}_4\text{O}_{10}(\text{OH})_2 n\text{H}_2\text{O}$, are composed of hydrated sodium calcium aluminum magnesium silicate hydroxide arranged in a monoclinic crystal system, see Figure 1.¹² Its structure was solved by Hofmann, Endell, and Wilm in 1933.^{13,14,15} Aluminum silicate clays have a sheet-like structure, and consist of two silica tetrahedra (SiO_4) layers bonded to a single alumina octahedron (AlO_6) layer. The basic building block of the aluminum silicate mineral is the silicon-oxygen tetrahedron. These tetrahedra form the backbone and other ions are accommodated based on their size. Smectite clays have a three-layer crystalline structure, a 2:1 tetrahedra to the octahedral expanding crystal lattice, with platelet dimensions of one nanometer in thickness in one dimension and 150 ~ 250 nanometers in the other two. Smectite clays are known to contain very high aspect ratios. When completely dispersed, these plates have a large surface area in the range of 700 – 800 m^2/g , allowing an enormous range, both in number and variety, to become intercalated with the clay sheets.¹⁶ The high surface area of the clay plate is responsible for increasing the mechanical properties of conventional polymers, see Figure 2.¹⁷

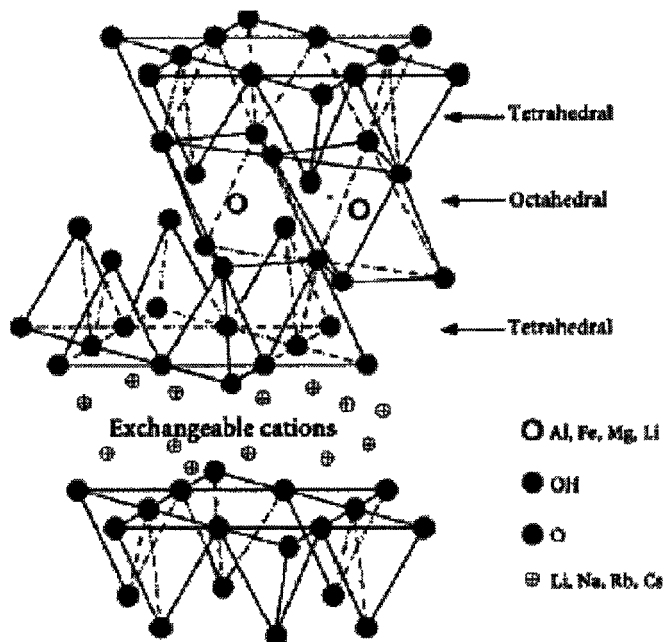


Figure 1. Structure of Montmorillonite: 2 Tetrahedral Sheets Surrounding a Central Octahedral Sheet.¹⁸

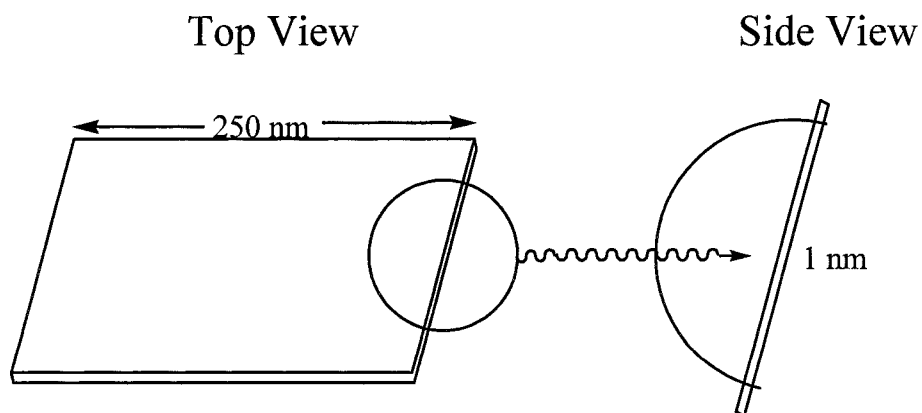


Figure 2. Dimensions of Montmorillonite.

1.2.2 Cation Exchange Character of Montmorillonite

In montmorillonite, isomorphous substitution in the tetrahedral lattice of aluminum and silicon [$\text{Si}_2\text{O}_4 \rightarrow \text{SiAlO}_4$] and in the octahedral lattice of magnesium and aluminum

$[(\text{OH})_2\text{Al}_2\text{O}_2 \rightarrow (\text{OH})_2\text{AlMgO}_2]$ results in a negative charge between layers. Cations like Na^+ and Ca^{2+} located in the interlayer galleries compensate the net negative charge on the surfaces of the silicate plates that generate from the oxide layers. This is depicted in Figure 3. The counter ions, embedded between the galleries, that hold the individual plates together via van der Waals forces form stacks of plates (10 - 20 plates) called tactoids. Water molecules are generally coordinated to the cations on the surface due to their relative high hydration energy. This makes the clay hydrophilic in nature and incompatible with most organic matrices. The surface must be treated before it can be processed into PCNs.

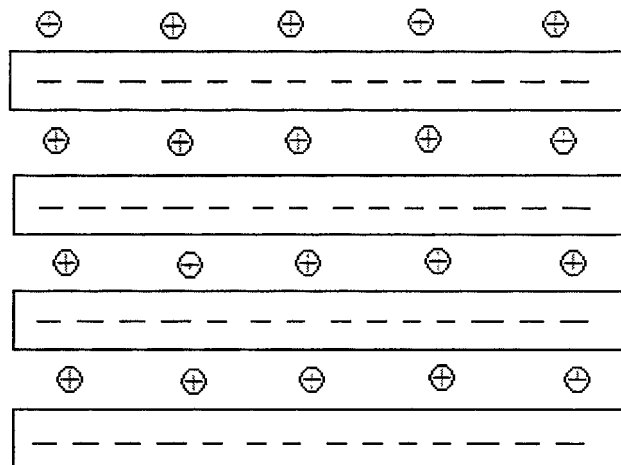


Figure 3. Ions Balance the Negative Charge on the Surface of Montmorillonite. The circles represent cations on the surface and the rectangles depict the clay platelets.

Montmorillonite as a mineral is unique in that it retains the cations at the surface in an exchangeable fashion. The cation exchange capacity for montmorillonite is between 80 and 150 milliequivalent per 100g, but varies from deposit to deposit.¹⁹ Ion-exchanging of the cations on the surface of the clay with organic onium ions renders the

clay hydrophobic (organophilic) and compatible with a wide array of organic matrices. This is done by exchanging the cations on the surface with a variety of positively charged species, most commonly by ion-exchanging reactions with primary, secondary, tertiary, and quaternary alkylammonium cations. Figure 4 depicts the exchange of the surface cation with a quaternary ammonium. Exchanging surface cations greatly lowers the surface energy of the clay, which enhances its wetting character and, as a result, raises the interlayer spacing (higher degrees of swelling). Montmorillonite's ability to show such character is dependent on particle size, amount and site of isomorphic substitution as well as the nature of the saturated cation.

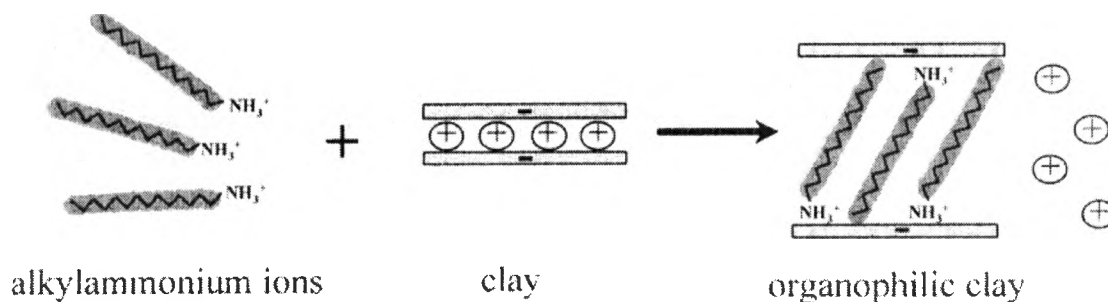


Figure 4. Cation Exchange of Alkylammonium Ions for Sodium Cations.²⁰

1.2.3 Formation of Polymer Clay Systems

Once the clay has been treated, it becomes possible to produce polymer nanocomposites from polymers of varying polarities. There are a variety of ways to produce polymer-clay nanocomposites. An example is seen in Figure 5. The most common techniques are in-situ polymerization, melt compounding, and solvent aided. The extrusion, or melt compounding, method is most suitable to our needs and, therefore,

is used throughout this study. The extrusion method facilitates the mixing process of the polymer and clay. In some situations, it has been observed that nearly perfect dispersion of nanoparticles with polymer can be achieved through twin screw extrusion.²¹ This can be explained by the shear force produced by the screws and the processing temperatures exerted on the mixture. Both variables allow the clay particles to slip past one another to create a dispersed system.

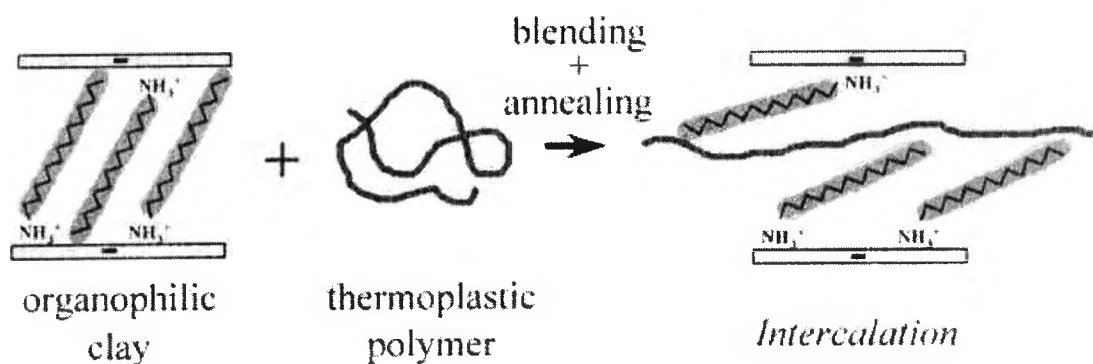


Figure 5. Melt Compounding Intercalation Process.²²

There are two main types of polymer nanocomposite systems formed; intercalated and exfoliated (Figure 6). In the former, the polymer chains alternate with the inorganic layer in an ordered and well defined manor. Intercalated systems exhibit distinct x-ray diffraction peaks. Exfoliated PLS nanocomposites are highly disordered and are considered to be completely dispersed within the matrix. This exfoliation causes the heterogenous mixture to act in such a manner that it operates much like a homogeneous entity.

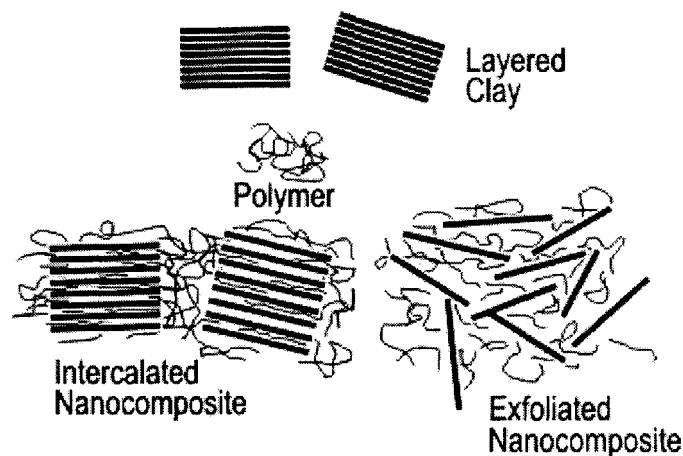


Figure 6. Intercalated and Exfoliated Polymer Layered Silicate Nanocomposite. ²³

The advantage of using nano-size particles over conventional fillers, like carbon fiber, is the ability of the end product to exhibit the improvements formerly discussed at much lower filler loading rates, 1-5 % versus 30 % for a conventional composite.

1.3 Tortuous Pathway

In 1967 Nielsen developed a simple theory pertaining to barrier properties of polymer-clay nanocomposites.²⁴ Nielsen's theory focuses on a tortuous path (Barrier Model) around the clay plates, in which a gas permeant must travel a longer distance to penetrate through a system. The clay plates create a maze which slows down the permeant as it travels through the matrix. The increase in path length is a consequence of the high aspect ratio of the clay filler. This theory only takes into account the aspect ratio of the clay plates and the volume percent of the filler in the composite. Nielsen's equation for permeability as a function of aspect ratio,

$$\frac{P_f}{P_u} = \frac{V_p}{1 + (L/2W)V_f}$$

Equation 1. Nielsen's equation for permeability, 2-Dimensional.

where P_f is the permeability coefficient of the composite, and P_u is the permeability coefficient of the pristine polymer, V_p is the volume fraction of the polymer and V_f is the volume fraction of the filler, L is the average length and W is the average thickness of the filler.

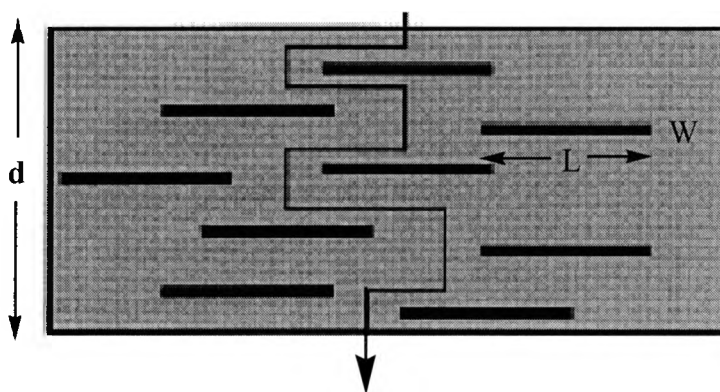


Figure 7. Tortuous Pathway in PLS Nanocomposite.²⁵

At very low clay loading rates, Nielsen's model predicts the permeability behavior of a system quite well, especially at clay loading rates of less than one percent. The experimental data deviates greatly from predicted values from the tortuous path model at higher clay loading rates and in certain polymers. In Nylon 6 nanocomposites, the gas permeability decreases by a factor of two, the tortuous path model predicts a factor of about three, while Nylon-MXD6 (an aromatic nylon) nanocomposites decrease by a factor of forty. This phenomenon cannot be explained by the simple tortuous path model.

The simple tortuous path model cannot explain many of the experimental observations published in the literature. One such observation involves the relative permeability from various permeants on the same polymer nanocomposite. Experiments conducted on polyimide nanocomposite with water, O₂, and CO₂, reveal aspect ratios of 132, 87, 83, respectively. The measured aspect ratio of montmorillonite is about 200.²⁶

This model cannot explain the effects of humidity on relative permeability. Work conducted on polyimide nanocomposites revealed that the relative permeability of these composites decreased with increasing relative humidity, for a pure polyimide polymer the relative permeability increased with increasing relative humidity.²⁷ The tortuous path model could not explain these data.

A major disadvantage of this model is that it cannot correlate between aspect ratio and relative permeability even though it predicts the relative permeability to be a function of the aspect ratio. This model assumes that the clay plates are perfectly oriented and spaced evenly with the plane of the polymer film. Predictably, perfect orientation and even spacing does not occur.

1.4 Conceptual Model

A new model has been recently proposed by Beall.⁸ The “conceptual model” focuses on the polymer-clay interface as the governing factor in addition to the tortuous path. It defines three regions around the clay plates: the surface modifier region, the constrained polymer region, and the unconstrained polymer region. The surface modifier region binds the clay with the polymer and owes its size (1-2 nm) to the surface modifier type. This area can be measured by x-ray diffraction. The unconstrained polymer region

is not affected much by the clay and will experience properties to a large extent like a pristine polymer. The constrained polymer region is less well defined, but has been indirectly confirmed. This region is in direct contact with the surface modifier and may extend 50-100 nm, depending on polymer's intermolecular force from the surface of the clay. This model also assumes the existence of four individual phases: a clay phase, a surface modifier phase, a constrained phase, and a polymer phase.

By modifying the tortuous path model to account for various regions around the clay plates and assuming the existence of four distinct phases, it is believed that a model can be developed that can accurately predict the diffusion of gases through PLS nanocomposites.

The tortuous path model for PLS nanocomposites contains clay platelets in a polymer film which make the path of the gases greater than the geometric path. The model we are proposing focuses on the region around the clay plates. This constrained polymer region will yield different results when compared to the tortuous path model. The path in which the gases are diffused is much greater than that of the tortuous path model. This is because the constrained polymer region has a lower permeability than the polymer that is not affected by the clay platelet since it has less disorder and lower free volume.

Computations performed by Beall, calculated with the tortuous path model, show great deviation in predicted diffusion rates compared to experimentally accepted values. Calculated diffusion rates on the same systems with the modified conceptual model were in better agreement with experimental values. This analysis however had to assume two parameters which include the size of the constrained polymer region and the relative

permeabilities of the constrained region. The aim of this research is to attempt to measure one of these parameters, the size of the constrained polymer region.

1.5 Analysis

Nylon 6 and Nylon-MXD6 are processed into well oriented-exfoliated polymer nanocomposites. The pristine polymers along with their nanocomposites are extruded into thin film for analysis. X-ray diffraction data, CuK α radiation, is used to measure the extent of exfoliation in all system and to obtain the crystal structure of the Nylon 6 nanocomposites. All films were microtomed normal to the film direction and analyzed with an Atomic Force Microscope (AFM) operating in contact mode in order to determine the position of the clay plates and topographical relief in the samples around the clay plates. Microtomed samples were placed in a 98% relative humidity chamber in order to swell the polymer. The unconstrained polymer regions will swell more than the constrained regions. AFM measurement may confirm this phenomenon.

Our intended research is focused on measuring the size and shape of the constrained polymer region. Future research will correlate the data with commonly applied polymer interaction parameters to determine if general predictions can be made on the size of the constrained polymer region. Relative diffusion coefficients will then be derived from the measured size of the constrained and unconstrained polymer regions. Based on these calculations, a comparison will be made between the calculated relative permeability and experimentally measured permeability. It is our belief that a universally accepted model can be developed to accurately predict the diffusion of gases through PCNs.

CHAPTER 2

EXPERIMENTAL

2.1 Materials

The list of all materials used throughout the course of this study is outlined in Table 1.

Table 1. Experimental Materials.

Name	Supplier	Amount	Grade or Lot #
Montmorillonite (Cloisite Na ⁺)	Southern Clay Products	–	92.6 meq/100g clay
Nylon-MXD6	Mitsubishi Gas Chemical	25 kg	6007
Polyamide 6 (Nylon 6)	DuPont	25 kg	Zytel 211
Stearylamine (Octadecylamine)	Sigma-Aldrich	1.5 kg	112K3711
Hydrochloric Acid	EMD	2.5 L	43282
Sodium Chloride	Mallinckrodt	2.5 kg	7581V17613
Calcium Chloride	EM Science	500 g	43008307
Cupric Sulfate	Spectrum	500 g	6D289
Drierite	Acrös	2 kg	A01749130
Vinylcyclophene Dioxide (VCD)	SPI Supplies	250 ml	1091220
Diglycidyl Ether of Polypropylene Glycol (DER 736)	SPI Supplies	250 g	1090915
Nonenyl Succinic Anhydride (NSA)	SPI Supplies	450 g	1090707
Dimethylaminoethanol	SPI Supplies	25 g	1100601

2.2 Organoclay Formation

The organoclay was prepared via the “dry process method”. Cloisite Na⁺ was modified by protonating octadecylamine with hydrochloric acid and water. The guideline used was to combine a mixture at 95 meq/100 g of cloisite Na⁺, with the addition of 110% octadecylamine and 110% acid to produce an optimum exchange of the sodium cations on the surface of the clay with the newly formed quaternary ammonium salt. Octadecylamine was first brought to a melt and introduced to 250 g of cloisite Na⁺ clay, a blend of hot distilled water and hydrochloric acid was added and mixed with a household stand mixer.

The mixture was processed through a Hobert commercial single screw Auger extruder model 4522. After the extrusion process, the organoclay was placed in a 70°C oven overnight until dry. Once the clay had dried, it was ground and washed to remove any residual salt. The organoclay was then returned to a 70°C oven.

The dried organoclay was ground and sieved with the help of a Humboldt Intermatic vibratory sieve shaker. A 325 mesh (45 micron grating) sieve was used to produce the desired organoclay particle size. The sieved organoclay was placed in a 70°C oven, under vacuum, until further use.

2.3 Extrusion of Nylon 6 PLS Nanocomposite

Nylon 6 was processed into PLS nanocomposites by melt compounding using a HBI System 90 computer drive attached to a Haake Rheomix CTW100 twin screw

extruder. Prior to each processing step, all materials were dried in a vacuum oven set at 70°C until further use to prevent moisture build-up.

2.3.1 Nylon 6 PLS Nanocomposite Monofilament Formation

Nylon 6 PLS nanocomposites were prepared at clay loading of 0.5 %, 2.0 %, and 5.0 % by weight of clay. This was accomplished by mixing the appropriate amounts of polymer and clay in sealed plastic bags, Ziploc style, to create the desired clay loading. The content of the bag was shaken to create a uniform mixture. The mixture was then transferred into glass beakers and dried.

The set processing parameters for all PLS nanocomposite formations are listed in Table 2. The Nylon 6 PLS nanocomposites were extruded into monofilaments using a 3 mm die head. Once the composites passed the die head, they were quenched in a water bath. The monofilaments were pelletized through a Haake PPI Pelletizer Postex and stored dried, waiting further use.

Table 2. Temperature and RPM Parameters for Extruding Nylon 6 Nanocomposites into Monofilaments.

Clay loading	Processing Temperature (°C)			RPM
	Rear	Middle	Front	
0.5 %	230	240	245	85
2.0%	230	245	245	85
5.0%	235	245	245	85

2.3.2 Nylon 6 PLS Nanocomposite Film Formation

Dried pellets from the previously made nanocomposites were introduced into the Haake Rheomix CTW100 twin screw extruder. A 15.24 cm thin film die head with a 2 mm slit opening was attached to the extruder. The processing parameters used for making the films are tabulated in Table 3. The RPM's for each were varied at different time intervals during the extrusion process (85-100 RPM). The films were immediately quenched in a water bath and placed to dry in the vacuum oven.

Table 3. Temperature and RPM Parameters for Extruding Nylon 6 Nanocomposites into Thin Films.

Nylon 6 Nanocomposite (Clay loading)	Processing Temperature (°C)				RPM (Varied at times)
	Rear	Middle	Front	Die Head	
0.5 %	260	245	245	235	85-100
2.0%	260	250	245	235	85-100
5.0%	260	250	250	240	85-100

The films were further processed into thinner films (≤ 1 mm) using a Carver Model C Platen Press set at 235°C. A constant force of 5000 lbs/in² was applied to each film for 5 minutes. Once the films were removed from the press they were cooled in a water bath, and dried.

2.4 Extrusion of Nylon-MXD6 PLS Nanocomposite

The same instruments and processing techniques used to produce Nylon 6 nanocomposites into monofilaments and thin films were used in the fabrication of Nylon-MXD6 nanocomposite.

2.4.1 Nylon-MXD6 PLS Nanocomposite Monofilament Formation

Nylon-MXD6 nanocomposites were manufactured at clay loading of 0.5 %, 2.0 %, and 5.0 % by weight. The set processing parameters for extruding Nylon-MXD6 into monofilament nanocomposites are listed in Table 4.

Table 4. Temperature and RPM Parameters for Extruding Nylon-MXD6 Nanocomposites into Monofilaments.

Clay loading	Processing Temperature (°C)			RPM
	Rear	Middle	Front	
0.5 %	245	245	250	85
2.0%	245	250	250	85
5.0%	245	250	250	85

2.4.2 Nylon-MXD6 PLS Nanocomposite Film Formation

The processing parameters for making thin films (~ 5mm) are tabulated in Table 5. Thinner films (less than 1 mm) of these nanocomposites were made using the Carver heated press in the same manner previously discussed in section 2.3.2 for the Nylon 6 nanocomposites, but at a press set temperature of 250°C.

Table 5. Temperature and RPM Parameters for Extruding Nylon-MXD6 Nanocomposites into Thin Films.

Nylon-MXD6 Nanocomposite (Clay loading)	Processing Temperature (°C)				RPM (Varied at times)
	Rear	Middle	Front	Die Head	
0.5 %	265	255	255	255	85-100
2.0%	265	265	255	255	85-100
5.0%	265	265	255	255	85-100

2.5 Characterization Techniques

2.5.1 Thermogravimetric Analysis

Thermogravimetric analysis (TGA) was performed for all nanocomposite films of Nylon 6 and Nylon-MXD6 on a TGA Q50. These analyses were conducted on a platinum pan, under air, at a scan rate of 20°C/minute from room temperature to 800°C. All samples were dried before analysis.

2.5.2 X-ray Diffraction

All nanocomposite films were scanned with a Bruker AXS D8 Focus X-ray Diffraction Instrument. CuK α radiation was utilized to carry out the study. Nylon-MXD6 and Nylon-MXD6 nanocomposites were scanned from 1° to 22° 2-Theta. Nylon 6 and its nanocomposites were scanned from 1° to 28° 2-Theta.

2.5.3 Atomic Force Microscopy

All samples were embedded using the method described by Spurr.^{28,29} The standard formula to cure all samples was utilized, as in Table 6. Before the embedding process, all nanocomposites were cut into smaller pieces and dried to achieve proper curing. The nanocomposites were placed into size 00 BEEM capsule along with the embedding resin. The capsules were then placed in a 70°C oven for curing.

Table 6. Standard and Modified Embedding Formulations.²⁰

COMPONENT	WEIGHT OF SPURR COMPONENTS (grams)		
	STANDARD FORMULA FIRM	HARD	SOFT
VCD	10.0	10.0	10.0
DER 736	6.0	4.0	7.0
NSA	26.0	26.0	26.0
DMAE	0.4	0.4	0.4

The embedded nanocomposites were microtomed using a Boeckeler RMC Product PowerTome XL with a RMC MTXL computer attachment. A diamond knife was used to obtain 100 nm thick nanocomposite slices. The sliced samples were placed on silicon oxide wafers, which were previously cut into 2.00 cm² plates, and dried under vacuum in a glass dessicator filled with Drierite. Once dried, the samples were sandwiched between silicon oxide plates and placed in an 85°C oven under vacuum. They were then transferred into a 98 % R.H. chamber and later scanned with the Atomic Force Microscope. The samples were scanned at hourly intervals.

Atomic Force Microscopy (AFM) was done with a Veeco Dimension 3100 Atomic Force Microscope attached to a Nanoscope Dimension 3100 Controller. Contact-mode AFM was used for all analysis.

CHAPTER 3

RESULTS AND DISCUSSION

3.1 Monofilaments and Films Visual Appearance

The monofilament PCNs of Nylon 6 and Nylon-MXD6 showed signs of yellowing with increased clay loadings when compared to the pristine polymers. In both the Nylon 6 and Nylon-MXD6 systems, the 0.5 % clay loaded nanocomposites showed the least coloration. The 2 % clay loaded nanocomposites showed a darker hint of yellowing while the 5 % clay loaded nanocomposites exhibited the greatest color distortion.

All extruded films (> 2 mm) showed the same yellowing characteristics as the monofilaments. When the films were pressed (< 1 mm) into thinner sections, it became harder to distinguish between the pristine polymer, the 0.5 % PCN, and the 2 % PCN. The 5 % clay loaded systems differed slightly in coloration, but was still difficult to distinguish from the others.

3.2 Thermogravimetric Analysis

Thermogravimetric analysis was used to determine the actual clay loadings of the newly made nanocomposites. The remaining residual mass after the TGA experiments

for each nanocomposite was compared to that of pristine polymers. The relative clay loadings were calculated based on the percent difference from their corresponding residual mass.

3.2.1 TGA of Nylon 6 and Nanocomposites

Nylon 6 acted as the benchmark for all other Nylon 6 nanocomposites. All samples were run in triplicate. At 800°C, TGA gave a mass residue of 0.01964 mg from a sample initially weighing 10.1920 mg. After the analysis, 0.1927 % of the original sample was left after the experimental run. The TGA graph of Nylon 6 is depicted in Figure 8. Table 7 contains TGA data for all Nylon PCNs along with the pristine polymer. Figure 9 illustrates an overlay for the TGA graphs of the Nylon 6 samples.

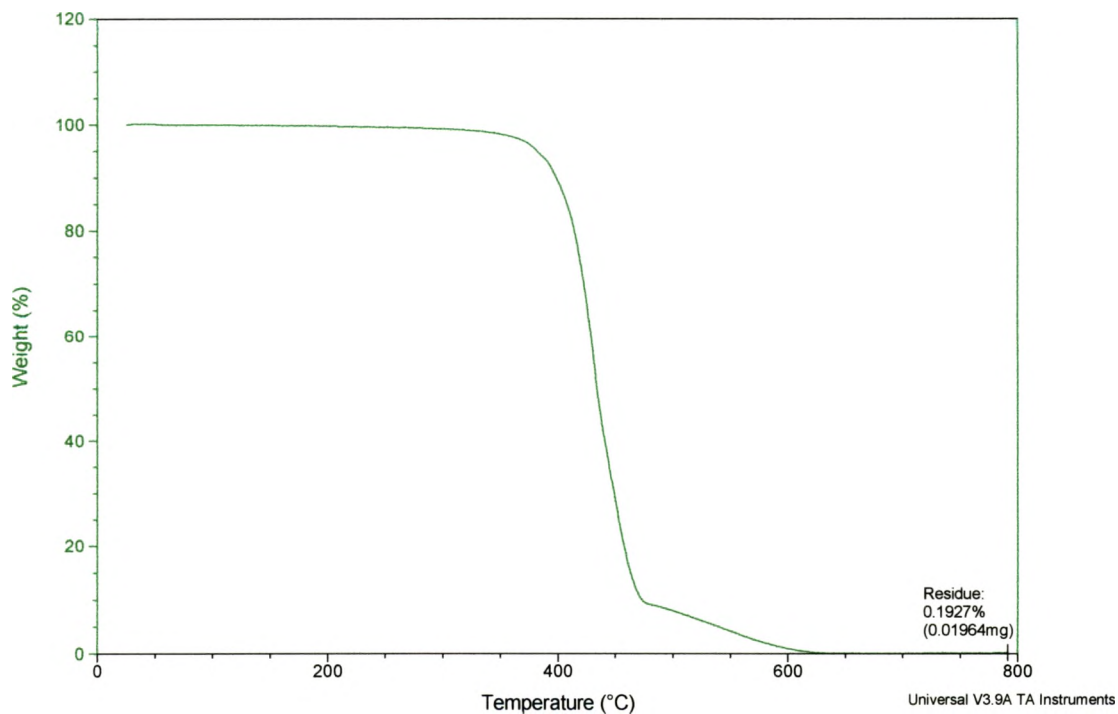
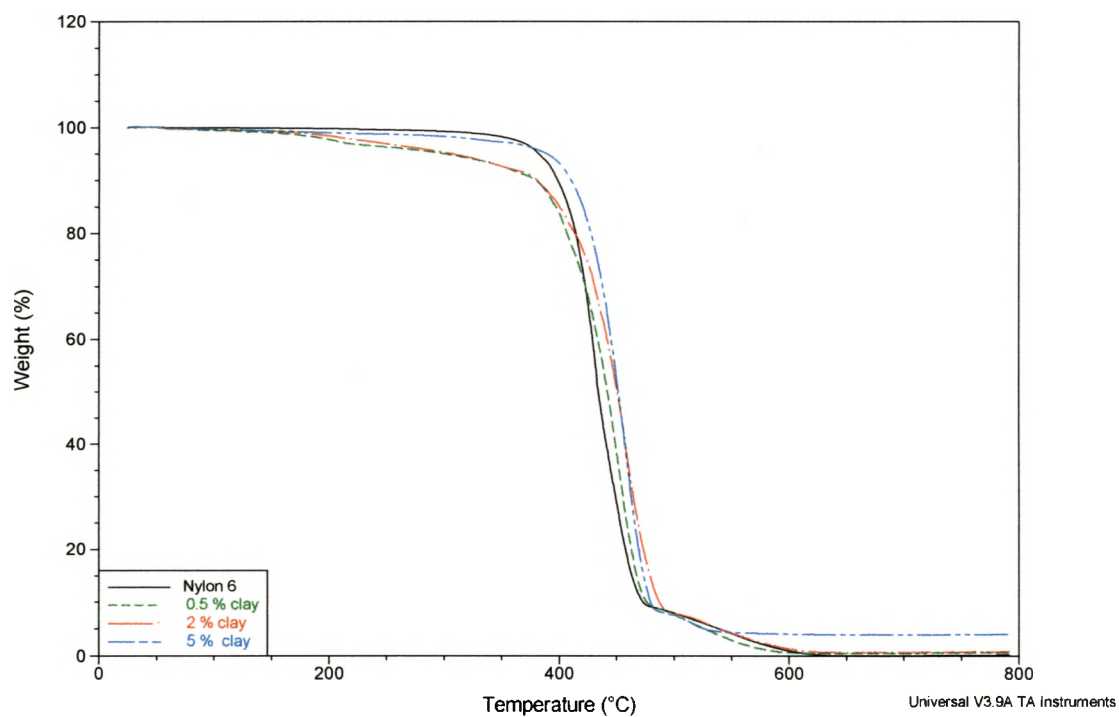


Figure 8. Thermogravimetric Analysis of Nylon 6. Data was collected at 800°C.

Table 7. TGA Results of Nylon 6 and PCNs. Data was recorded at 800°C.

Sample	Initial mass (mg)	Residue (mg)	Percent residue	Clay loading (%)
Nylon 6 Pristine polymer	10.1920	0.01964	0.193	—
Nylon 6 0.5 % clay loading	6.5790	0.04291	0.652	0.58
Nylon 6 2 % clay loading	9.9540	0.1681	1.689	1.87
Nylon 6 5 % clay loading	5.6588	0.2288	4.044	4.85

**Figure 9. TGA Overlay of Nylon 6 and PCNs.** Data was collected at 800°C.

3.2.2 TGA of Nylon-MXD6 and Nanocomposites

Nylon-MXD6 was the marker for all nanocomposites of this type. All samples were run in triplicate. TGA gave a mass residue of 0.02658 mg, at 800°C, from a sample initially weighing 24.5900 mg. From the original sample, 0.1081 % residue was left after the experimental run. The TGA graph for Nylon-MXD6 is seen in Figure 10 and the overlay of all MXD6 systems in Figure 11. Table 8 contains the experimental data, collected at 800°C, for all Nylon-MXD6 samples.

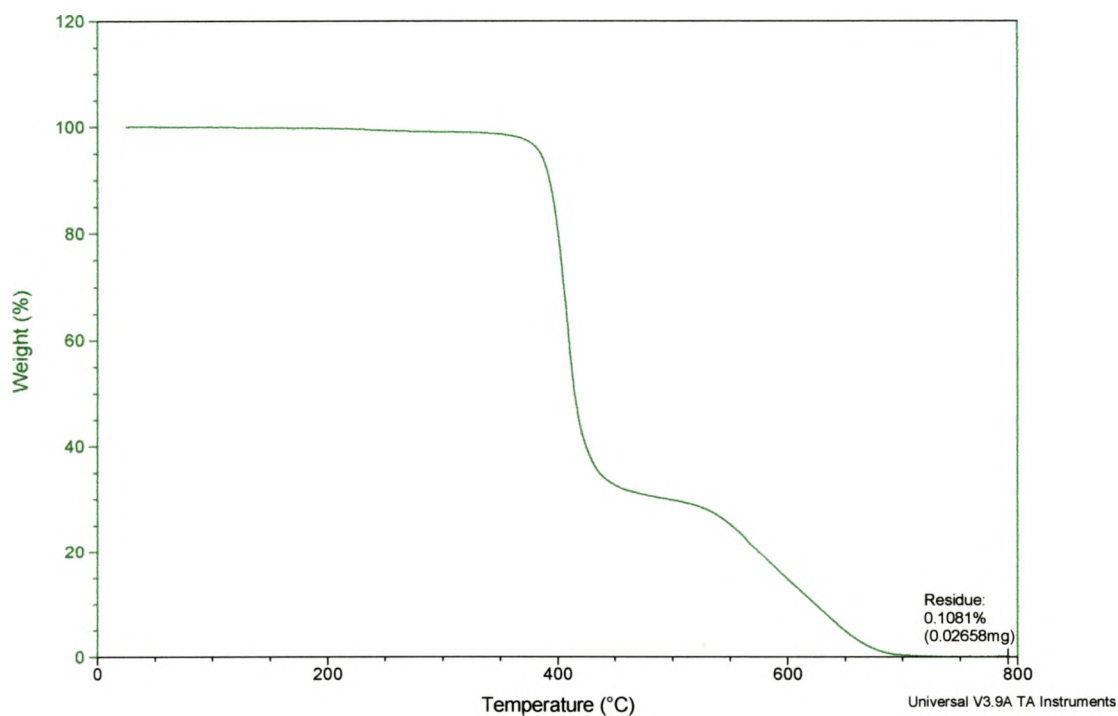
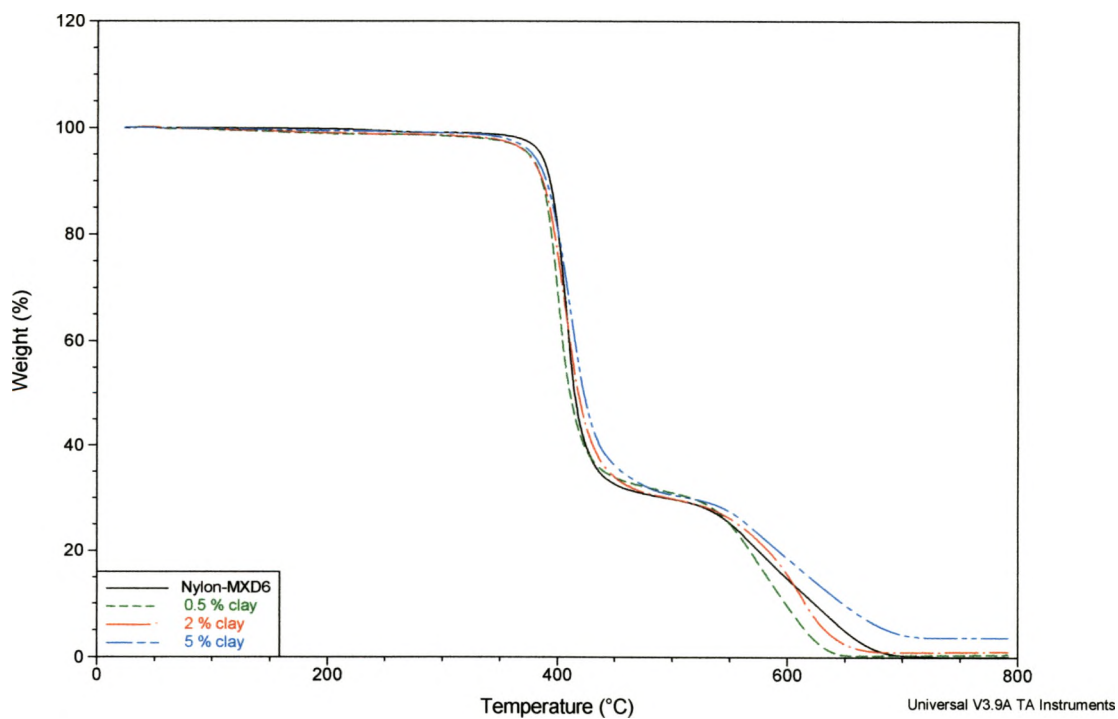


Figure 10. Thermogravimetric Analysis of Nylon-MXD6. Data was collected at 800°C.

Table 8. TGA Results of Nylon-MXD6 and PCNs. Data was recorded at 800°C.

Sample	Initial mass (mg)	Residue (mg)	Percent residue	Clay loading (%)
Nylon-MXD6 Pristine polymer	24.5900	0.0265	0.108	—
Nylon-MXD6 0.5 % clay loading	5.0980	0.0276	0.542	0.54
Nylon-MXD6 2 % clay loading	6.0007	0.0869	1.448	1.68
Nylon-MXD6 5 % clay loading	14.3070	0.5303	3.707	4.53

**Figure 11. TGA Overlay of Nylon-MXD6 and PCNs.** Data was collected at 800°C.

3.2.3 Experimental Clay Loading

It is easy to speculate possible reasons for underloading the samples. The polymer-organoclay mixtures were not introduced into the extruder in proper amounts. In all cases, small amounts of organoclay were left attached to the Ziploc bag. When the systems were extruded, a considerable amount of the organoclay did not pass through the melt process, but was found inside the rear chamber of the extruder.

3.3 X-ray Diffraction

The goal in producing thin films was to create oriented-exfoliated systems since it is well established that the platy morphology of the clay orients strongly along flow lines. X-ray diffraction data was also used to establish whether or not the clay platelets in the PCNs were exfoliated into the polymer matrix.

X-ray diffraction data of monofilament pressed films originally indicated that some level of intercalation (small diffraction peaks at low 2-Theta) was present in some, but not all polymer clay nanocomposites. This was especially true for the Nylon-MXD6 PCNs, which when melt compounded produced uneven exfoliation, see Figure 12. After the thin film extrusion process, the absence of peaks at low 2-Theta angles indicated the absence of an intercalated system and the presence of an exfoliated system. The orientation of the clay in the thin films makes the x-ray much more sensitive to intercalates.

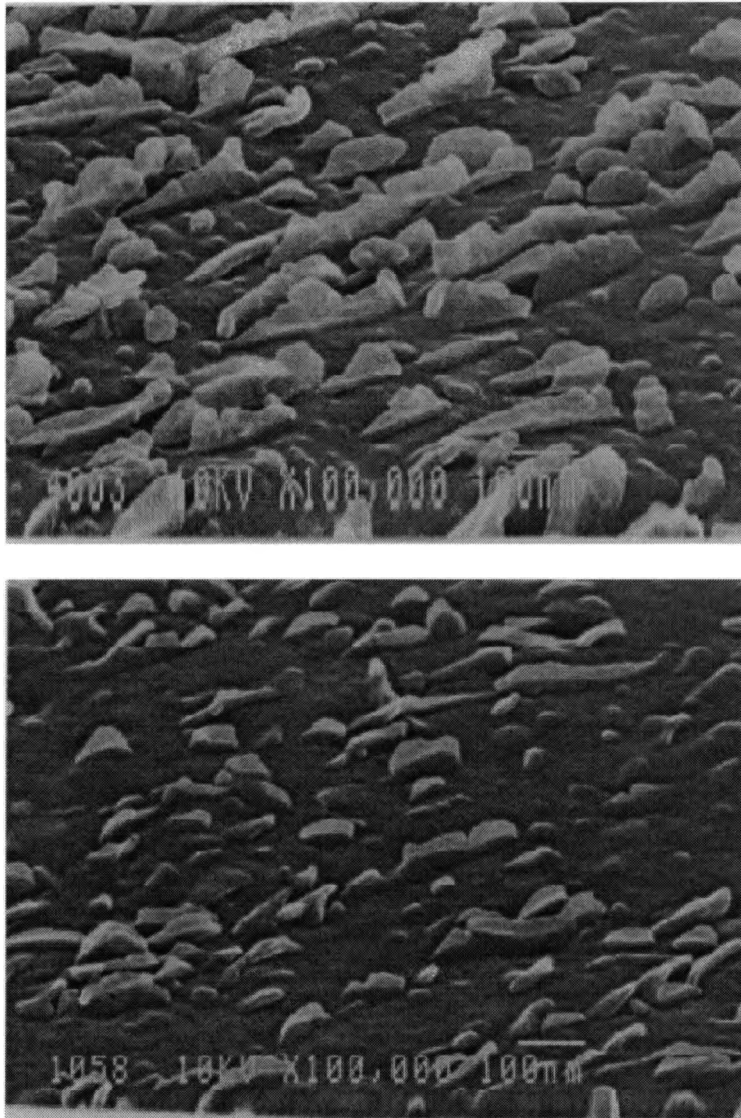


Figure 12. SEM Image of Etched Nylon 6 (top) and Nylon-MXD6 (bottom) at 5 % Clay Loading. Evidence of uneven exfoliation is seen for Nylon-MXD6.

3.3.1 X-ray Diffraction of Nylon 6 and Nanocomposites

In recent years, it has been observed that clay nanoparticles, like montmorillonite, affect the crystallization behavior of Nylon 6. It has been reported, for Nylon 6 PLS, that the addition of a silicate favors the transformation from the α -crystalline form to the γ -

crystalline form.^{30,31,32,33} The addition of clay favors the γ -crystalline form with increasing clay loading regardless of preparation type.

Figure 13 contains the x-ray diffraction data for Nylon 6 and Nylon 6 nanocomposites, individual x-ray diffraction data can be seen in the Appendix. The data acquired is in agreement with the experimental data obtained by Liu.³⁴ Nylon 6 exhibits two stable crystal structures, the α and γ monoclinic forms. The peaks observed at 20.275° and 23.422° 2-Theta for pristine Nylon 6 are characteristic of α -crystalline form, represented as α -1 and α -2 by Wu.³⁵

These characteristic α -crystalline form peaks are observed for the 0.5 % clay loaded nanocomposite at 20.285° and 23.961° 2-Theta. The intensity of these peaks has changed with the addition of the nanoclay. For the 0.5 % clay loaded nanocomposite, the α -2 diffraction peak was more intense than the α -1 diffraction peak when compared to Nylon 6.

The 2 % clay loaded Nylon 6 nanocomposite exhibited a different crystal structure conformation altogether. The γ and not the α -crystal structure was now the dominate form. The weak diffraction peak at 10.999° and the strong diffraction peak at 21.545° 2-Theta are characteristic of the γ -crystal structure.

The higher clay loaded nanocomposite (5 %) expressed the same characteristic crystalline behavior as the previously discussed PCN. The γ -crystalline diffraction peaks are observed at 11.062° and 21.712° 2-Theta.

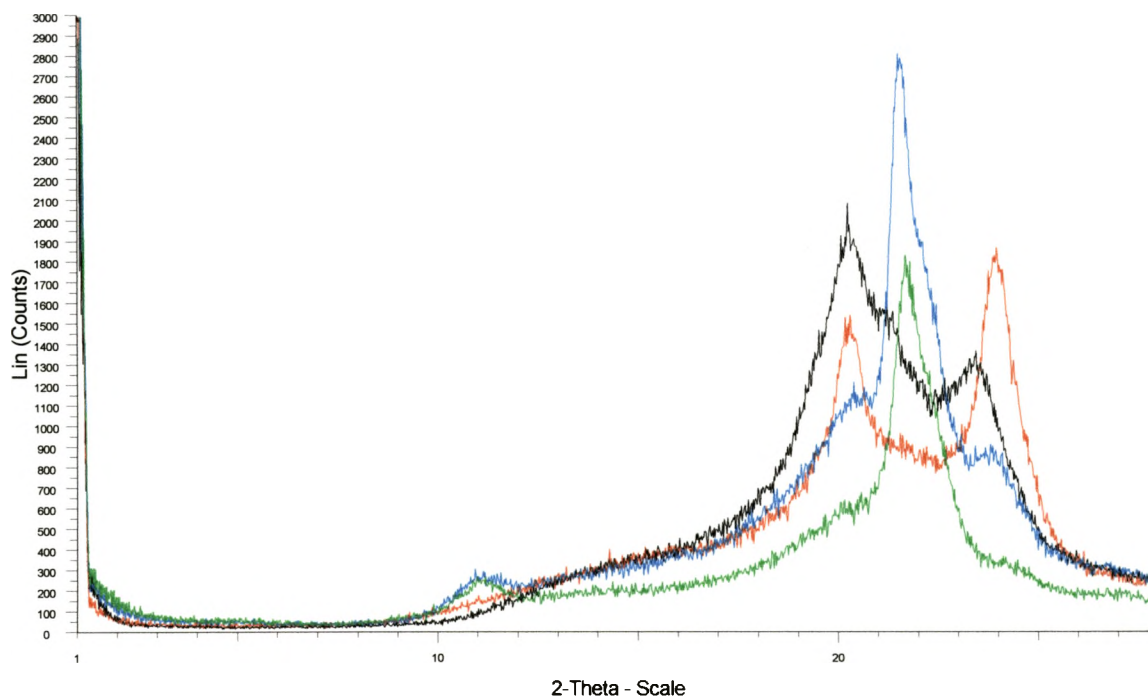


Figure 13. X-ray Diffraction Data of Nylon 6 and Nanocomposites.

Nylon 6 is well known for forming the maximum number of hydrogen bonds between polymer chains. These H-bonds dictate the crystal structure present in a polyamide system. Two crystalline structures form in Nylon 6, α and γ . These two structures have been well documented in the literature via X-ray diffraction.^{36,37,38,39,40}

For Nylon 6, the plane of the $(\text{CH}_2)_5$ group and the amide group in the α -crystalline form are parallel to each other, while in the γ -crystalline they offer a more perpendicular arrangement.⁴¹ There are two chain conformations demonstrated by Nylon 6, the full-extended chain and the twisted chain as illustrated in Figure 14. H-bonding in a parallel chain arrangement results in a γ -crystalline form, and an antiparallel chain arrangement is characteristic of an α -crystal structure. With the addition of clay, H-bonds form between parallel chains creating a more favorable γ -crystalline form. The

relationship with the silicate and the polymer governs this behavior, while the organic modifier plays an insignificant role in this event.

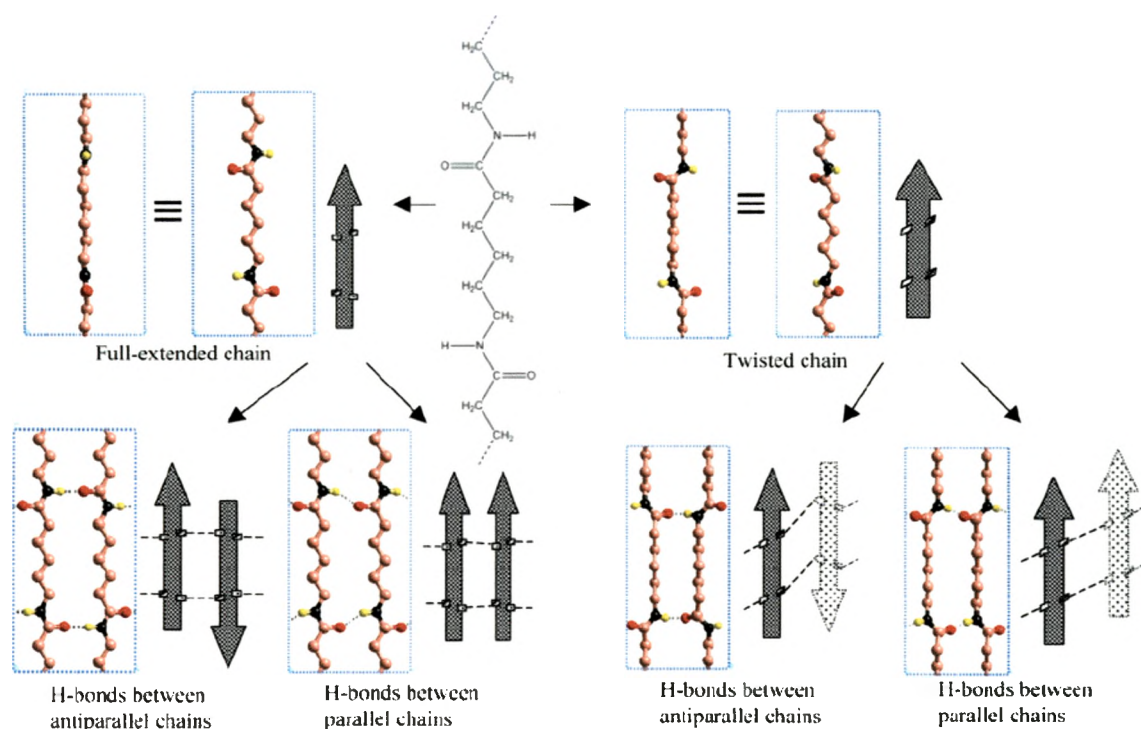


Figure 14. Conformational Crystal Structures of Nylon 6.⁴⁰ In all there are 8 classes and 14 stacking schemes for a total of 112 regular infinite chain crystal structures.

3.3.2 X-ray Diffraction of Nylon-MXD6 and Nanocomposites

The absence of low 2-Theta peaks in the x-ray diffraction data of the Nylon-MXD6 nanocomposites indicated a fully exfoliated system, as noted in section 3.2.1. Compared to the Nylon 6 systems, sharp and intense peaks were not seen at higher 2-Theta values. Instead, one broad peak was seen throughout the study. The broad peaks at higher 2-Theta values are characteristic of an amorphous type system. Figure 15 contains the x-ray diffraction data for all Nylon-MXD6 samples.

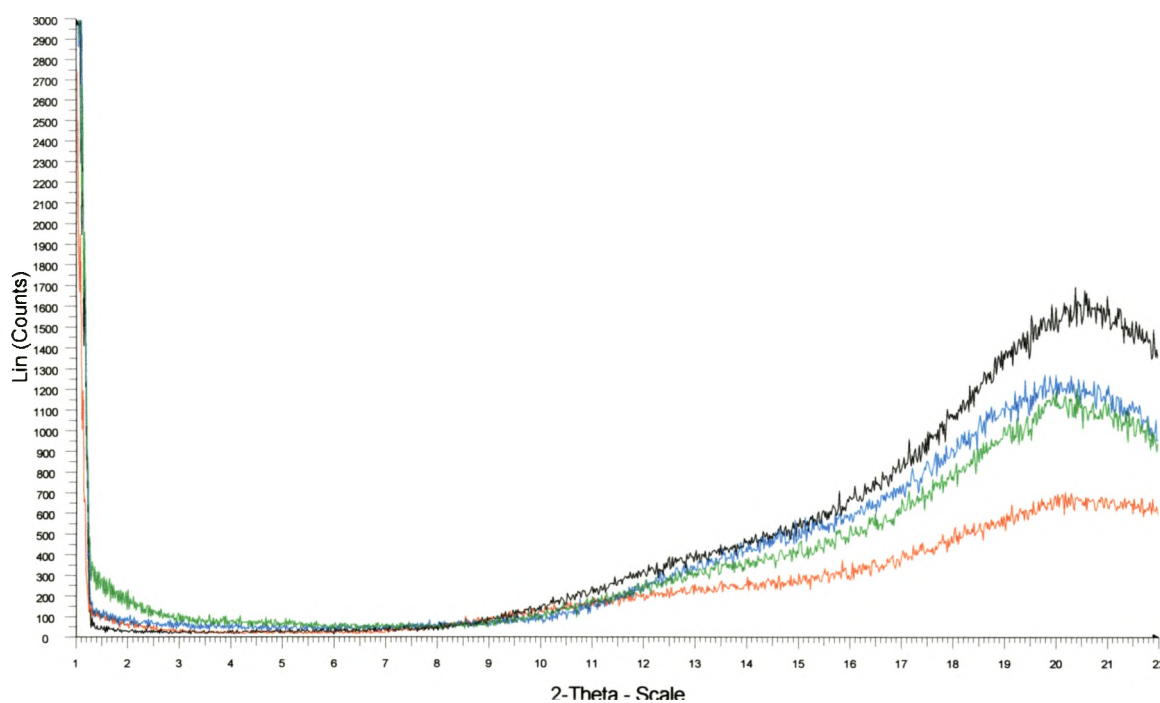


Figure 15. X-ray Diffraction Data of Nylon-MXD6 and Nanocomposites.

3.4 Atomic Force Microscopy

Through topographical analysis, AFM experiments located the constrained and unconstrained polymer regions in the PCN. Table 9 contains theoretical distances between clay plates in fully oriented-exfoliated PCNs.

Table 9. Theoretical Clay Distances in an Oriented-Exfoliated PCN.

weight % w/modifier	Weight % clay	Volume % clay	Distance between clay plates (nm)
0.5	0.4	0.154	648
2.0	1.6	0.615	162
5.0	4.0	1.54	64

Before any discussion in regards to measured topographical distances in AFM, it must be noted that it was desirable to measure the same area multiple times over a pre-established period, it was however difficult to do as a result of drift in both the y axis (slow axis) and x axis (fast axis) in the scans. In turn, it was easier to see the degree of swelling (shrinkage) over time in the systems in which the same area was captured. Throughout this paper, discussions began with the Nylon 6 samples, in the next section Nylon-MXD6 will be discussed first. All topographical measurement analysis (2-D, 3-D, and graphs) for all systems are located in the Appendix

3.4.1 AFM Analysis of Nylon-MXD6 PCNs

As discussed earlier, in section 1.2.1, the average dimensions of the clay are one nanometer in thickness in one dimension and from 150 ~ 250 nanometers in the other two. In the AFM experiments, it was assumed that the topographical valleys and hills correspond to the constrained and unconstrained polymer regions. In Nylon-MXD6 at 0.5% clay loading, pits were observed throughout each scan. Analysis of the pits revealed measured distances in the range of 200 nm. The distances correlated well with the dimensions of the clay, in view of the fact that the clay was oriented perpendicular to

the surface of the film, the dimensions were approximately what was expected for montmorillonite.

The average distance from clay plate to clay plate was acknowledged in Table 9 for each clay loaded PCN, section 3.3. In the area between the clay, due to the absence of clay in this region, the unconstrained polymer region dominates. The distance from clay plate to plate for a 0.5 % clay loaded system was calculated at 648 nm (refer to Table 9, section 3.4). AFM measurements approximately confirmed the calculated distance between the clay platelets. The distances measured between clay plates were about 600 nm which falls reasonably well with what was expected. These measurements can be seen in most topographical line graphs for this composite. All diagrams (located in the Appendix) contain 3-D and 2-D depictions of this system's surface at time zero through time 2 hours along with topographical measurement data. The green and blue lines, in the 2-D diagram, correspond to the examined topographical surface measurements of the sample. The green topographical line measurements in the 2-D models are depicted first throughout the Appendix.

Similarly to the previously discussed system, the dimension of the pits for Nylon-MXD6 at 2 % clay loading measured 200 nm. This strengthens the notion that the pits are in fact, clay plates. Nylon-MXD6 at 2 % clay loading contains more clay than at 0.5 % which is verified through AFM. As a result, more hills and valleys on the 3-D and 2-D models are visible on this PCN than on the one previously discussed. The calculated distance from clay plate to clay plate for this system is 162 nm. At time zero, measurements made were inconclusive regarding clay plate separation. Topographical hills and valleys were not as pronounced and therefore could not be interpreted, however

the distance became more apparent with time. At time 1 hour, the distance from clay plate to clay plate was in the range of 200 nm, this number is comparable with the calculated value of 162 nm. At time 2 hours similar observations were made. As expected, the unconstrained polymer region has diminished with increasing clay loading.

The 5 % clay loaded Nylon-MXD6 system displayed more but less pronounced features than at 2 %. Measurements of the unconstrained areas were relevant throughout each scan. More hills and valleys were present than in the other two systems which, again, was expected. As time progressed, these observations were accentuated. At time zero several indentations measured closely to the dimension of the clay, which provided convincing evidence of the presence of clay in these areas. Topographical measurements compared well with the calculated distance between clay plates for this system. The distance roughly measured 100 nm, compared to the calculated value of 64 nm. This was particularly observable after a lapse of time 2 hours.

3.4.2 AFM Analysis of Nylon 6 PCNs

AFM experiments conducted for the Nylon 6 at 0.5 % clay loading were at times difficult to interpret. The effects caused by water absorption did not help with the identification of the constrained and unconstrained polymer regions. The unconstrained polymer region was expected to swell, for a 100 nm thick slice, significantly. This was not the case for this type system. Topographical features illustrated the same frequency of hills and valleys observed in the Nylon-MXD6 nanocomposites at the same clay loading, but unfortunately, height measurements were on the order of 1–3 nm. As a result, it was harder to determine the areas in which the constrained and unconstrained

polymer regions were located. The system, over time, did not experience many topographical changes, which led to the idea that longer time intervals (water evaporation) were needed for all Nylon 6 type nanocomposites. The locations of the clay platelets were at times indistinguishable.

Nylon 6 at 2 % clay loading contained characteristic topographical style features seen in the Nylon-MXD6 PCNs. Swelling effects were considerable and more apparent than at 0.5 % clay loading. All Nylon 6 PCNs were expected to swell to a higher degree than those of the Nylon-MXD6 PCNs. This expected occurrence only happened at 2 % clay loading. Hills and valleys were highly recognizable in this type system and increased with time. Pits on the surface of the material measured closely to clay dimensions, signifying a presence in this area. This characteristic was not seen well at 0.5 % clay loading. Measurements of the clay plate separations were in the range of about 400 nm, the calculated size was 648 nm.

Nylon 6 at 5 % clay loading resembled the 0.5 % clay loaded system. The topographical height measurements were also in the range of 1-3 nm. As in the Nylon-MXD6 at 5 % clay loading, more hills and valleys were seen on the surface, and these increased with time. Detailed analysis of the constrained and unconstrained polymer regions were again difficult to interpret and therefore inconclusive.

3.4.3 Constrained Polymer Region

As discussed earlier in the introductory section of this paper, the expected range of the constrained polymer region predicted by Beall theoretically extends 50-100 nm from the surface of the clay. AFM analysis clearly demonstrated this to be true. Most of

the measured values for the constrained polymer region fell in agreement with the theoretically assumed values. Tables 10-13 contain measurement data of the constrained polymer region for all except two systems. Topographical measurements of Nylon 6 at 0.5 % and 5 % clay loading were difficult to analyze.

The simplest topographical measurements for the constrained polymer regions occurred in the areas in which pits were present, as valley to hill measurements were not as trivial. These measurements were made from the centers of the pits and valleys then extended to the midpoint of a hills maximum. Figures 16 and 17 represent typical style measurements for the constrained polymer region.

Analysis of the constrained polymer region depended greatly on the extent of the gradient in which a pit or valley met with its corresponding hill. At higher gradients, reference points established lower values for the constrained polymer region. Consequently, areas with broader gradients corresponded with higher values for the region.

Table 10. Constrained Polymer Region at Time 2 Hours for Nylon-MXD6 at 0.5% Clay Loading. The values are expressed in nm, standard deviation 20.559.

65	85	83	74	81	76	103
102	90	96	86	88	93	94
78	72	79	90	90	95	72
87	86	75	84	88	93	116
65	124	130	75	126	104	77
97	57	84	71	118	141	67
113	121	61	88	92	51	56
78	46	45	57	78	99	70
59	63	88	72	59	84	84

Table 11. Constrained Polymer Region at Time 2 Hours for Nylon-MXD6 at 2 % Clay Loading. The values are expressed in nm, standard deviation 20.375.

79	87	71	96	79	99	77
80	114	54	108	96	83	128
68	117	123	98	64	76	78
87	92	78	79	66	90	49
99	47	68	52	44	50	83
41	66	82	44	84	118	76
93	100	86	93	86	118	92
92	86	93	86	96	100	67
83	70	71	62	65	55	59

Table 12. Constrained Polymer Region at Time 2 Hours for Nylon-MXD6 at 5 % Clay Loading. The values are expressed in nm, standard deviation 19.492.

94	92	82	85	95	77	92
58	100	35	87	62	41	68
68	39	30	78	70	37	39
37	51	60	79	70	32	33
47	94	61	64	42	39	43
67	51	45	38	74	68	70
62	44	68	65	84	82	62
81	98	87	78	69	52	43
59	73	50	68	68	44	89

Table 13. Constrained Polymer Region at Time 2 Hours for Nylon 6 at 2 % Clay Loading. The values are expressed in nm, standard deviation 14.395.

74	81	78	93	62	99	75
89	91	92	85	97	62	59
77	76	81	103	77	74	78
84	75	75	58	97	63	87
86	69	67	104	71	90	73
79	88	93	57	63	72	78
86	93	56	56	87	89	72
84	88	78	86	88	87	101
126	86	120	75	95	96	97

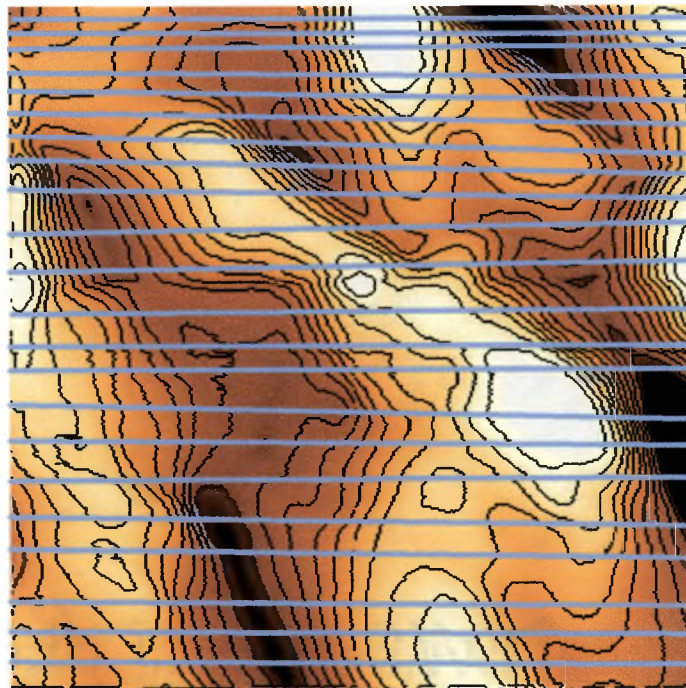


Figure 16. Typical Topographical Surface Measurements for all PCNs. A scanned surface area of $1\mu\text{m} \times 1\mu\text{m}$ is depicted.

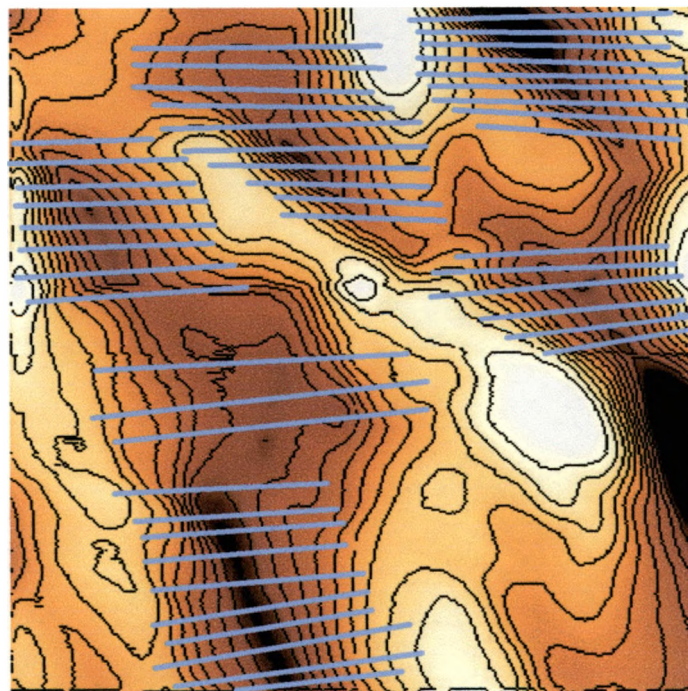


Figure 17. Typical Topographical Surface Measurements for the Constrained Polymer Region. A scanned surface area of $1\mu\text{m} \times 1\mu\text{m}$ is depicted.

CHAPTER 4

CONCLUSION

An attempt was made to measure the constrained polymer regions for several PCNs. It was theorized that the constrained polymer region extends 50 to 100 nm away from the surface of the clay. Analysis performed through AFM established that the range did in fact fall in agreement with the speculated values proposed by Beall.⁸

AFM topographical information of the PCNs proved to be of great importance. With an increase in clay loading, topographical hills and valleys became more frequent for a given area as seen in Figure 18. This occurred because of the decrease in the distance between clay plates. In higher clay loaded samples, the clay plates were closer to each other and as a result the frequency of hills and valleys were higher than on those of the lower clay loaded PCNs.

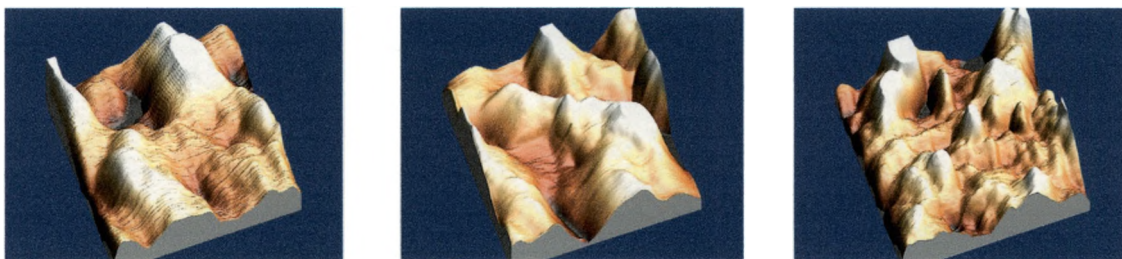


Figure 18. Increase of Topographical Features with an Increase in Clay Loading. Nylon-MXD6 at 0.5, 2.0, and 5.0 % clay loading are depicted respectively, a scanned surface area of $1\mu\text{m} \times 1\mu\text{m}$ is portrayed.

Experimentally measured distances between clay plates were in reasonable agreement with expected values. Trends were apparent when the distances between clay

plates were measured. In systems with lower clay loading, the distances between clay plates were higher. Lower distances between clay plates were seen in systems with higher clay contents.

Water evaporation played a role in determining and measuring the areas in which the constrained polymer regions relied. As water vapor escaped from the systems into the surroundings, the swelling character (shrinkage) and resolution of the hills and valley also became more apparent. It was determined that a higher time interval or increase temperature, for the evaporation of water to the surroundings was necessary.

The swelling behavior of the studied PCNs is also attributed to their crystalline makeup. The addition of clay turns the amorphous Nylon-MXD6 polymer into one with a pseudocrystalline character. This crystalline behavior is observed in areas which are in close proximity to the surface of the clay, the constrained polymer region. When comparing the unconstrained to the constrained polymer region of Nylon-MXD6, a decrease in free volume is observed in the area which acts crystalline. As a result the swelling effect caused by the solvent is amplified in the areas in which clay is absent, the unconstrained polymer region. These areas are clearly seen in the AFM analysis.

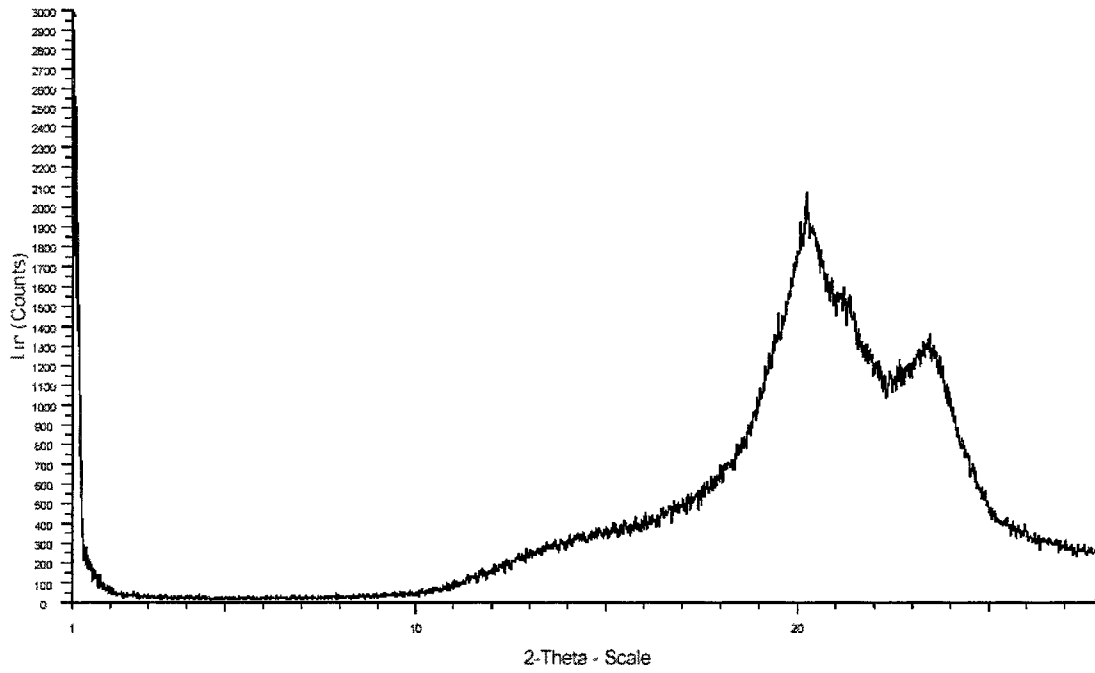
Nylon 6 acted in a different manner than Nylon-MXD6. The polymer is already in a crystalline state and so the swelling imparted by the solvent was more uniform in these samples. The topographical relief on the surface was significantly lower than those on Nylon-MXD6. The distinct amplitude of hills and valley of Nylon-MXD6 was a result of a transition from a crystalline domain to an amorphous one. In Nylon 6 the transition was between two crystalline forms and therefore the swelling amplitude for both areas acted quite similarly.

APPENDICES

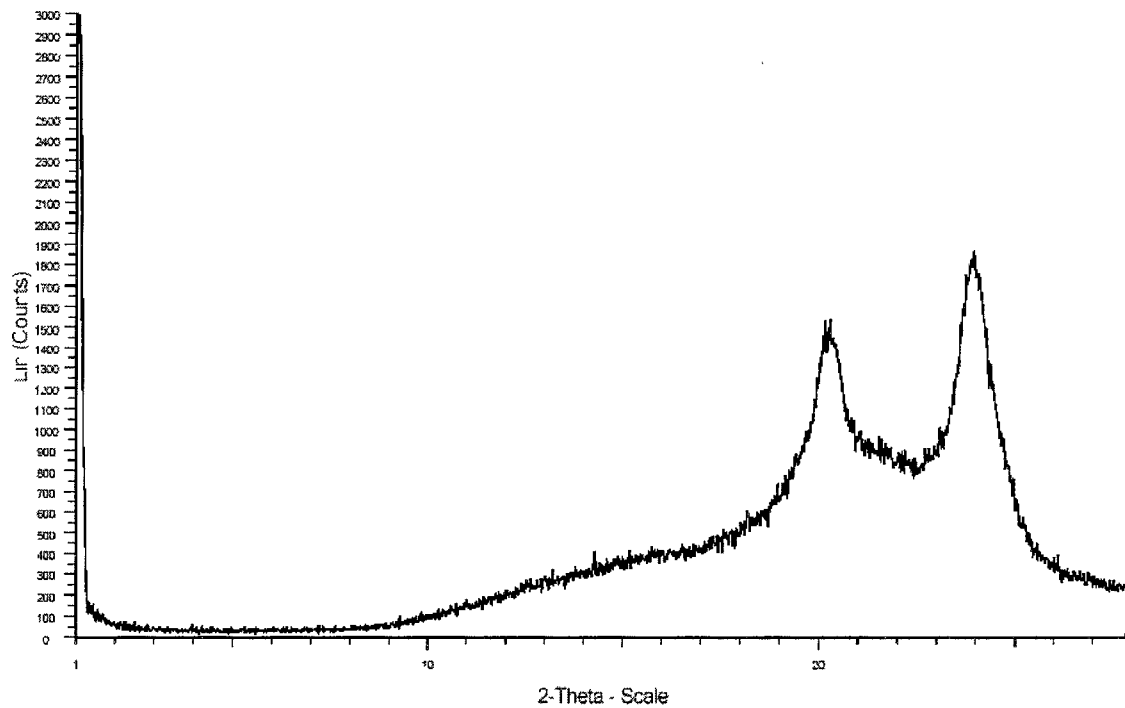
APPENDIX 1

X-ray Diffraction

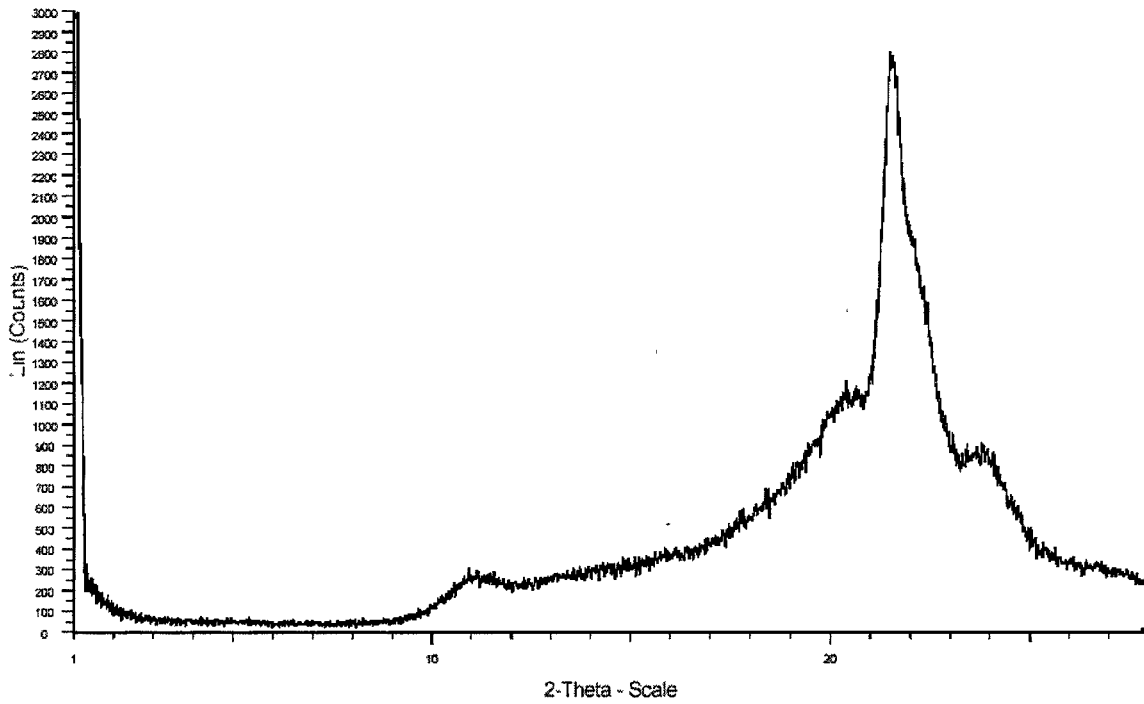
1. X-ray Diffraction of Nylon 6.
2. X-ray Diffraction of Nylon 6 at 0.5 % clay loading.
3. X-ray Diffraction of Nylon 6 at 2.0 % clay loading.
4. X-ray Diffraction of Nylon 6 at 5.0 % clay loading.
5. X-ray Diffraction of Nylon-MXD6.
6. X-ray Diffraction of Nylon-MXD6 at 0.5 % clay loading.
7. X-ray Diffraction of Nylon-MXD6 at 2.0 % clay loading.
8. X-ray Diffraction of Nylon-MXD6 at 5.0 % clay loading.



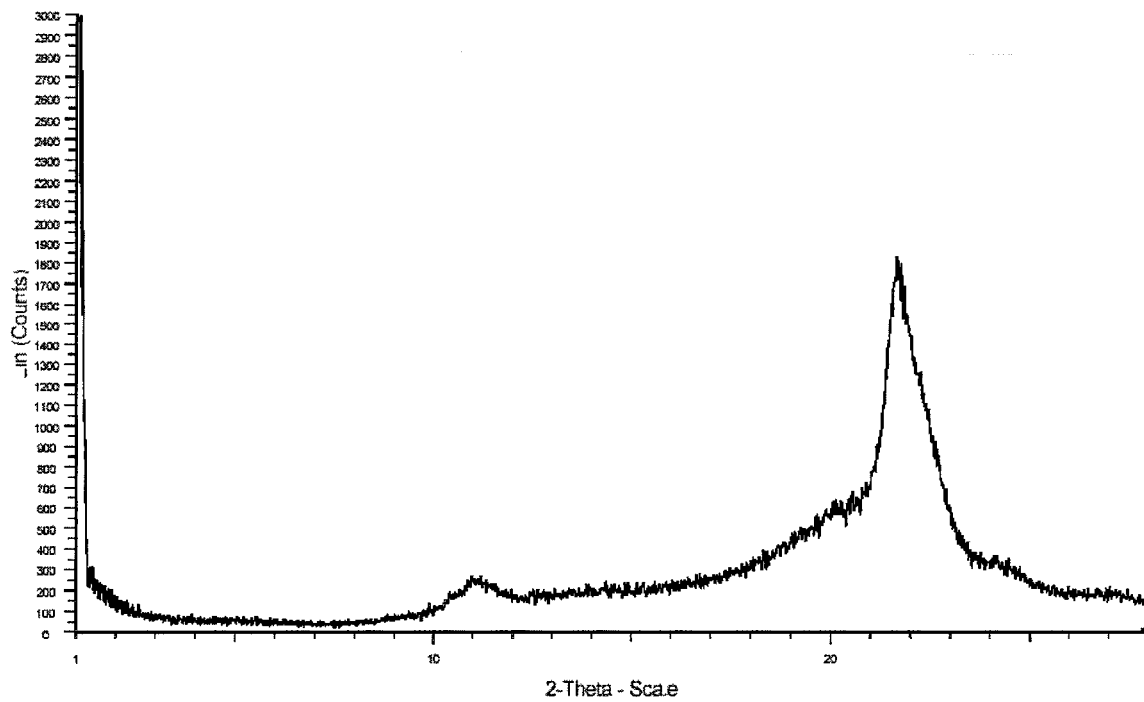
1. X-ray diffraction of Nylon 6.



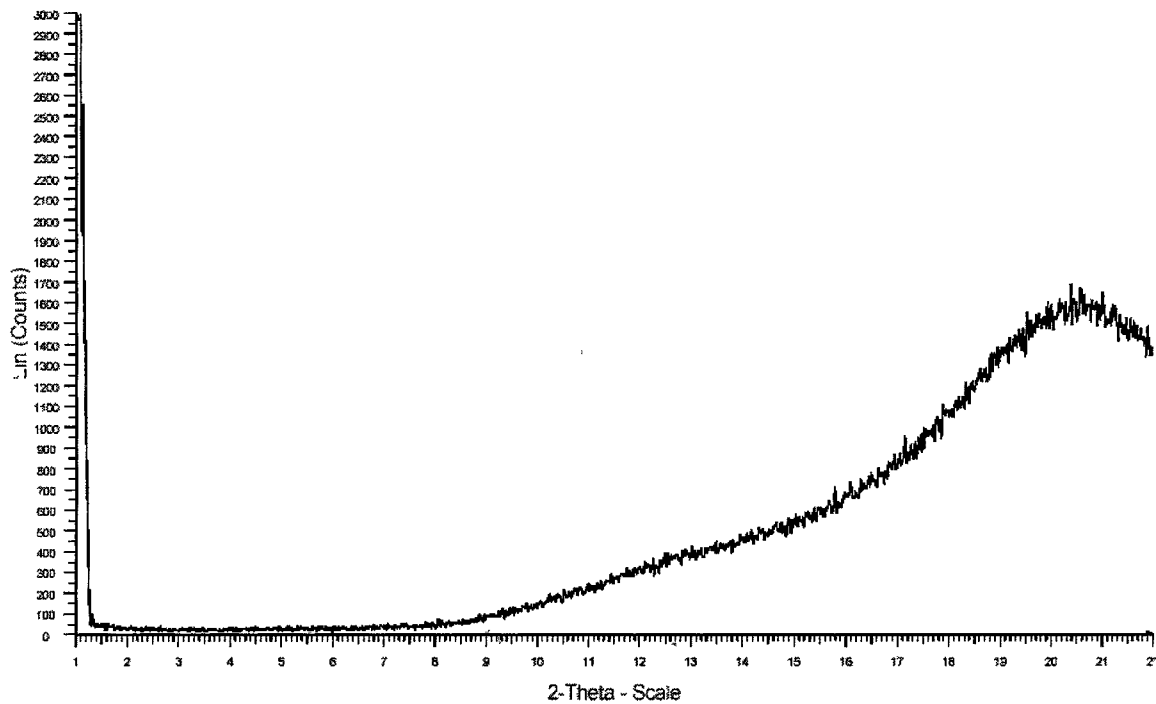
2. X-ray Diffraction of Nylon 6 at 0.5 % clay loading.



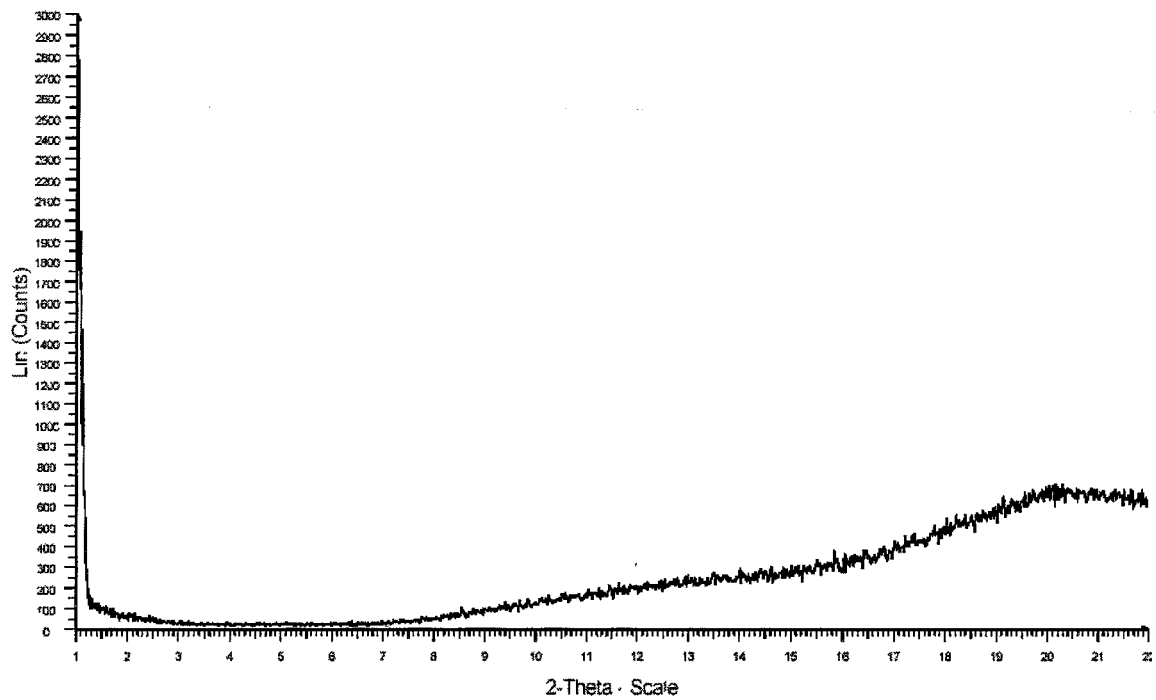
3. X-ray Diffraction of Nylon 6 at 2.0 % clay loading.



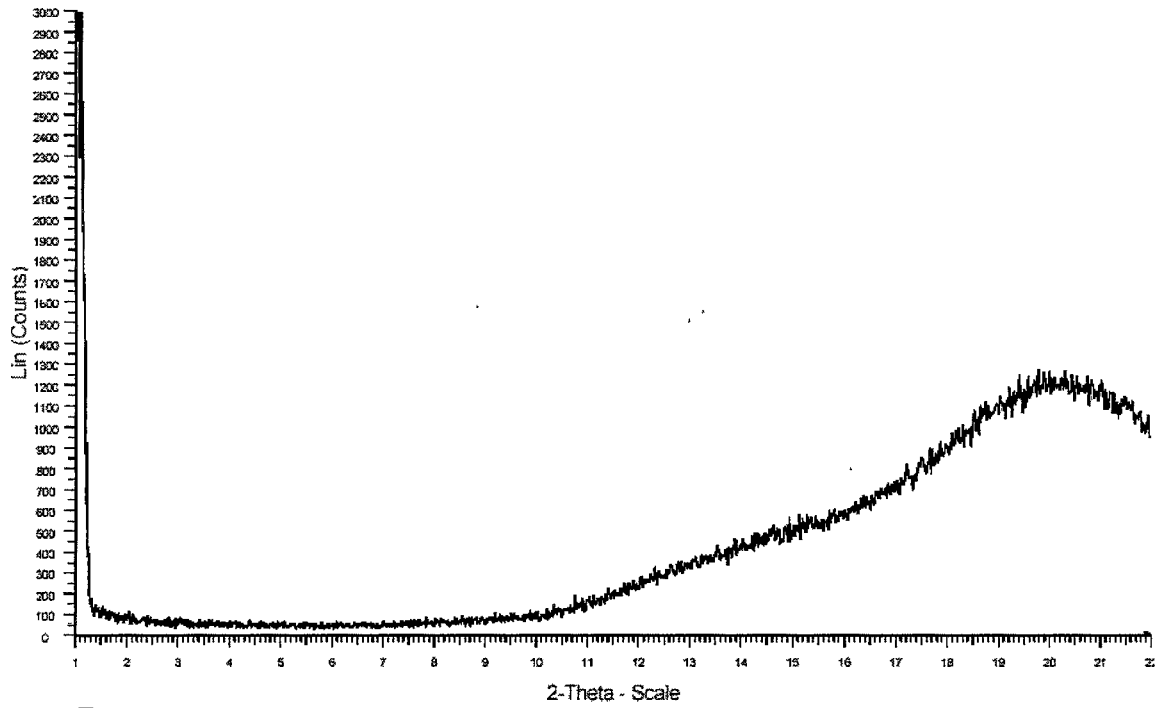
4. X-ray Diffraction of Nylon 6 at 5.0 % clay loading.



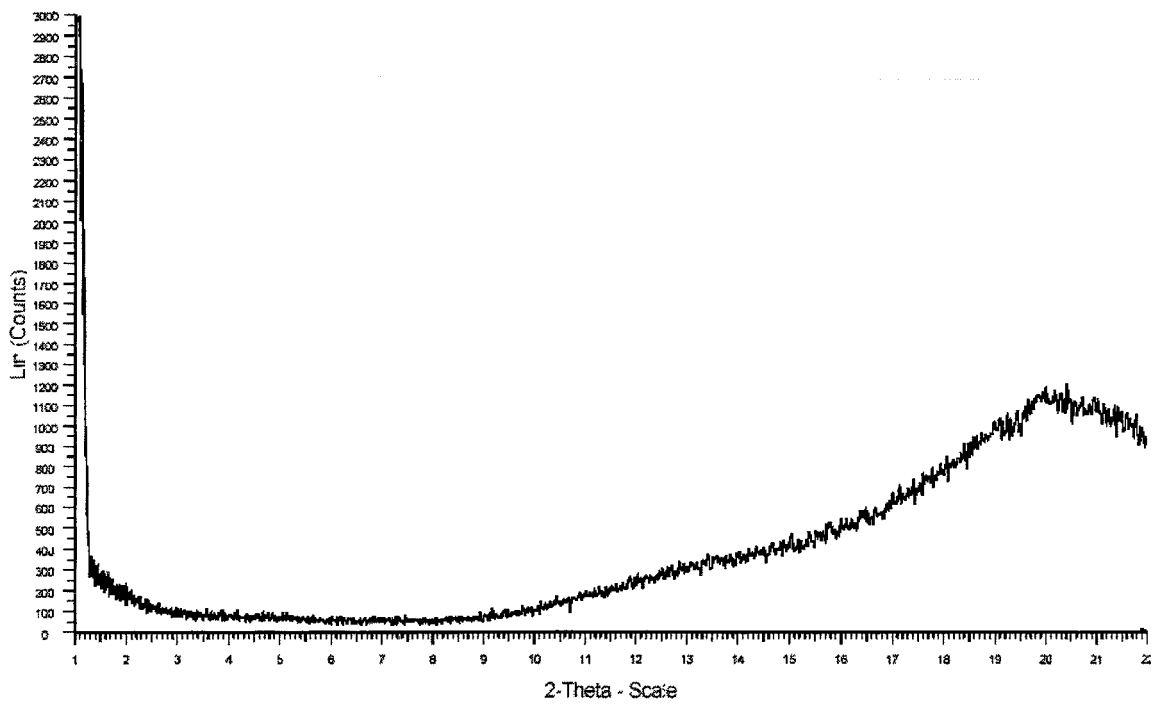
5. X-ray Diffraction of Nylon-MXD6.



6. X-ray Diffraction of Nylon-MXD6 at 0.5 % clay loading.



7. X-ray Diffraction of Nylon-MXD6 at 2.0 % clay loading.



8. X-ray Diffraction of Nylon-MXD6 at 5.0 % clay loading.

APPENDIX 2

Atomic Force Microscopy Analysis

1. 3-D AFM Surface Image of Nylon-MXD6 at 0.5 % Clay Loading at Time Zero
2. 2-D AFM Surface Image of Nylon-MXD6 at 0.5 % Clay Loading at Time Zero, green and blue lines represent topographical surface measurement.
3. Topographical Analysis of Nylon-MXD6 at 0.5 % Clay Loading at Time Zero, the graph represents the green line in 2.
4. Topographical Analysis of Nylon-MXD6 at 0.5 % Clay Loading at Time Zero, the graph represents the blue line in 2.
5. 3-D AFM Surface Image of Nylon-MXD6 at 0.5 % Clay Loading at Time 30 Minutes.
6. 2-D AFM Surface Image of Nylon-MXD6 at 0.5 % Clay Loading at Time 30 Minutes, green and blue lines represent topographical surface measurement.
7. Topographical analysis of Nylon-MXD6 at 0.5 % Clay Loading at Time 30 Minutes, the graph represents the blue line of 6.
8. Topographical analysis of Nylon-MXD6 at 0.5 % Clay Loading at Time 30 Minutes, the graph represents the blue line of 6.
9. 3-D AFM Surface Image of Nylon-MXD6 at 0.5 % Clay Loading at Time 1 Hour.
10. 2-D AFM Surface Image of Nylon-MXD6 at 0.5 % Clay Loading at Time 1 Hour, green and blue lines represent topographical surface measurement.
11. Topographical analysis of Nylon-MXD6 at 0.5 % Clay Loading at Time 1 Hour, the graph represents the green line of 10.
12. Topographical analysis of Nylon-MXD6 at 0.5 % Clay Loading at Time 1 Hour, the graph represents the blue line of 10.
13. 3-D AFM Surface Image of Nylon-MXD6 at 0.5 % Clay Loading at Time 2 Hours.

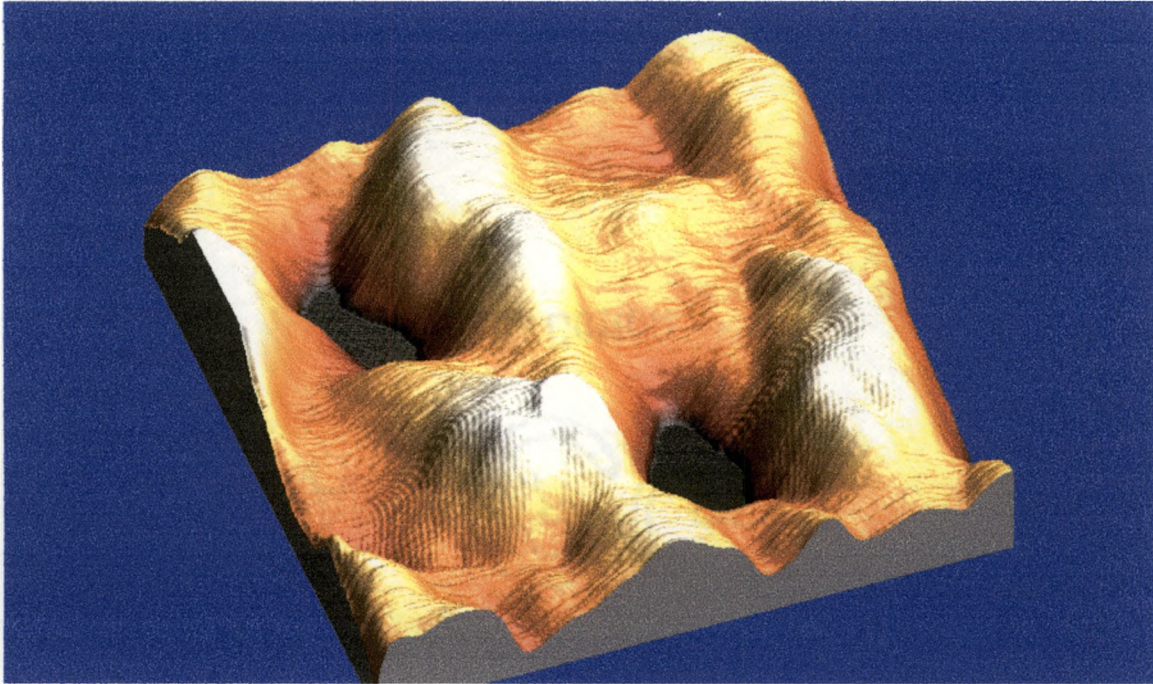
14. 2-D AFM Surface Image of Nylon-MXD6 at 0.5 % Clay Loading at Time 2 Hours, green and blue lines represent topographical surface measurement.
15. Topographical analysis of Nylon-MXD6 at 0.5 % Clay Loading at Time 2 Hours, the graph represents the blue line of 14.
16. Topographical analysis of Nylon-MXD6 at 0.5 % Clay Loading at Time 2 Hours, the graph represents the blue line of 14.
17. 3-D AFM Surface Image of Nylon-MXD6 at 2 % Clay Loading at Time Zero.
18. 2-D AFM Surface Image of Nylon-MXD6 at 2 % Clay Loading at Time Zero, green and blue lines represent topographical surface measurement.
19. Topographical analysis of Nylon-MXD6 at 0.5 % Clay Loading at Time Zero, the graph represents the green line of 18.
20. Topographical analysis of Nylon-MXD6 at 2 % Clay Loading at Time Zero, the graph represents the blue line of 18.
21. 3-D AFM Surface Image of Nylon-MXD6 at 2 % Clay Loading at Time 1 Hour.
22. 2-D AFM Image of Nylon-MXD6 at 2 % Clay Loading at Time 1 Hour, green and blue lines represent topographical surface measurement.
23. Topographical analysis of Nylon-MXD6 at 2 % Clay Loading at Time 1 Hour, the graph represents the green line of 22.
24. Topographical analysis of Nylon-MXD6 at 2 % Clay Loading at Time 1 Hour, the graph represents the blue line of 22.
25. 3-D AFM Surface Image of Nylon-MXD6 at 2 % Clay Loading at Time 2 Hours.
26. 2-D AFM Surface Image of Nylon-MXD6 at 2 % Clay Loading at Time 2 Hours, green and blue lines represent topographical surface measurement.
27. Topographical analysis of Nylon-MXD6 at 2 % Clay Loading at Time 2 Hours, the graph represents the green line of 26.
28. Topographical analysis of Nylon-MXD6 at 2 % Clay Loading at Time 2 Hours, the graph represents the blue line of 26.
29. 3-D AFM Surface Image of Nylon-MXD6 at 5 % Clay Loading at Time Zero.
30. 2-D AFM Surface Image of Nylon-MXD6 at 5 % Clay Loading at Time Zero, green and blue lines represent topographical surface measurement.

31. Topographical analysis of Nylon-MXD6 at 5 % Clay Loading at Time Zero, the graph represents the green line of 30.
32. Topographical analysis of Nylon-MXD6 at 5 % Clay Loading at Time Zero, the graph represents the blue line of 30.
33. Topographical analysis of Nylon-MXD6 at 5 % Clay Loading at Time Zero, the graph represents a cross section from 30.
34. 3-D AFM Surface Image of Nylon-MXD6 at 5 % Clay Loading at Time 1 Hour.
35. 2-D AFM Surface Image of Nylon-MXD6 at 5 % Clay Loading at Time 1 Hour, green and blue lines represent topographical surface measurement.
36. Topographical analysis of Nylon-MXD6 at 5 % Clay Loading at Time 1 Hour, the graph represents the green line of 35.
37. Topographical analysis of Nylon-MXD6 at 5 % Clay Loading at Time 1 Hour, the graph represents the blue line of 35.
38. 3-D AFM Surface Image of Nylon-MXD6 at 5 % Clay Loading at Time 2 Hours.
39. 2-D AFM Surface Image of Nylon-MXD6 at 5 % Clay Loading at Time 2 Hours, green and blue lines represent topographical surface measurement.
40. Topographical analysis of Nylon-MXD6 at 5 % Clay Loading at Time 2 Hours, the graph represents the green line of 39.
41. Topographical analysis of Nylon-MXD6 at 5 % Clay Loading at Time 2 Hours, the graph represents the green line of 39.
42. 3-D AFM Surface Image of Nylon 6 at 0.5 % Clay Loading at Time Zero.
43. 2-D AFM Surface Image of Nylon 6 at 0.5 % Clay Loading at Time Zero, green and blue lines represent topographical surface measurement.
44. Topographical analysis of Nylon 6 at 0.5 % Clay Loading at Time Zero, the graph represents the green line of 43.
45. Topographical analysis of Nylon 6 at 0.5 % Clay Loading at Time Zero, the graph represents the blue line of 43.
46. 3-D AFM Surface Image of Nylon 6 at 0.5 % Clay Loading at Time 30 Minutes.

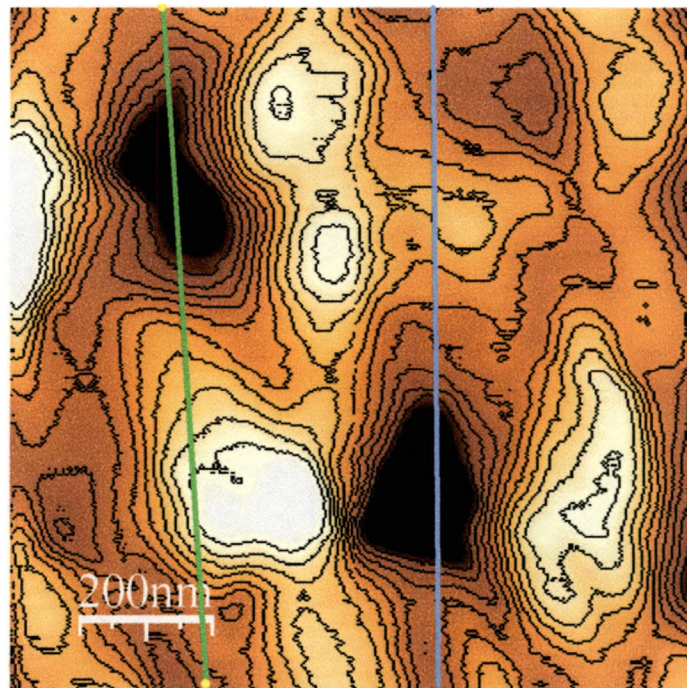
47. 2-D AFM Surface Image of Nylon 6 at 0.5 % Clay Loading at Time 30 Minutes, green and blue lines represent topographical surface measurement.
48. Topographical analysis of Nylon 6 at 0.5 % Clay Loading at Time 30 Minutes, the graph represents the green line of 47.
49. Topographical analysis of Nylon 6 at 0.5 % Clay Loading at Time 30 Minutes, the graph represents the blue line of 47.
50. 3-D AFM Surface Image of Nylon 6 at 0.5 % Clay Loading at Time 1 Hour.
51. 2-D AFM Surface Image of Nylon 6 at 0.5 % Clay Loading at Time 1 Hour, green and blue lines represent topographical surface measurement.
52. Topographical analysis of Nylon 6 at 0.5 % Clay Loading at Time 1 Hour, the graph represents the green line of 51.
53. Topographical analysis of Nylon 6 at 0.5 % Clay Loading at Time 1 Hour, the graph represents the blue line of 51.
54. 3-D AFM Surface Image of Nylon 6 at 0.5 % Clay Loading at Time 2 Hours.
55. 2-D AFM Surface Image of Nylon 6 at 0.5 % Clay Loading at Time 2 Hours, green and blue lines represent topographical surface measurement.
56. Topographical analysis of Nylon 6 at 0.5 % Clay Loading at Time 2 Hours, the graph represents the green line of 55.
57. Topographical analysis of Nylon 6 at 0.5 % Clay Loading at Time 2 Hours, the graph represents the blue line of 55.
58. 3-D AFM Surface Image of Nylon 6 at 2 % Clay Loading at Time Zero.
59. 2-D AFM Surface Image of Nylon 6 at 2 % Clay Loading at Time Zero, green and blue lines represent topographical surface measurement.
60. Topographical analysis of Nylon 6 at 2 % Clay Loading at Time Zero, the graph represents the green line of 59.
61. Topographical analysis of Nylon 6 at 2 % Clay Loading at Time Zero, the graph represents the blue line of 59.
62. 3-D AFM Surface Image of Nylon 6 at 2 % Clay Loading at Time 30 Minutes.
63. 2-D AFM Surface Image of Nylon 6 at 2 % Clay Loading at Time 30 Minutes, green and blue lines represent topographical surface measurement.

64. Topographical analysis of Nylon 6 at 2 % Clay Loading at Time 30 Minutes, the graph represents the green line of 63.
65. Topographical analysis of Nylon 6 at 2 % Clay Loading at Time 30 Minutes, the graph represents the blue line of 63.
66. 3-D AFM Surface Image of Nylon 6 at 2 % Clay Loading at Time 1 Hour.
67. 2-D AFM Surface Image of Nylon 6 at 2 % Clay Loading at Time 1 Hour, green and blue lines represent topographical surface measurement.
68. Topographical analysis of Nylon 6 at 2 % Clay Loading at Time 1 Hour, the graph represents the green line of 67.
69. Topographical analysis of Nylon 6 at 2 % Clay Loading at Time 1 Hour, the graph represents the blue line of 67.
70. 3-D AFM Surface Image of Nylon 6 at 2 % Clay Loading at Time 2 Hours.
71. 2-D AFM Surface Image of Nylon 6 at 2 % Clay Loading at Time 2 Hours, green and blue lines represent topographical surface measurement.
72. Topographical analysis of Nylon 6 at 2 % Clay Loading at Time 2 Hours, the graph represents the green line of 71.
73. Topographical analysis of Nylon 6 at 2 % Clay Loading at Time 2 Hours, the graph represents the blue line of 71.
74. 3-D AFM Surface Image of Nylon 6 at 5 % Clay Loading at Time Zero.
75. 2-D AFM Surface Image of Nylon 6 at 5 % Clay Loading at Time Zero, green and blue lines represent topographical surface measurement.
76. Topographical analysis of Nylon 6 at 5 % Clay Loading at Time Zero, the graph represents the green line of 75.
77. Topographical analysis of Nylon 6 at 5 % Clay Loading at Time Zero, the graph represents the blue line of 75.
78. 3-D AFM Surface Image of Nylon 6 at 5 % Clay Loading at Time 1 Hour.
79. 2-D AFM Surface Image of Nylon 6 at 5 % Clay Loading at Time 1 Hour, green and blue lines represent topographical surface measurement.

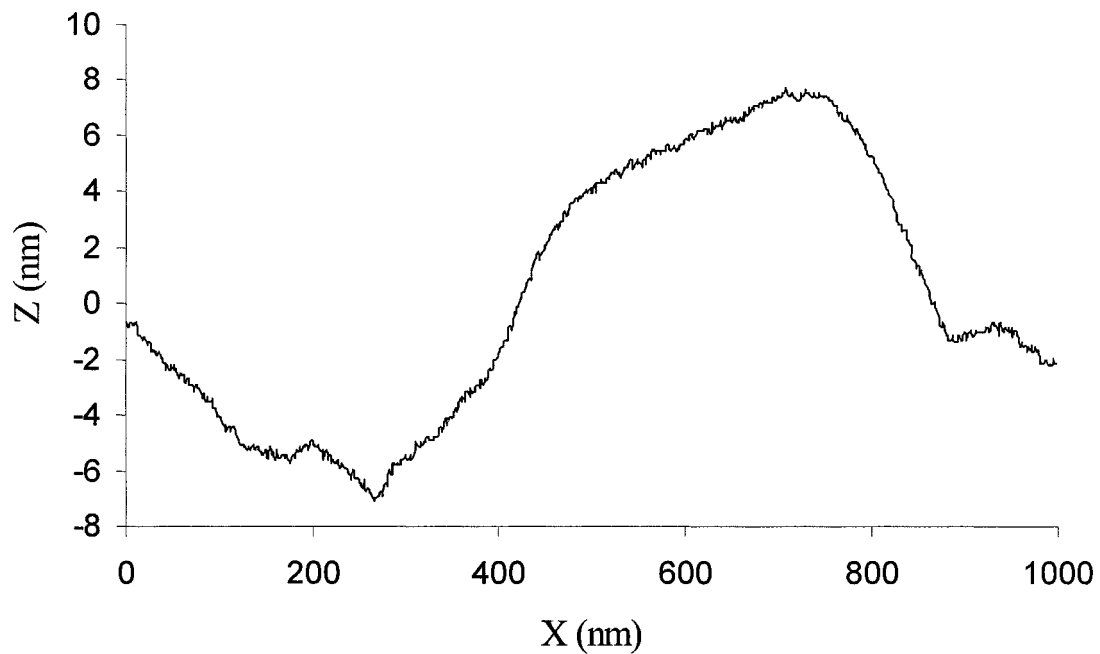
80. Topographical analysis of Nylon 6 at 5 % Clay Loading at Time 1 Hour, the graph represents the green line of 79.
81. Topographical analysis of Nylon 6 at 5 % Clay Loading at Time 1 Hour, the graph represents the blue line of 79.
82. 3-D AFM Surface Image of Nylon 6 at 5 % Clay Loading at Time 2 Hours.
83. 2-D AFM Surface Image of Nylon 6 at 5 % Clay Loading at Time 2 Hours, green and blue lines represent topographical surface measurement.
84. Topographical analysis of Nylon 6 at 5 % Clay Loading at Time 2 Hours, the graph represents the green line of 83.
85. Topographical analysis of Nylon 6 at 5 % Clay Loading at Time 2 Hours, the graph represents the blue line of 83.



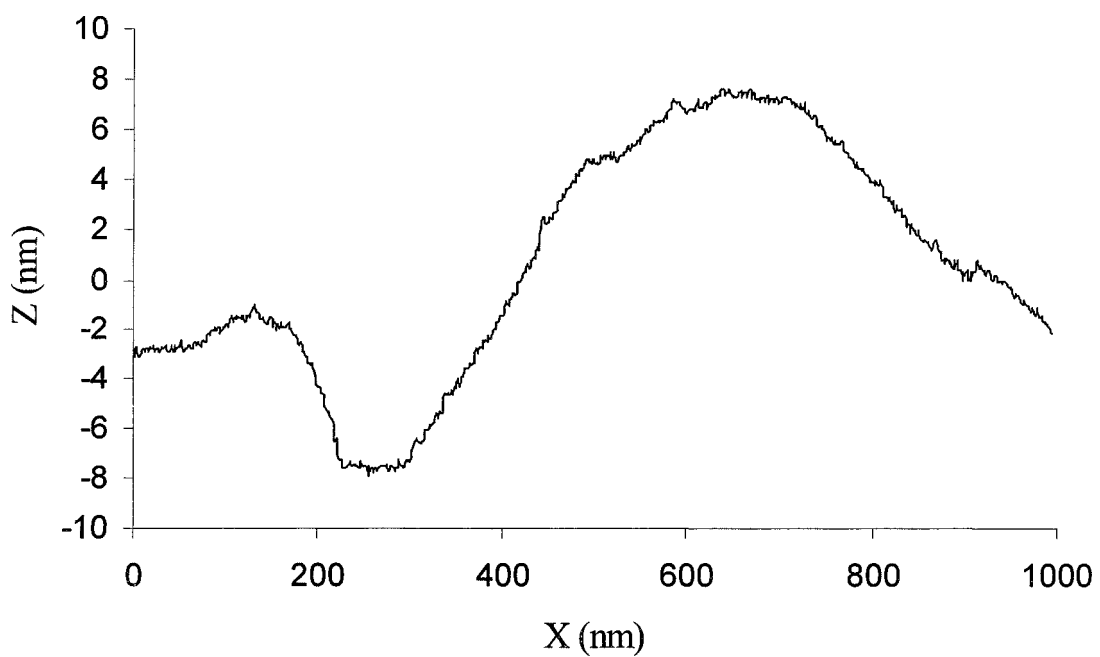
1. 3-D AFM Surface Image of Nylon-MXD6 at 0.5 % Clay Loading at Time Zero.



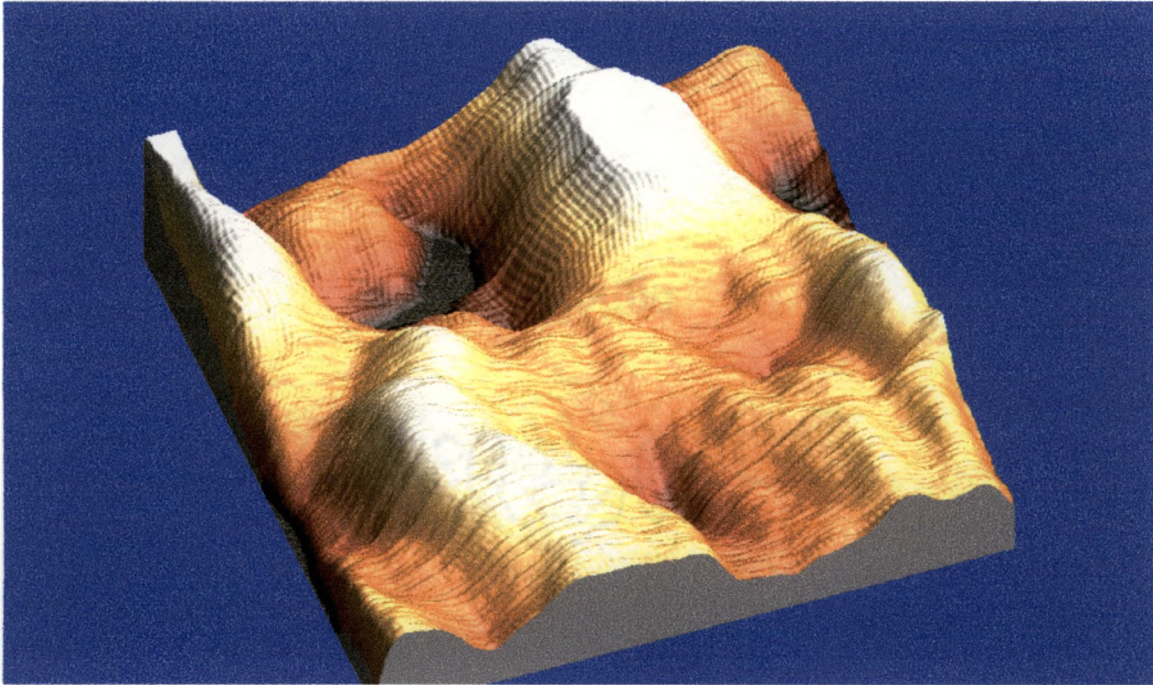
2. 2-D AFM Surface Image of Nylon-MXD6 at 0.5 % Clay Loading at Time Zero, green and blue lines represent topographical surface measurement.



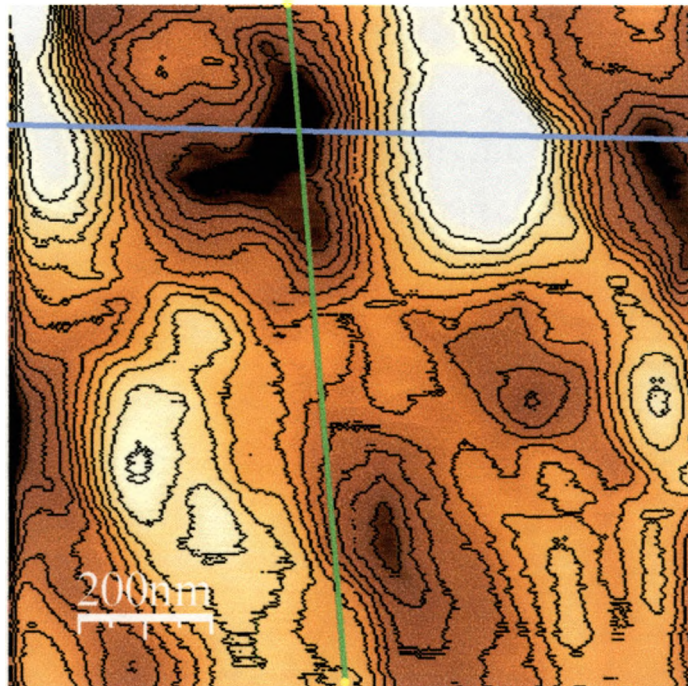
3. Topographical Analysis of Nylon-MXD6 at 0.5 % Clay Loading at Time Zero, the graph represents the green line of 2.



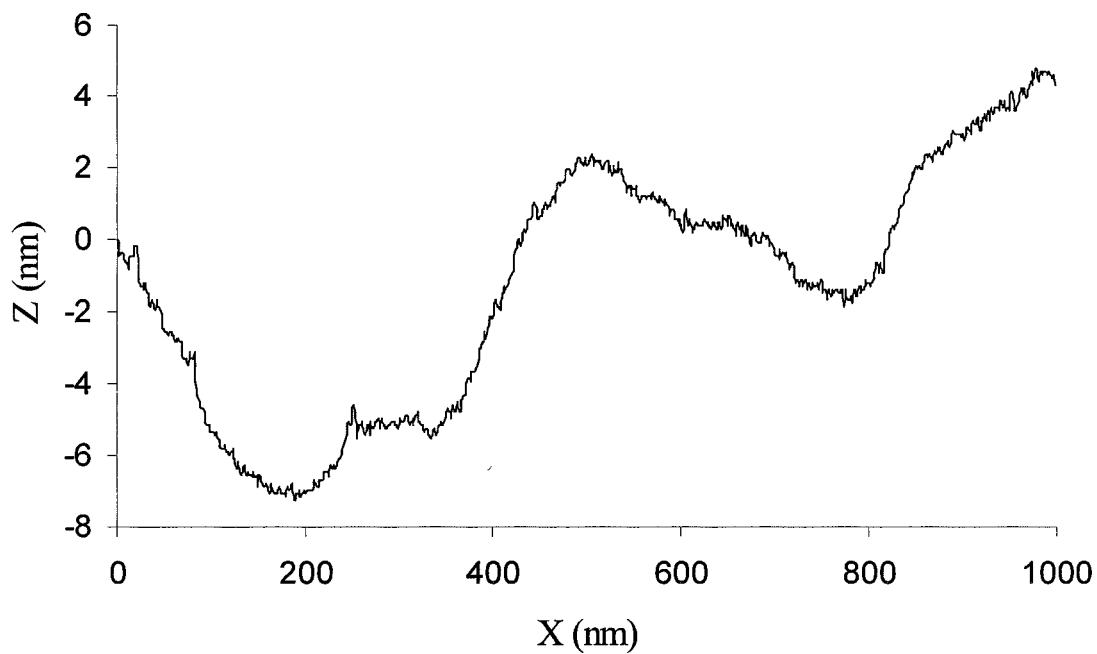
4. Topographical Analysis of Nylon-MXD6 at 0.5 % Clay Loading at Time Zero, the graph represents the blue line of 2.



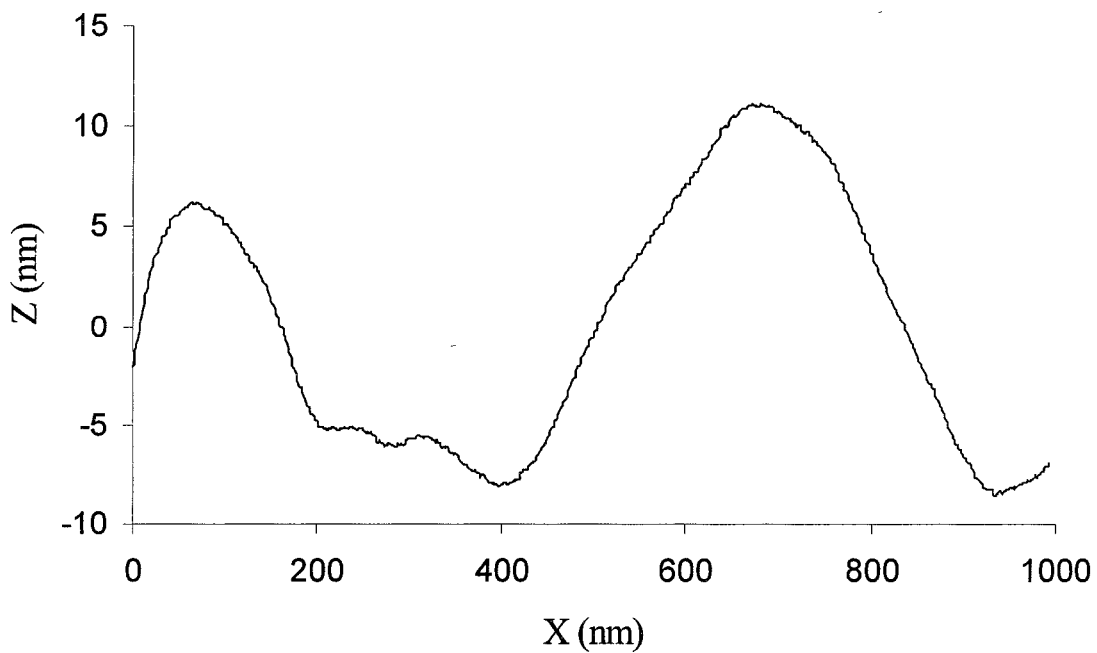
5. 3-D AFM Surface Image of Nylon-MXD6 at 0.5 % Clay Loading at Time 30 Minutes.



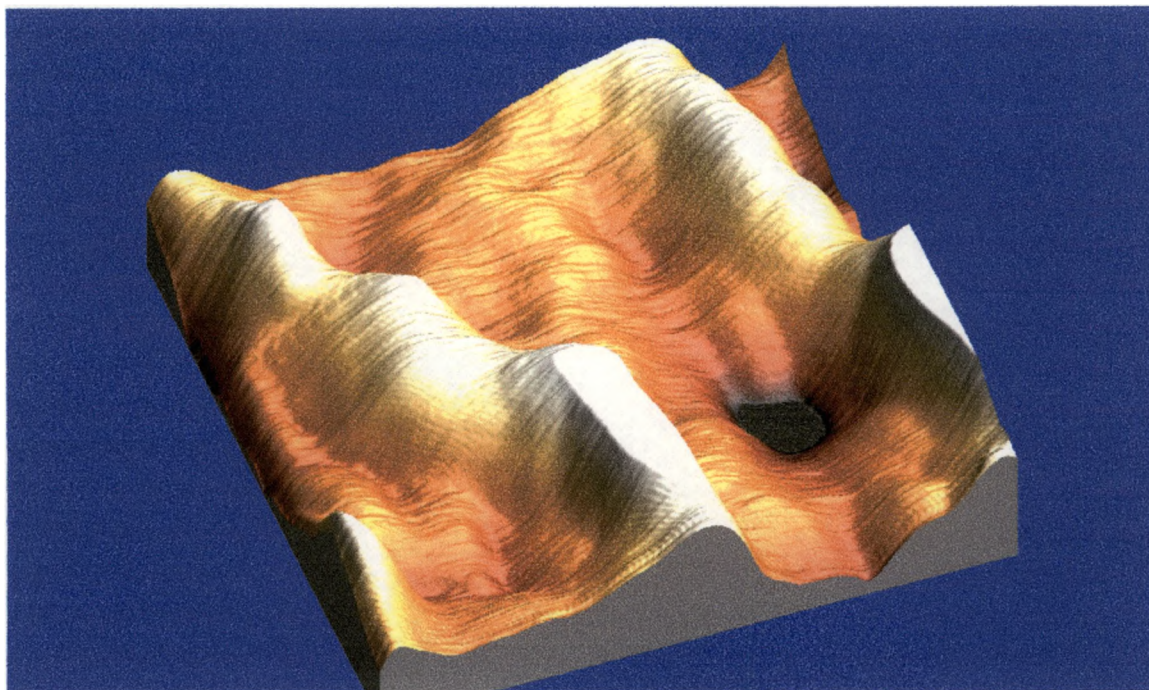
6. 2-D AFM Surface Image of Nylon-MXD6 at 0.5 % Clay Loading at Time 30 Minutes, green and blue lines represent topographical surface measurement.



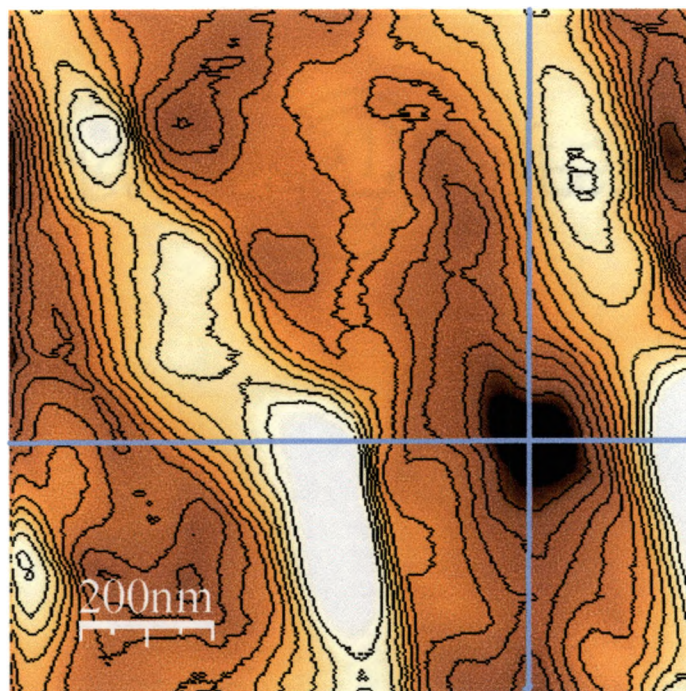
7. Topographical analysis of Nylon-MXD6 at 0.5 % Clay Loading at Time 30 Minutes, the graph represents the blue line of 6.



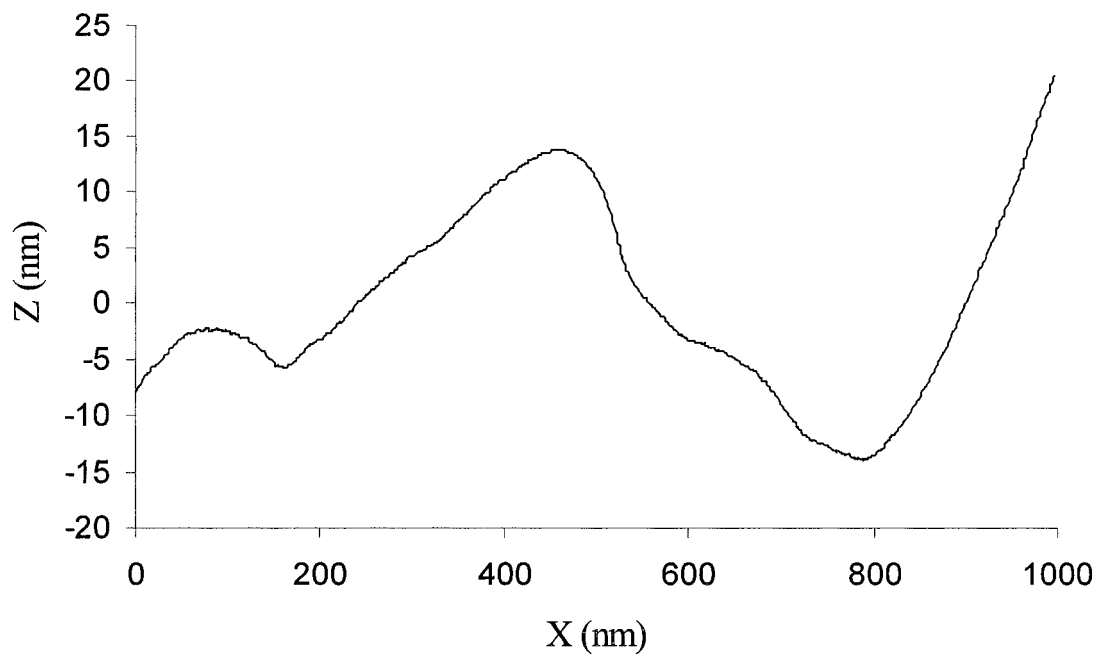
8. Topographical analysis of Nylon-MXD6 at 0.5 % Clay Loading at Time 30 Minutes, the graph represents the blue line of 6.



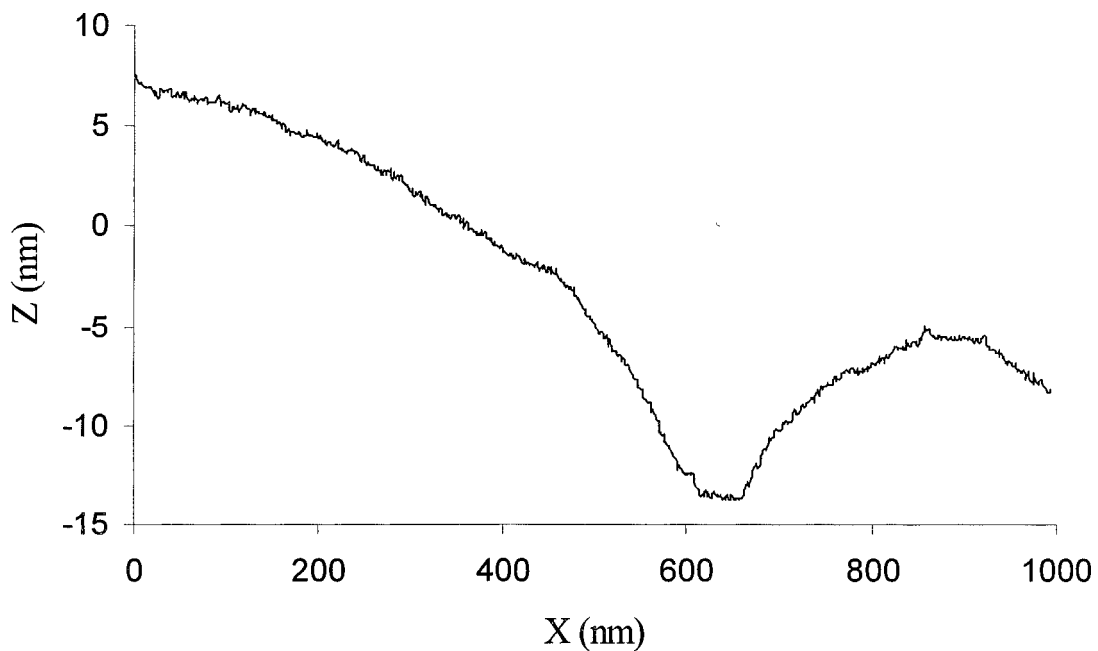
9. 3-D AFM Surface Image of Nylon-MXD6 at 0.5 % Clay Loading at Time 1 Hour.



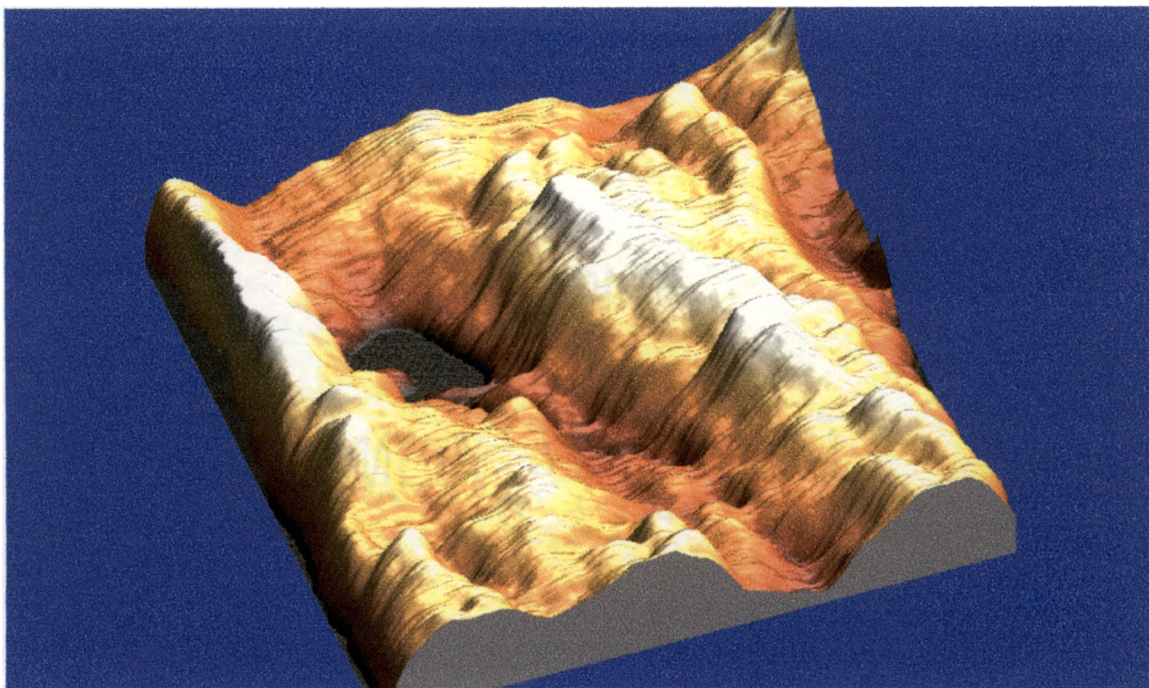
10. 2-D AFM Surface Image of Nylon-MXD6 at 0.5 % Clay Loading at Time 1 Hour, green and blue lines represent topographical surface measurement.



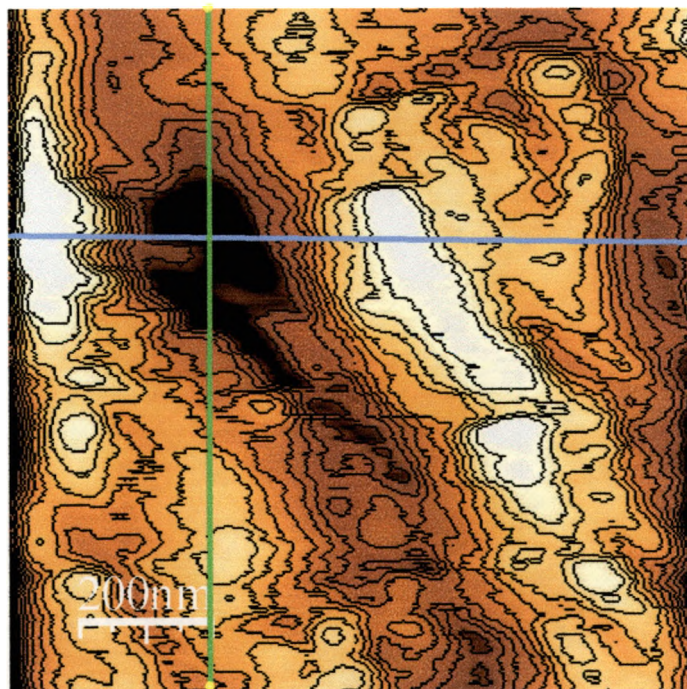
11. Topographical analysis of Nylon-MXD6 at 0.5 % Clay Loading at Time 1 Hour, the graph represents the green line of 10.



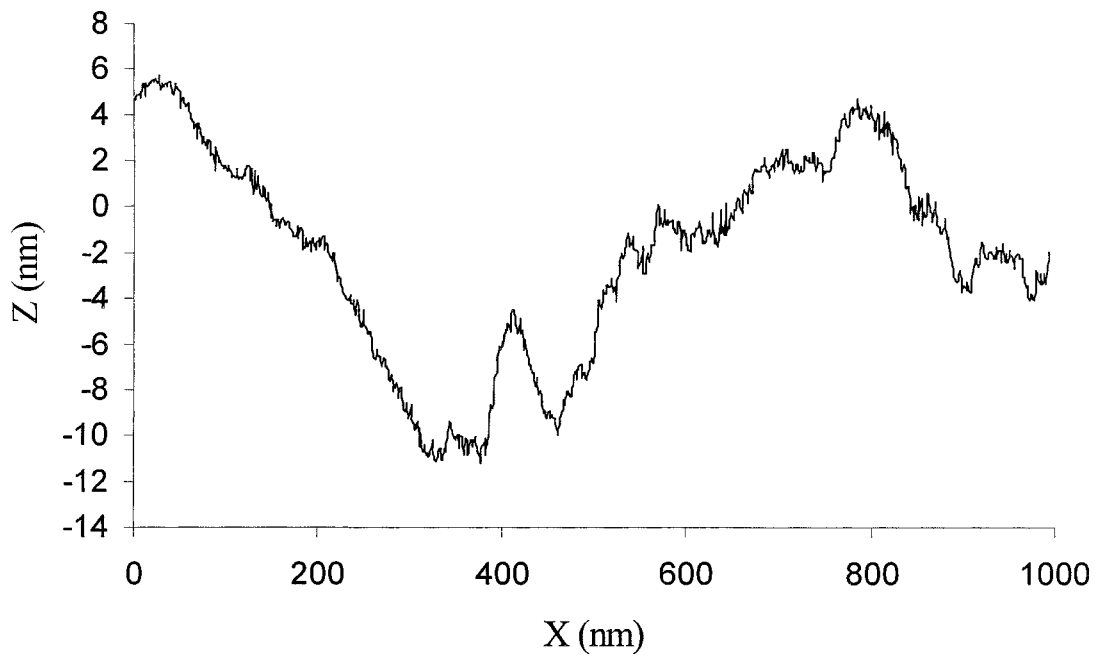
12. Topographical analysis of Nylon-MXD6 at 0.5 % Clay Loading at Time 1 Hour, the graph represents the blue line of 10.



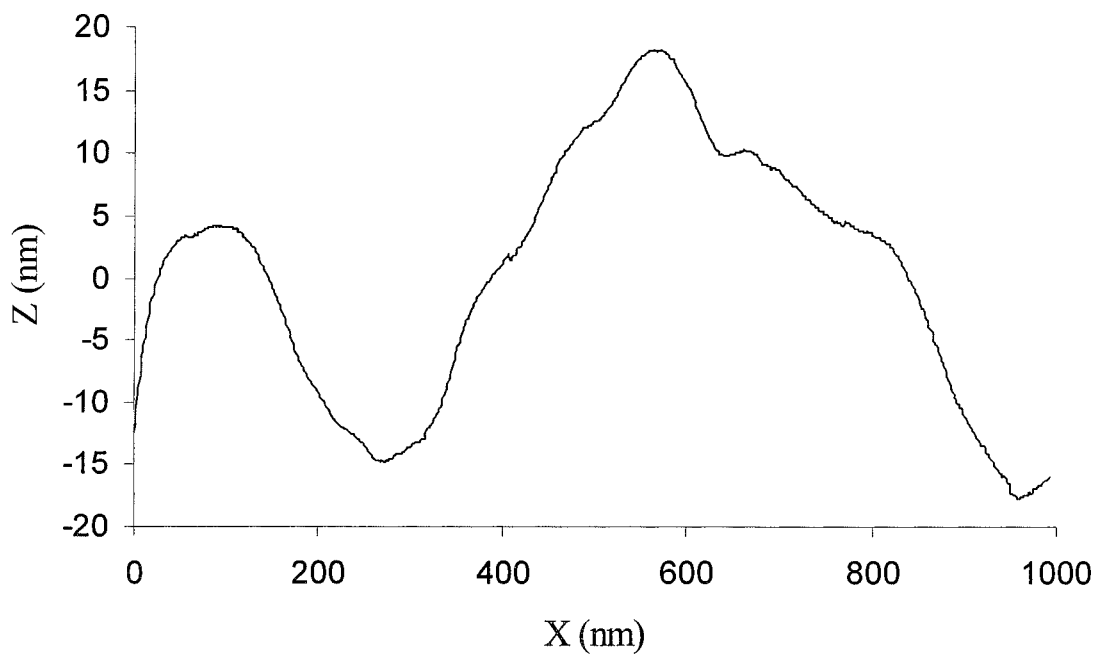
13. 3-D AFM Surface Image of Nylon-MXD6 at 0.5 % Clay Loading at Time 2 Hours.



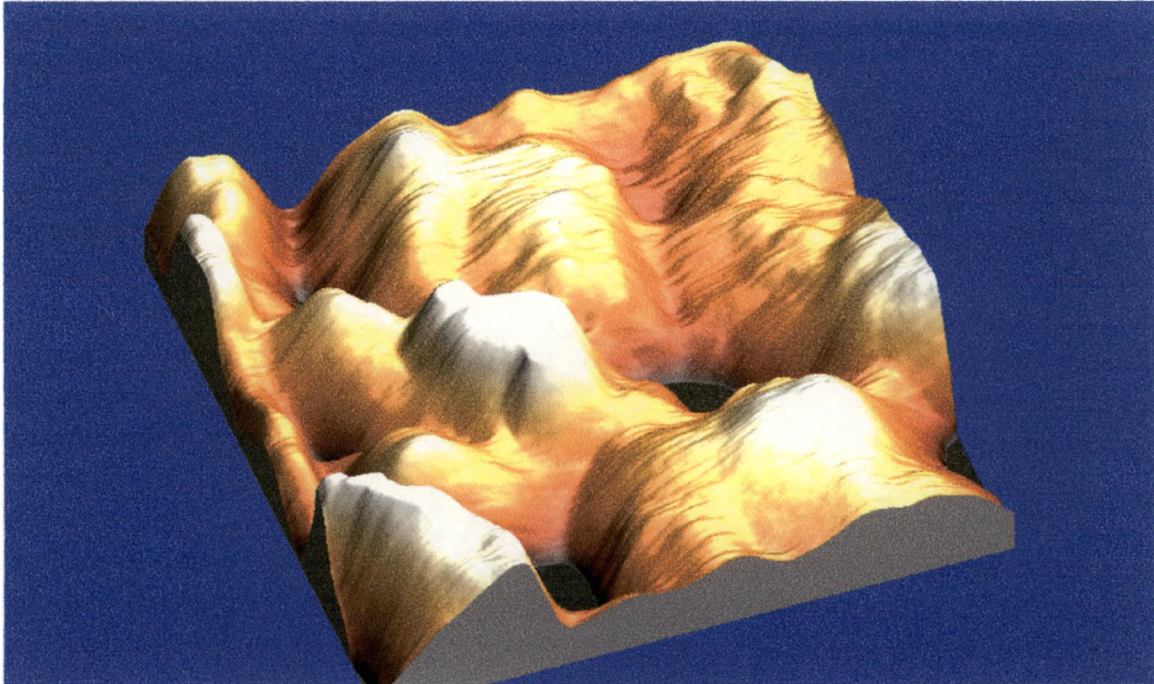
14. 2-D AFM Surface Image of Nylon-MXD6 at 0.5 % Clay Loading at Time 2 Hours, green and blue lines represent topographical surface measurement.



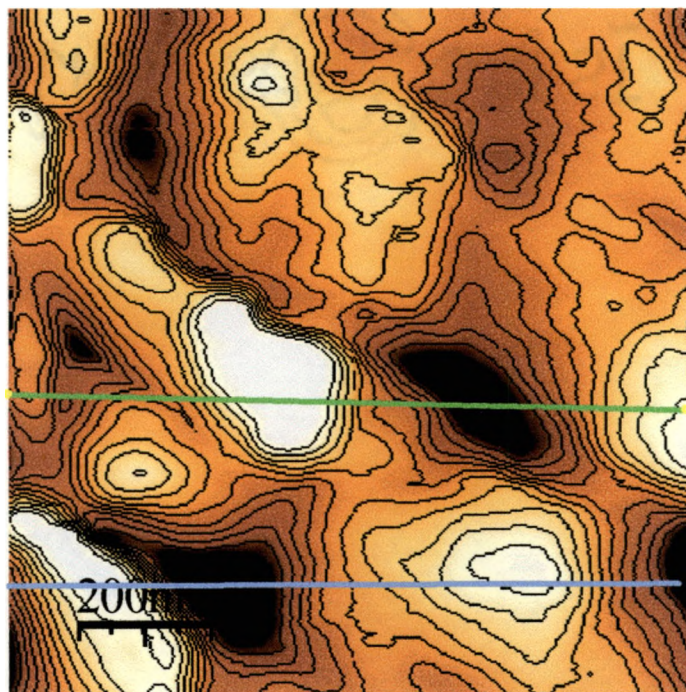
15. Topographical analysis of Nylon-MXD6 at 0.5 % Clay Loading at Time 2 Hours, the graph represents the blue line of 14.



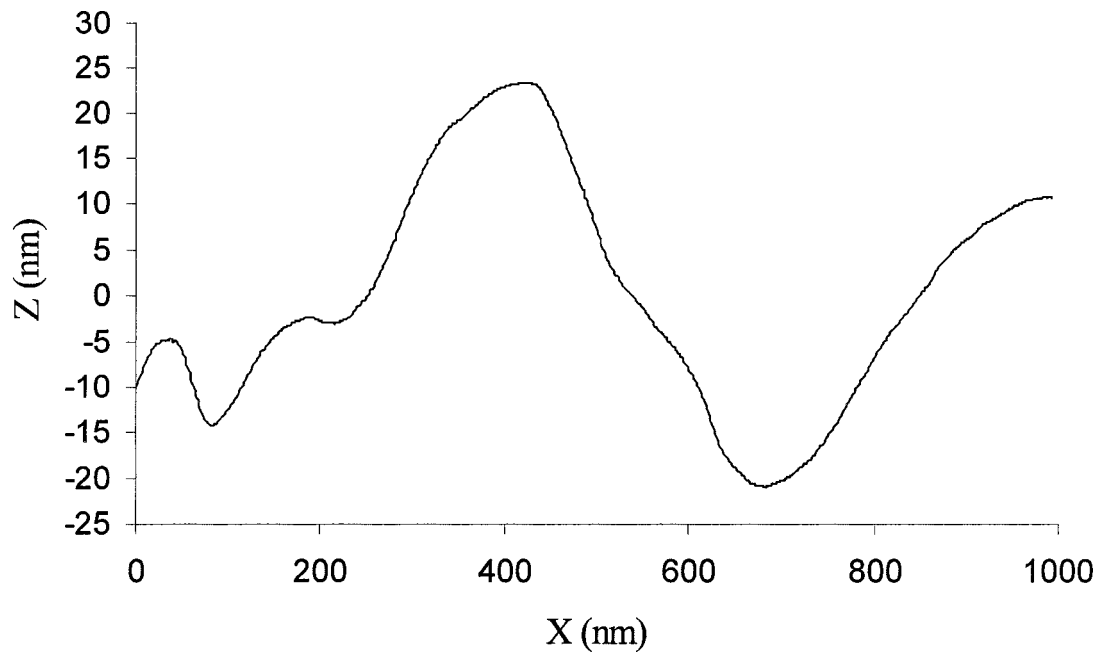
16. Topographical analysis of Nylon-MXD6 at 0.5 % Clay Loading at Time 2 Hours, the graph represents the green line of 14.



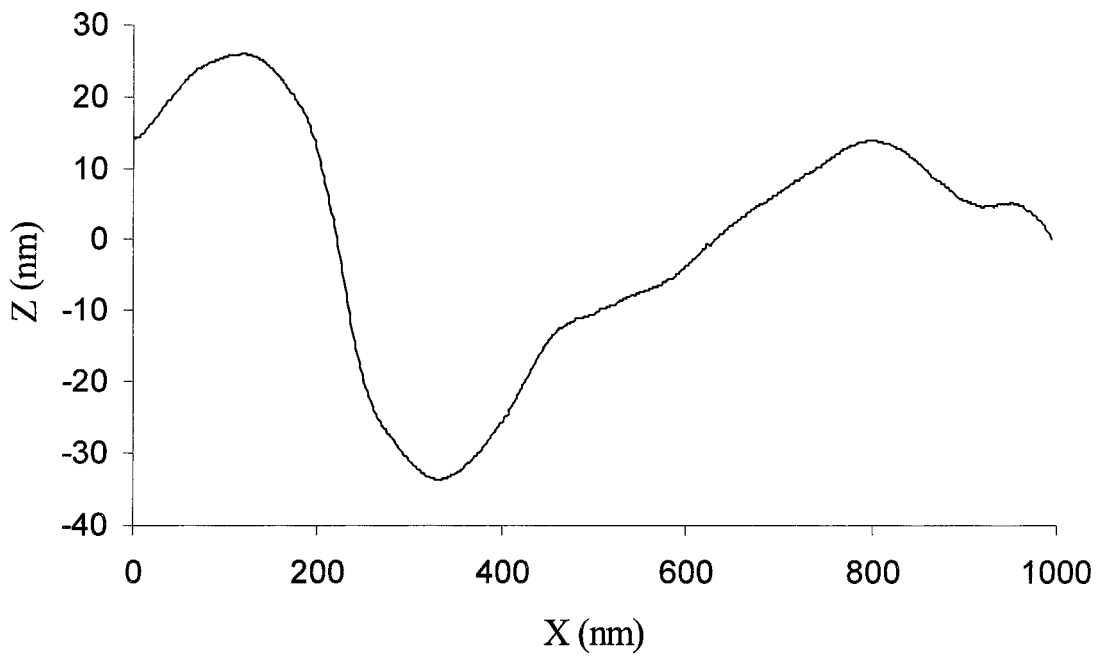
17. 3-D AFM Surface Image of Nylon-MXD6 at 2 % Clay Loading at Time Zero.



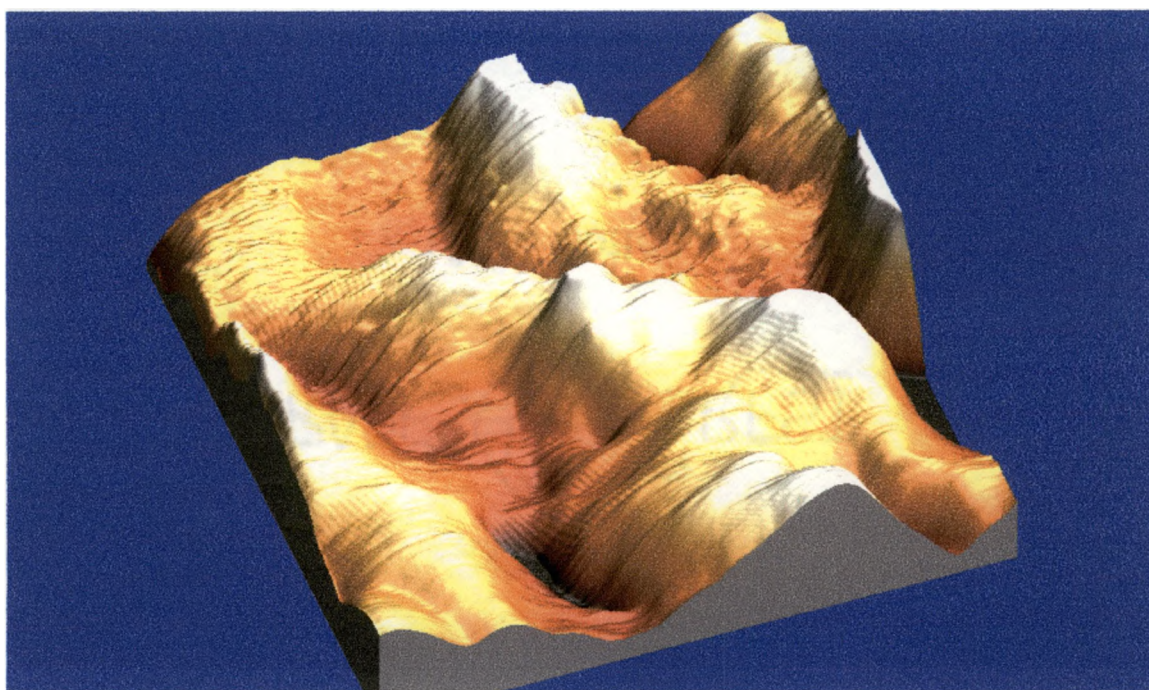
18. 2-D AFM Surface Image of Nylon-MXD6 at 2 % Clay Loading at Time Zero, green and blue lines represent topographical surface measurement.



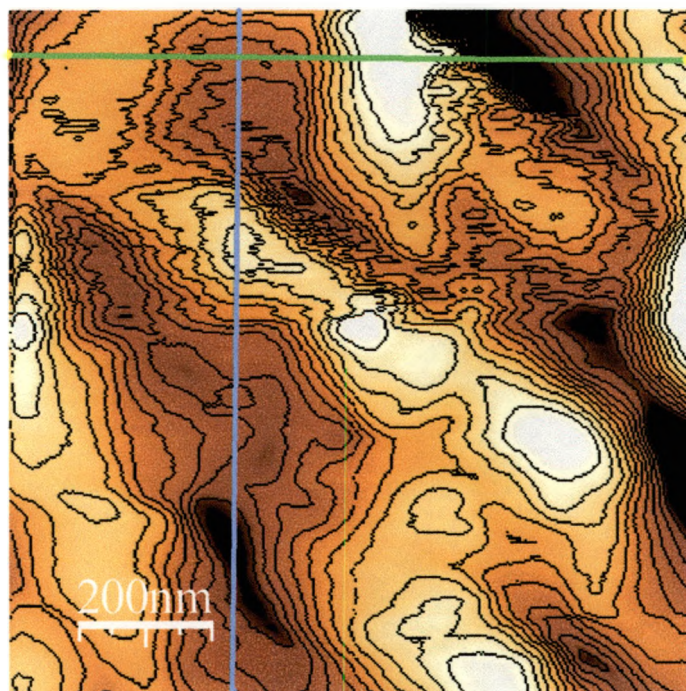
19. Topographical analysis of Nylon-MXD6 at 2 % Clay Loading at Time Zero, the graph represents the green line of 18.



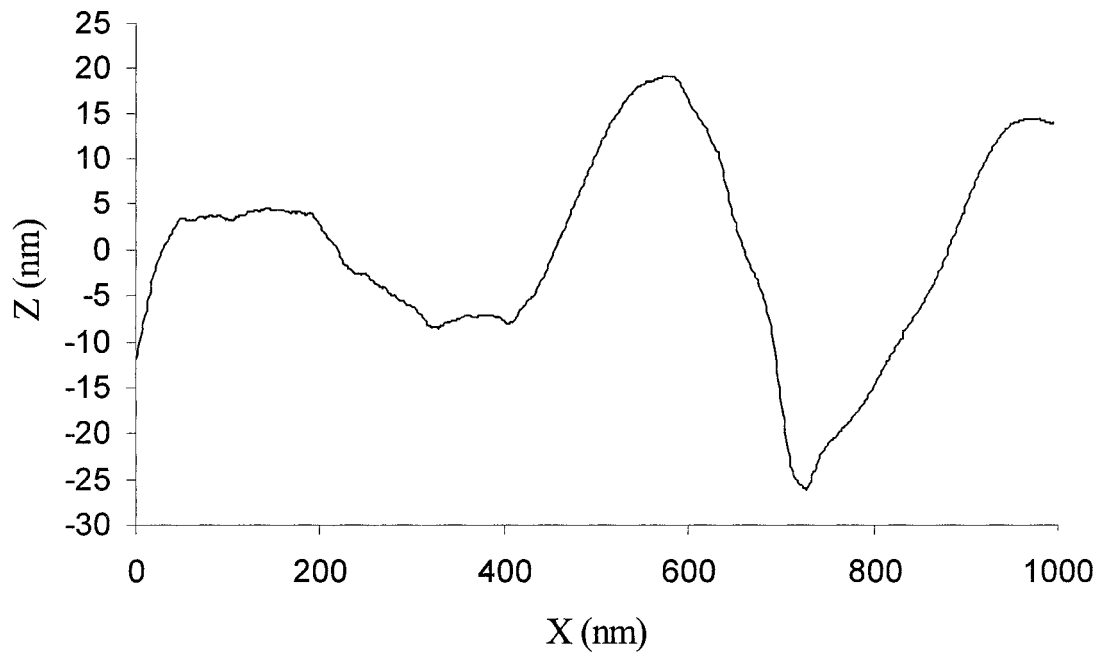
20. Topographical analysis of Nylon-MXD6 at 2 % Clay Loading at Time Zero, the graph represents the blue line of 18.



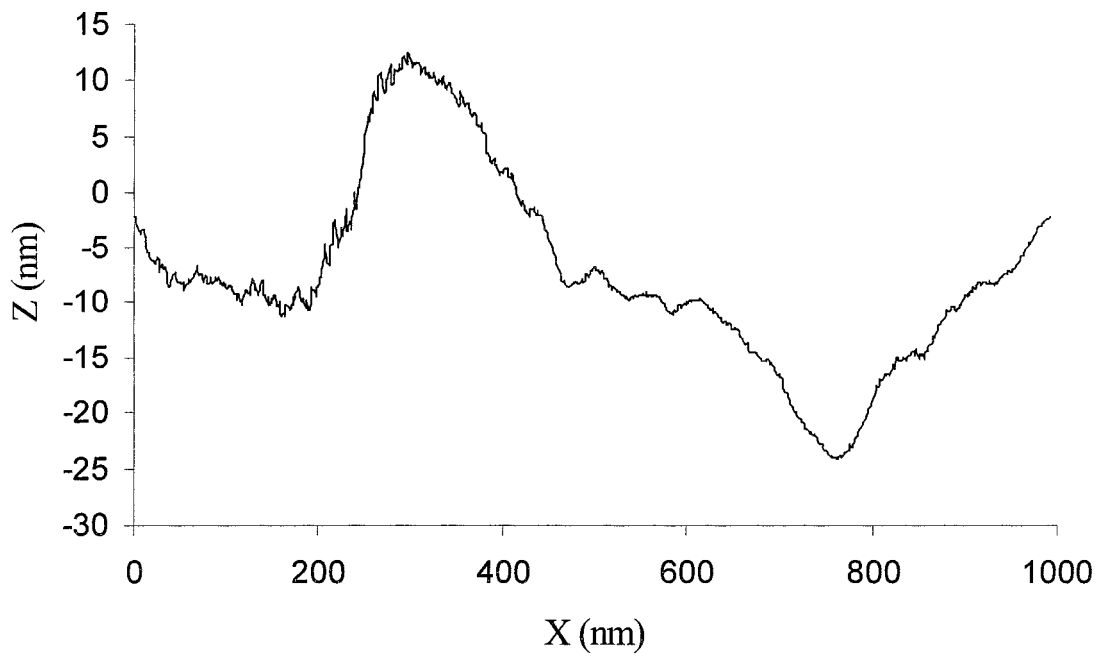
21. 3-D AFM Surface Image of Nylon-MXD6 at 2 % Clay Loading at Time 1 Hour.



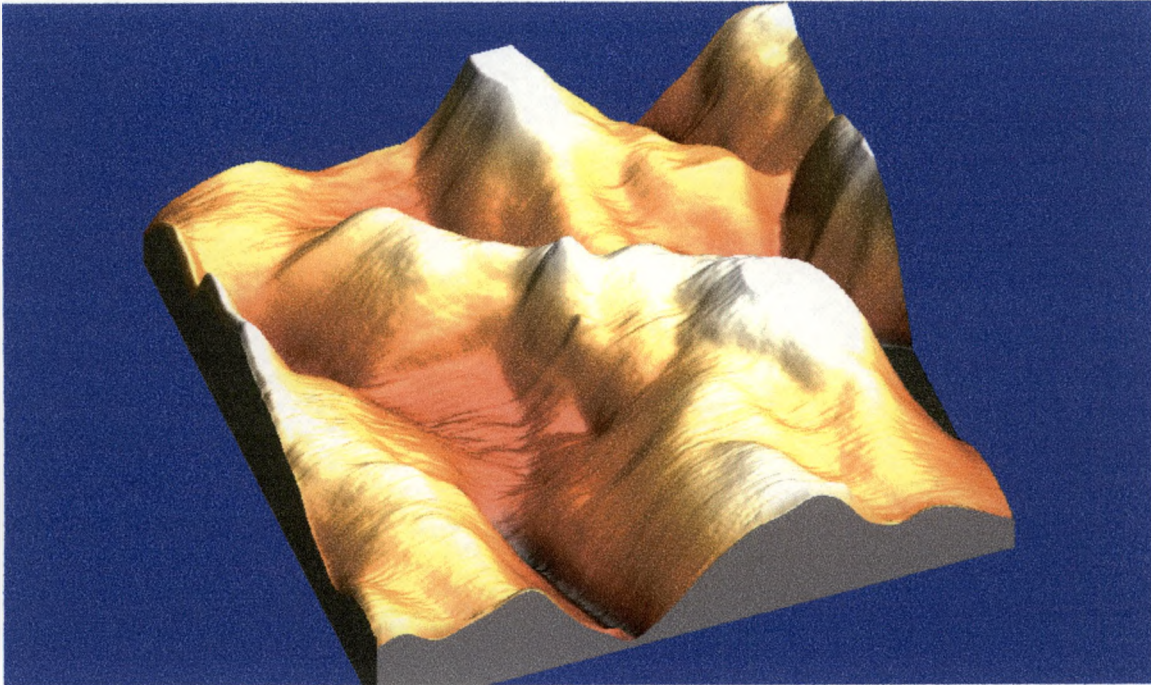
22. 2-D AFM Image of Nylon-MXD6 at 2 % Clay Loading at Time 1 Hour, green and blue lines represent topographical surface measurement.



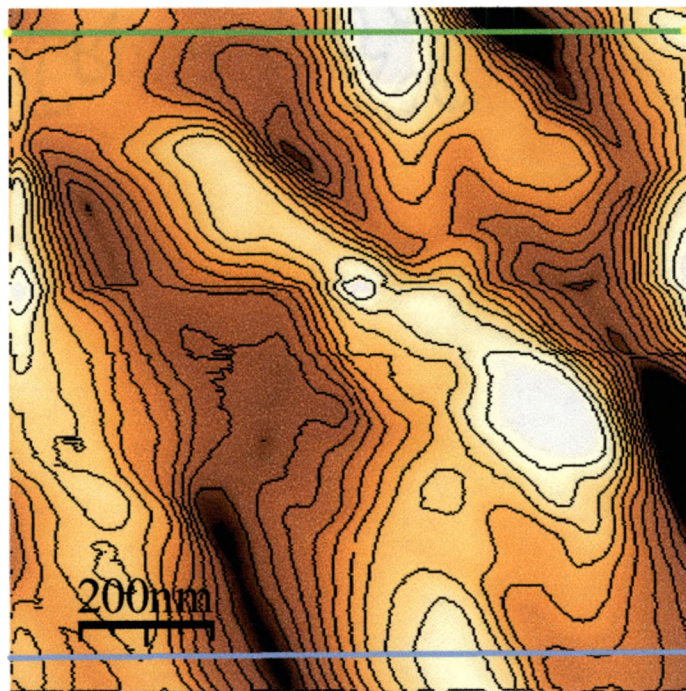
23. Topographical analysis of Nylon-MXD6 at 2 % Clay Loading at Time 1 Hour, the graph represents the green line of 22.



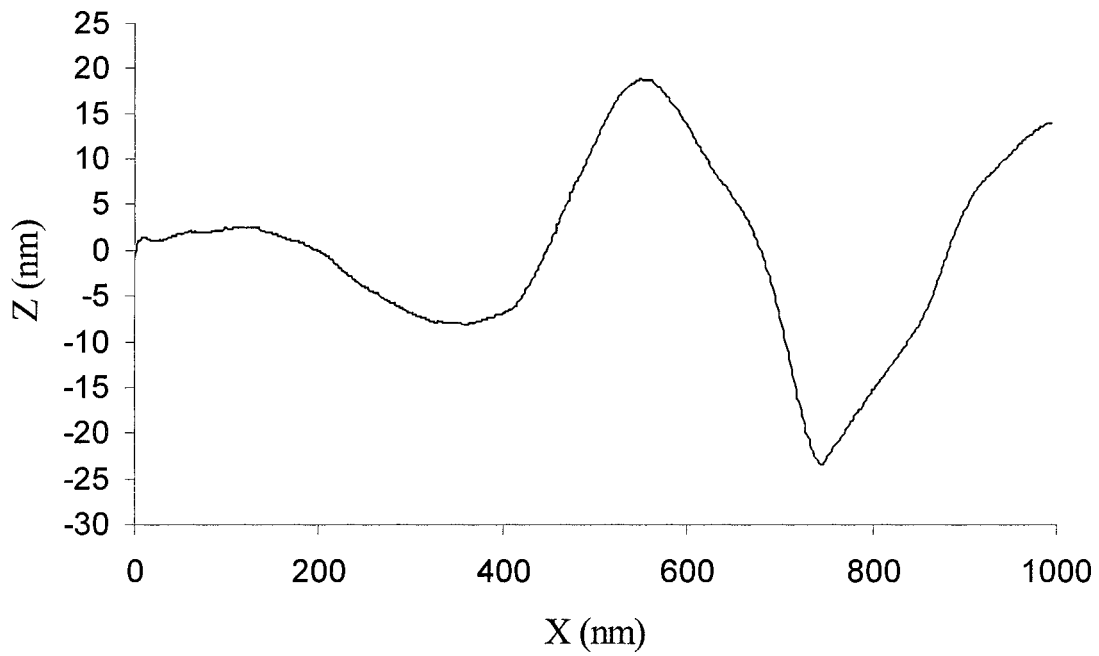
24. Topographical analysis of Nylon-MXD6 at 2 % Clay Loading at Time 1 Hour, the graph represents the blue line of 22.



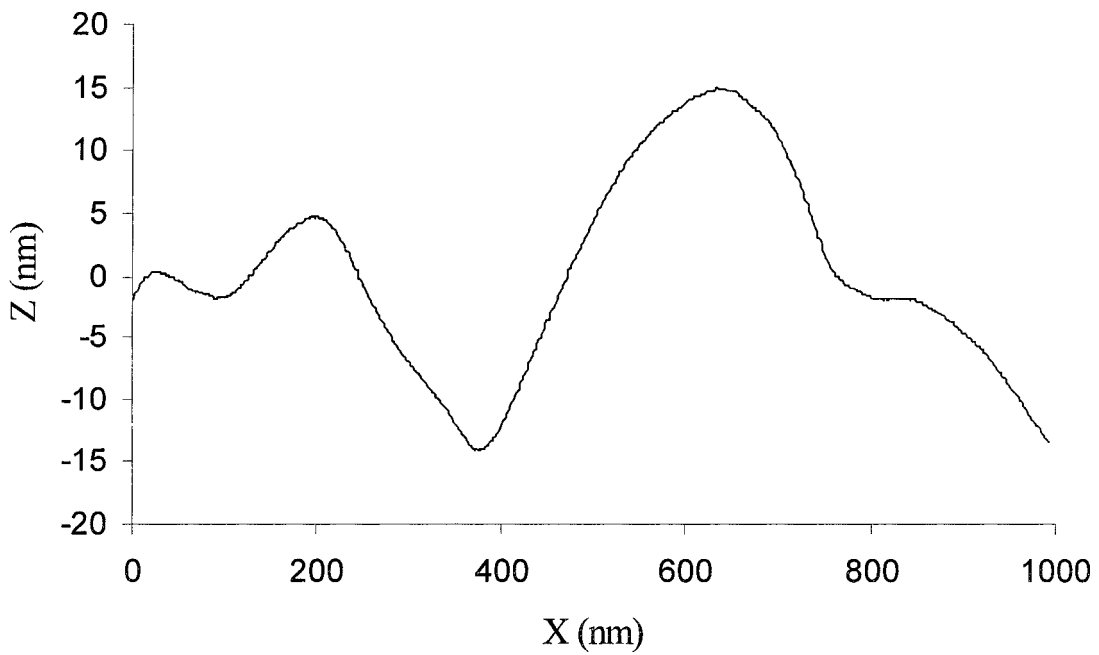
25. 3-D AFM Surface Image of Nylon-MXD6 at 2 % Clay Loading at Time 2 Hours.



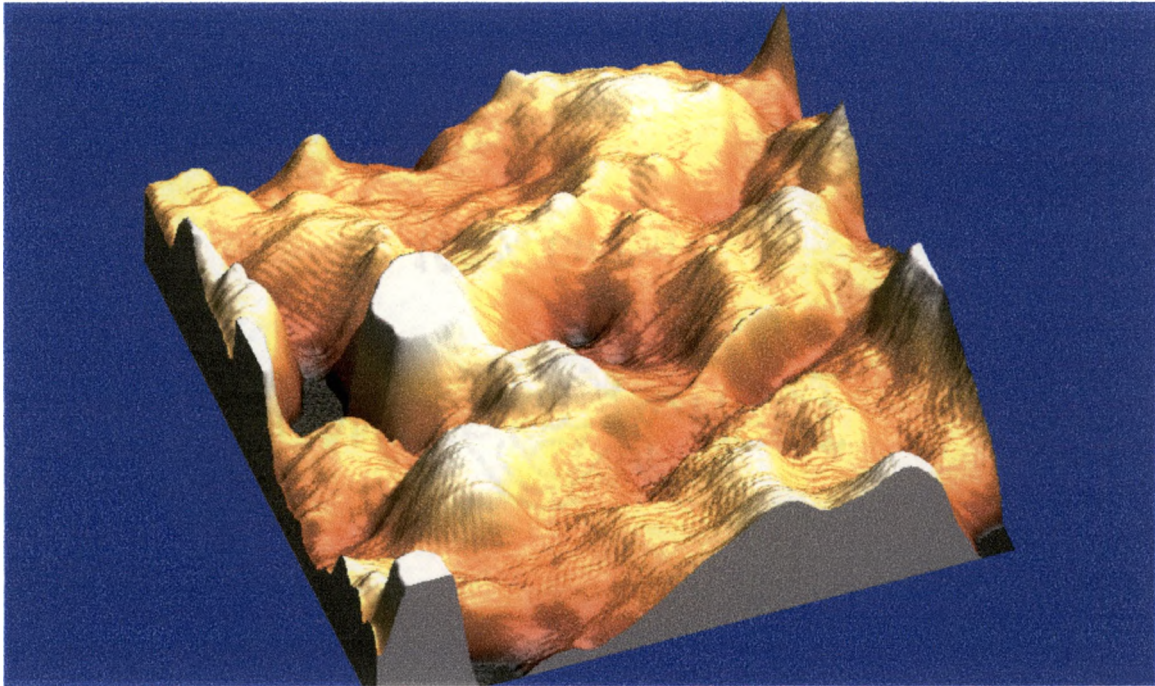
26. 2-D AFM Surface Image of Nylon-MXD6 at 2 % Clay Loading at Time 2 Hours, green and blue lines represent topographical surface measurement.



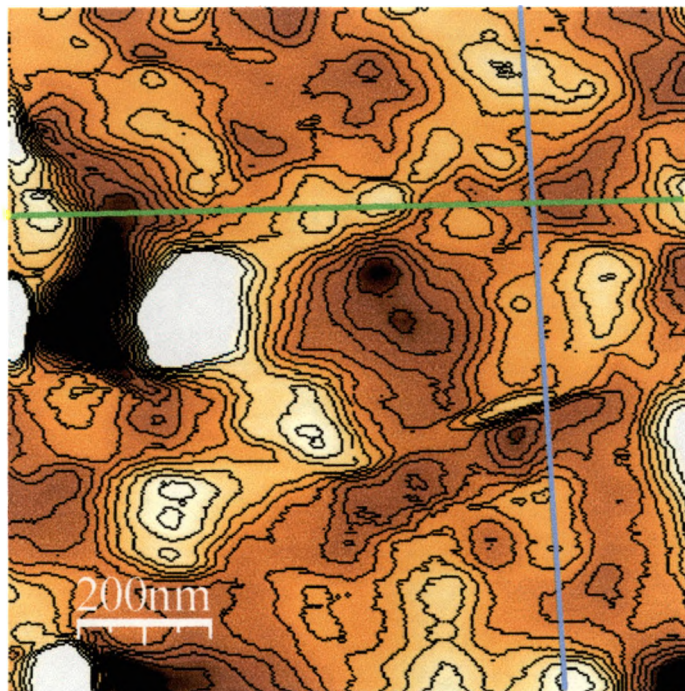
27. Topographical analysis of Nylon-MXD6 at 2 % Clay Loading at Time 2 Hours, the graph represents the green line of 26.



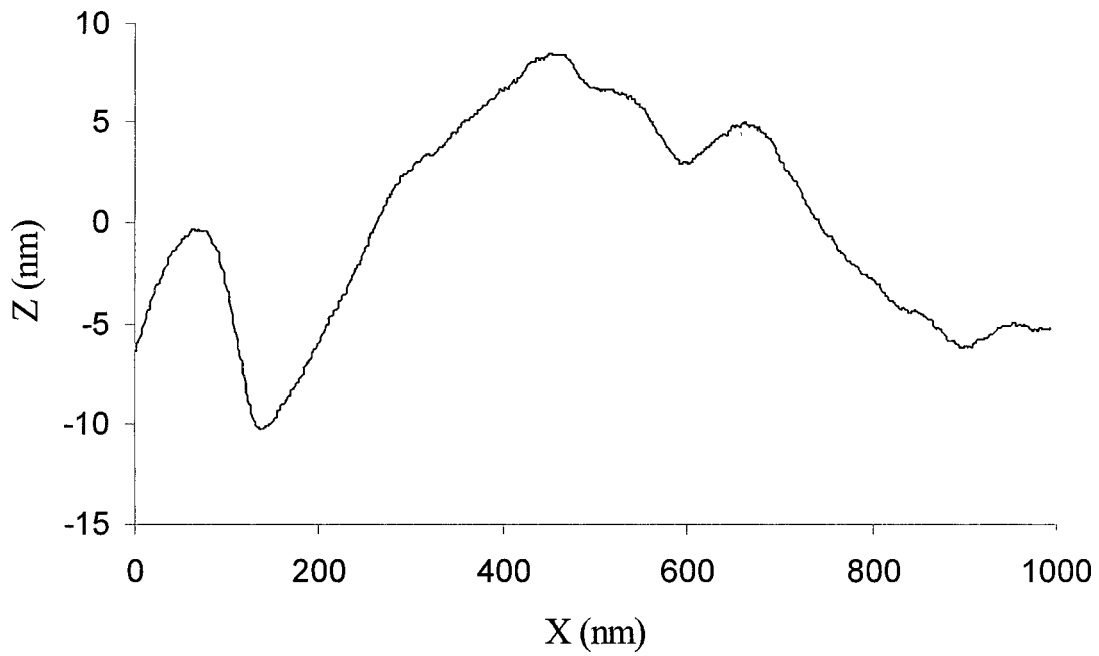
28. Topographical analysis of Nylon-MXD6 at 2 % Clay Loading at Time 2 Hours, the graph represents the blue line of 26.



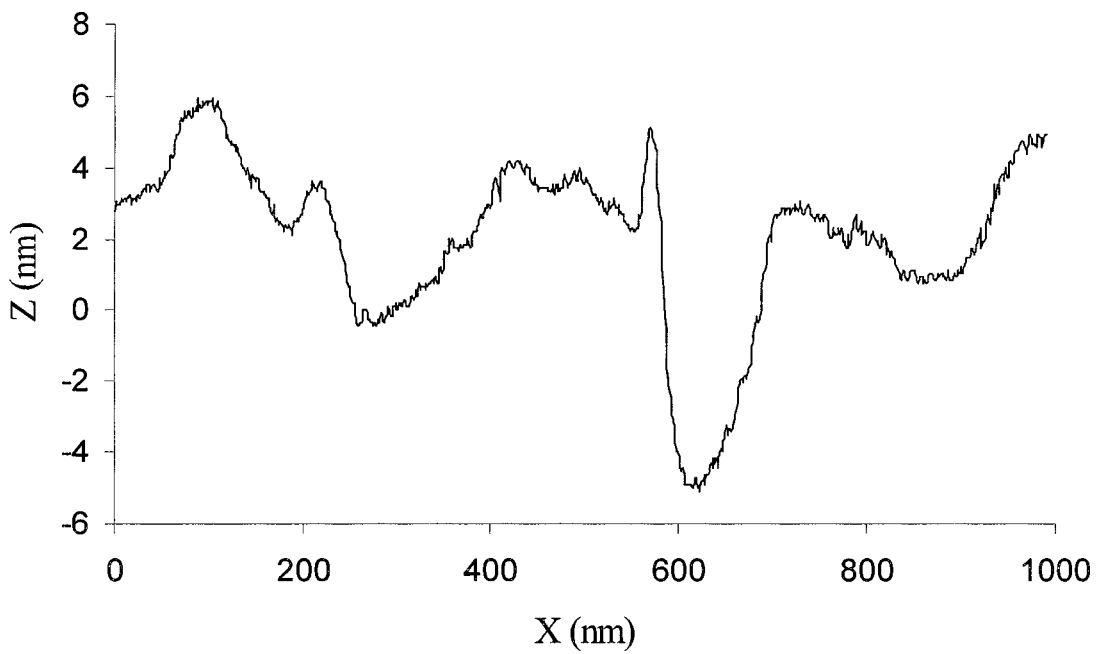
29. 3-D AFM Surface Image of Nylon-MXD6 at 5 % Clay Loading at Time Zero.



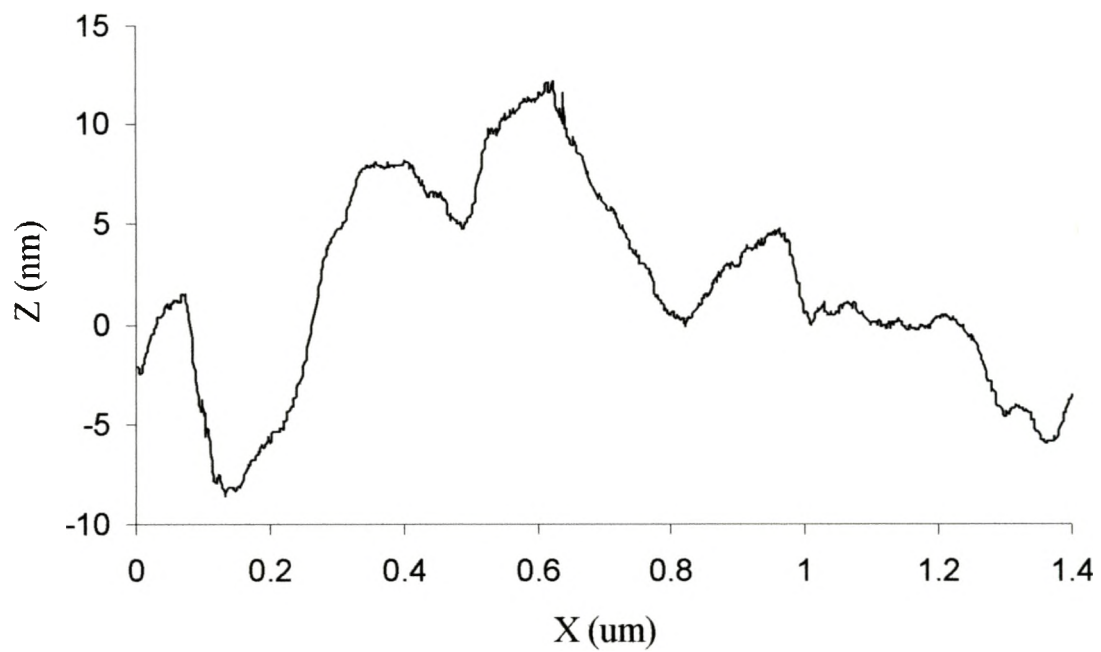
30. 2-D AFM Surface Image of Nylon-MXD6 at 5 % Clay Loading at Time Zero, green and blue lines represent topographical surface measurement.



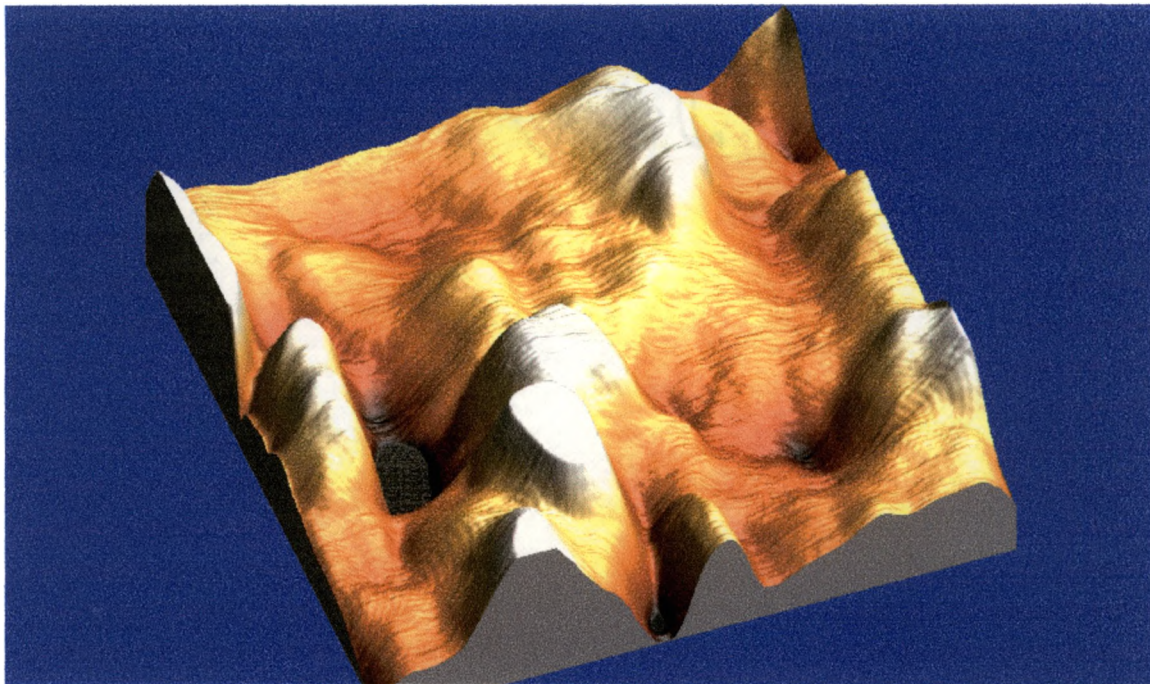
31. Topographical analysis of Nylon-MXD6 at 5 % Clay Loading at Time Zero, the graph represents the green line of 30.



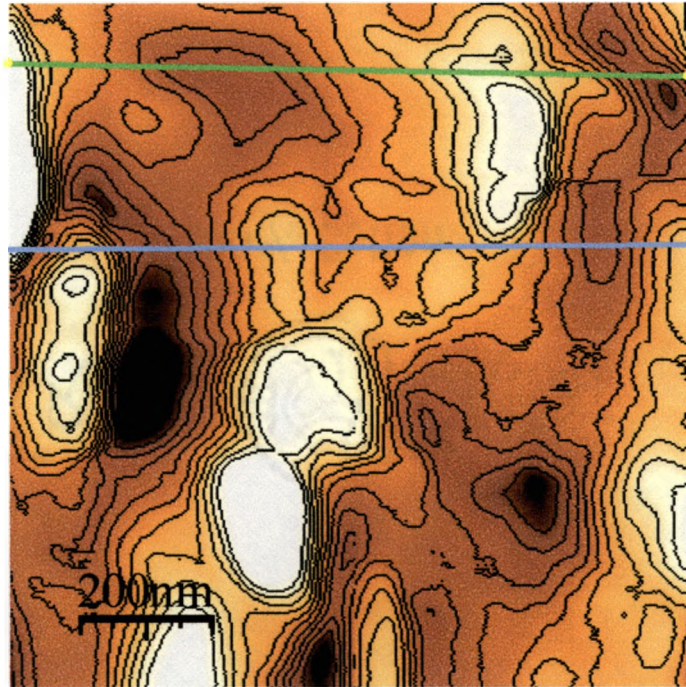
32. Topographical analysis of Nylon-MXD6 at 5 % Clay Loading at Time Zero, the graph represents the blue line of 30.



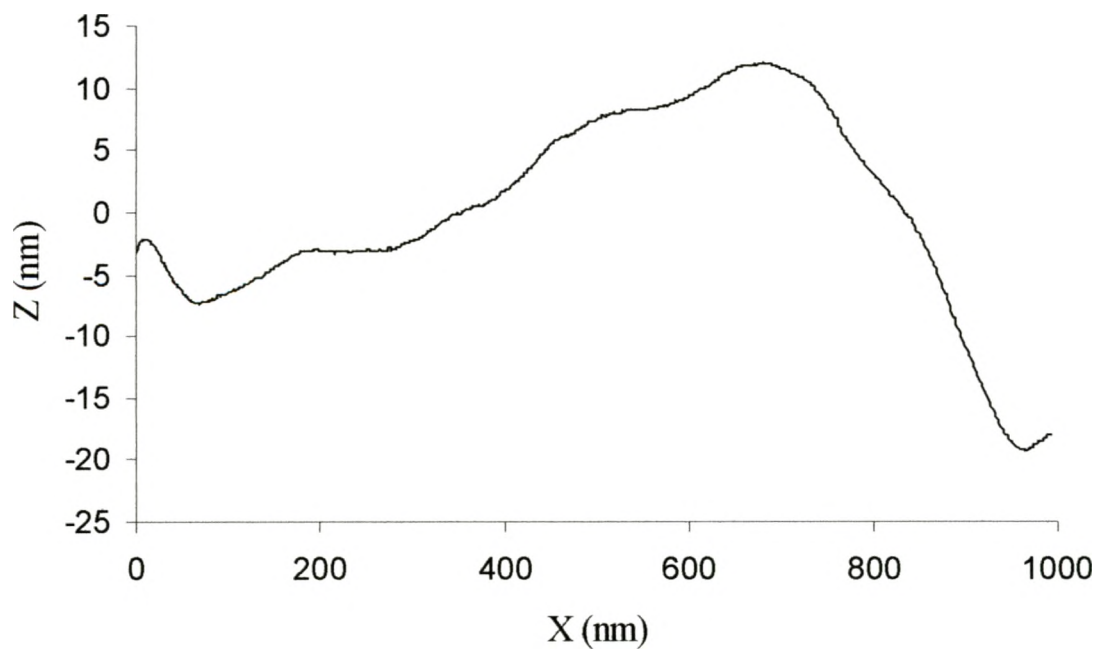
33. Topographical analysis of Nylon-MXD6 at 5 % Clay Loading at Time Zero, the graph represents a cross section from 30.



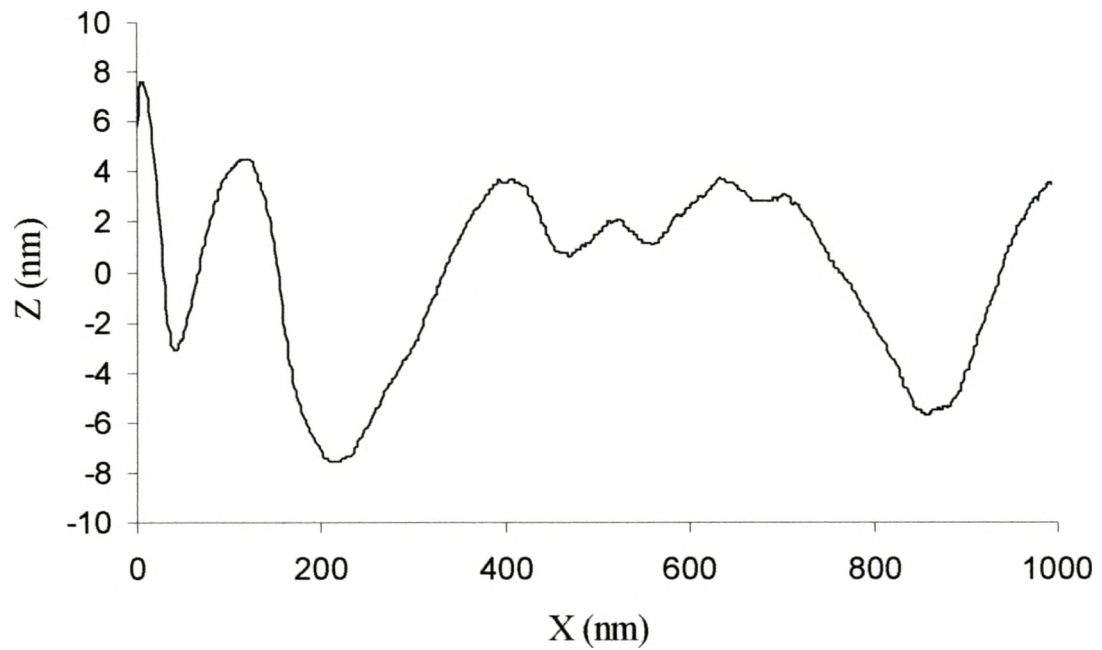
34. 3-D AFM Surface Image of Nylon-MXD6 at 5 % Clay Loading at Time 1 Hour.



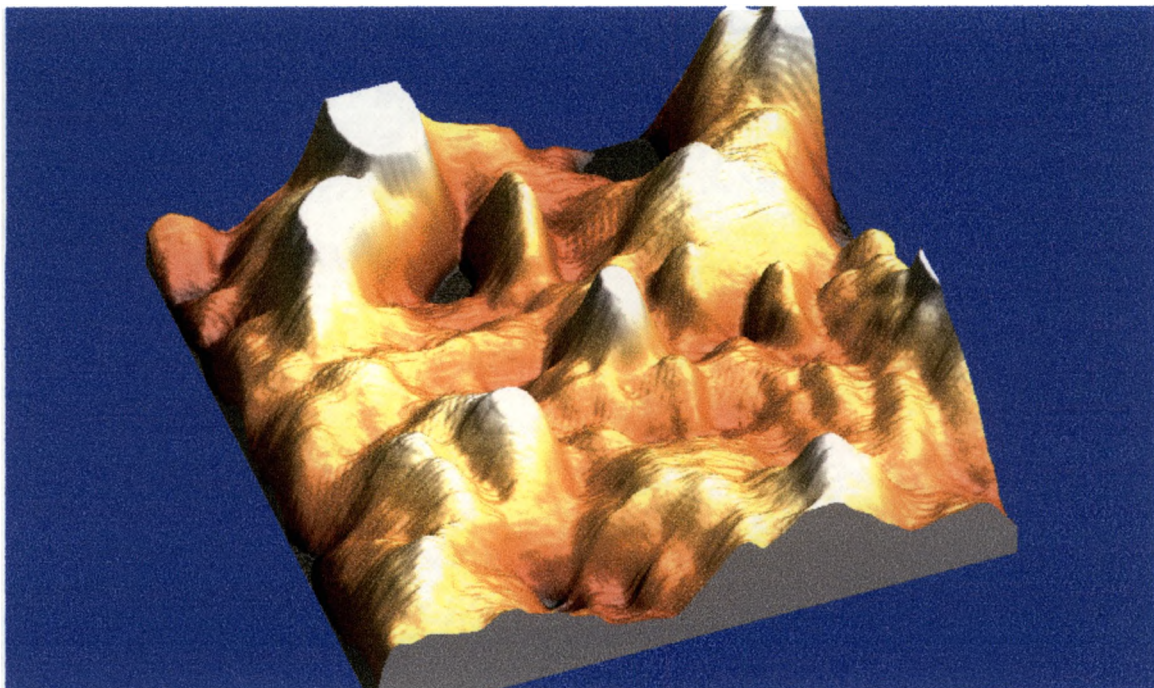
35. 2-D AFM Surface Image of Nylon-MXD6 at 5 % Clay Loading at Time 1 Hour, green and blue lines represent topographical surface measurement.



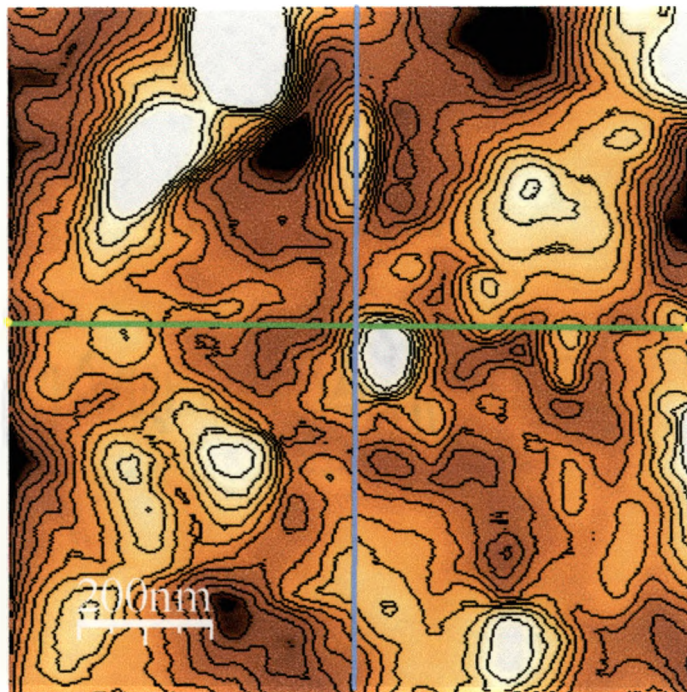
36. Topographical analysis of Nylon-MXD6 at 5 % Clay Loading at Time 1 Hour, the graph represents the green line of 35.



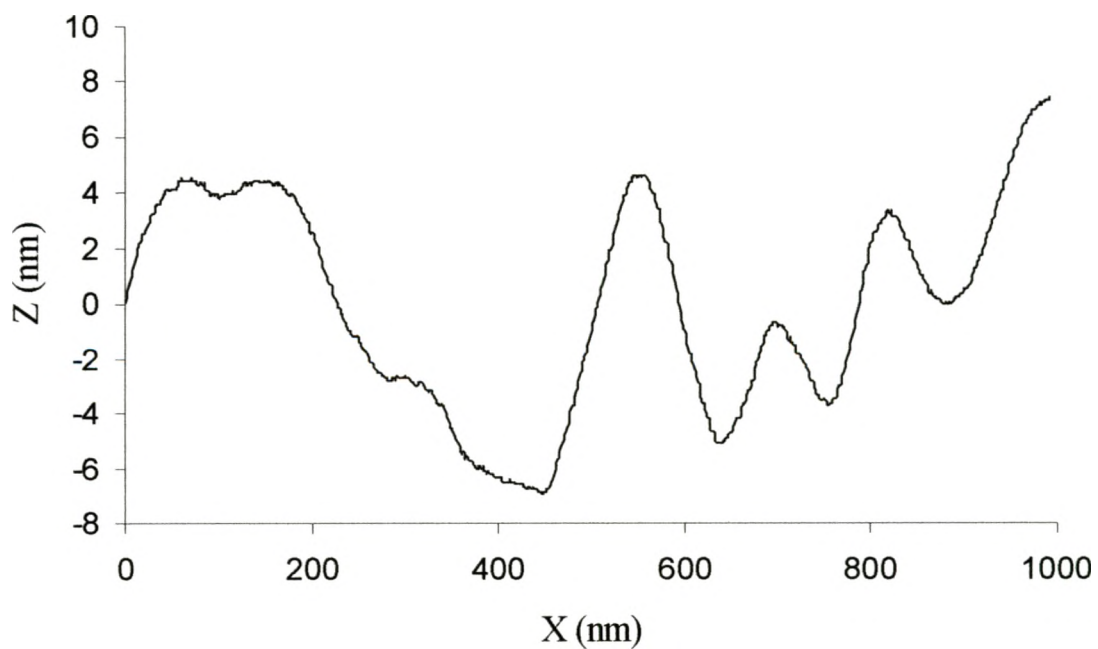
37. Topographical analysis of Nylon-MXD6 at 5 % Clay Loading at Time 1 Hour, the graph represents the blue line of 35.



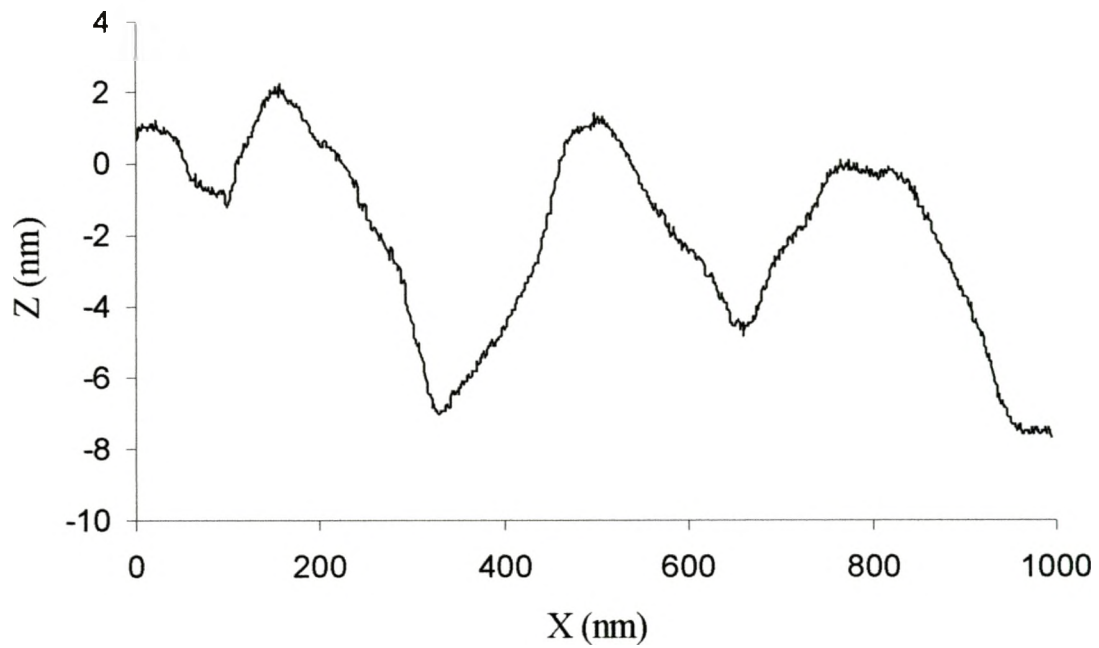
38. 3-D AFM Surface Image of Nylon-MXD6 at 5 % Clay Loading at Time 2 Hours.



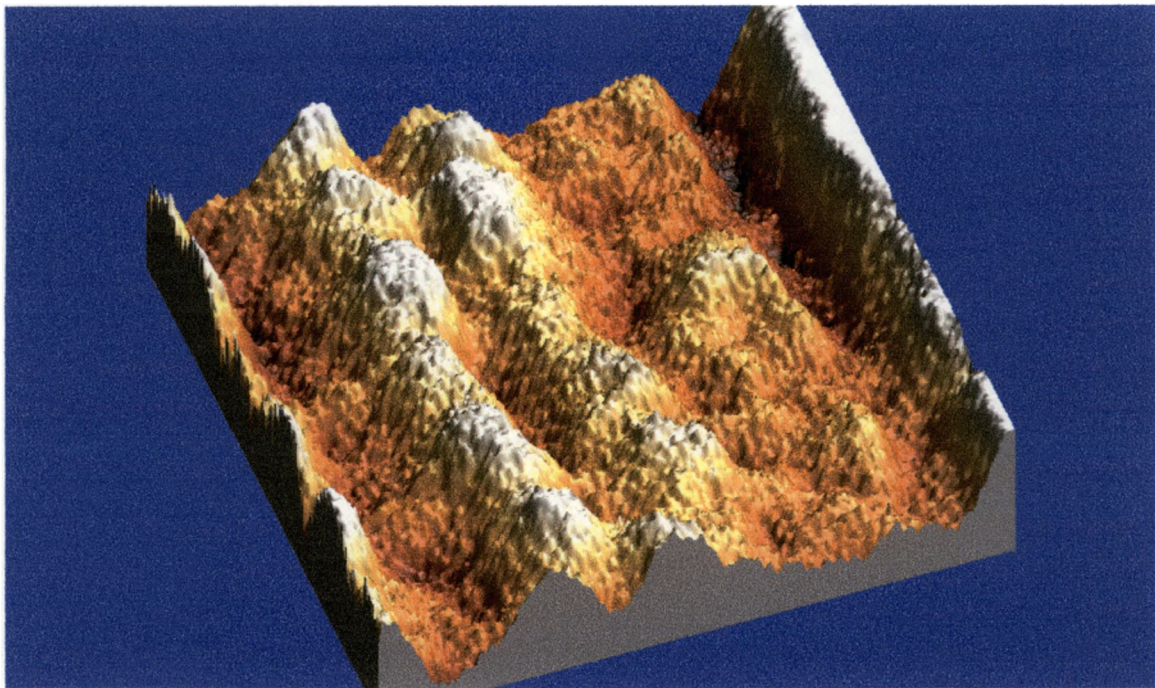
39. 2-D AFM Surface Image of Nylon-MXD6 at 5 % Clay Loading at Time 2 Hours, green and blue lines represent topographical surface measurement.



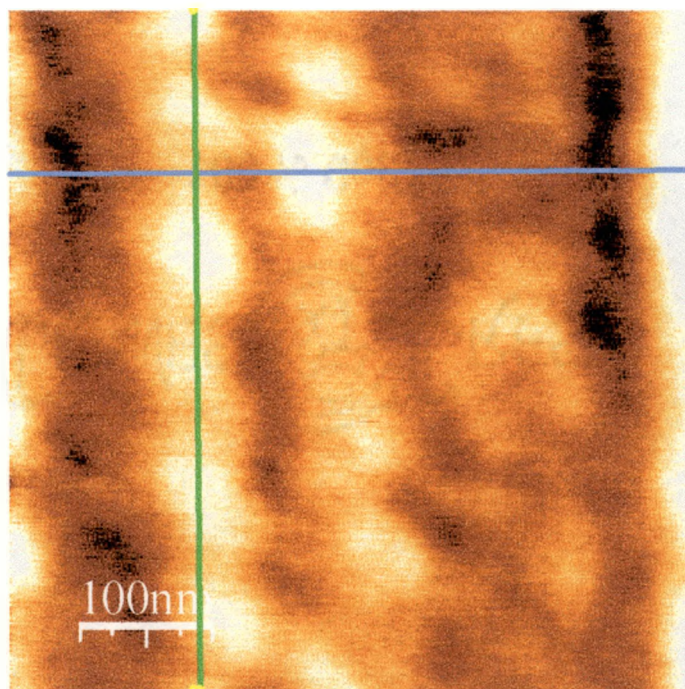
40. Topographical analysis of Nylon-MXD6 at 5 % Clay Loading at Time 2 Hours, the graph represents the green line of 39.



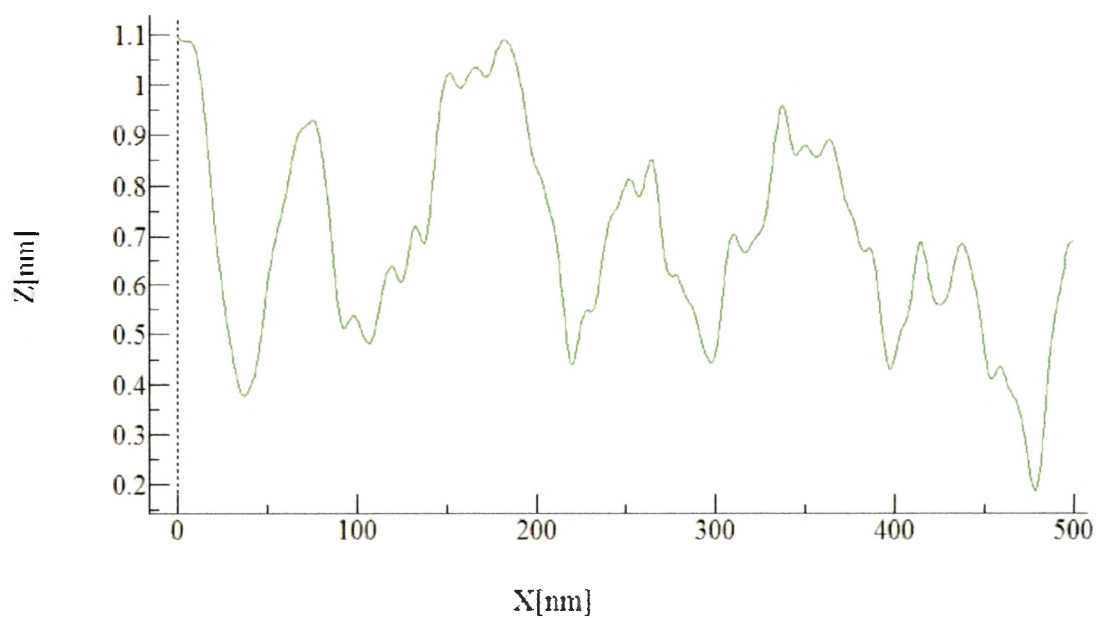
41. Topographical analysis of Nylon-MXD6 at 5 % Clay Loading at Time 2 Hours, the graph represents the green line of 39.



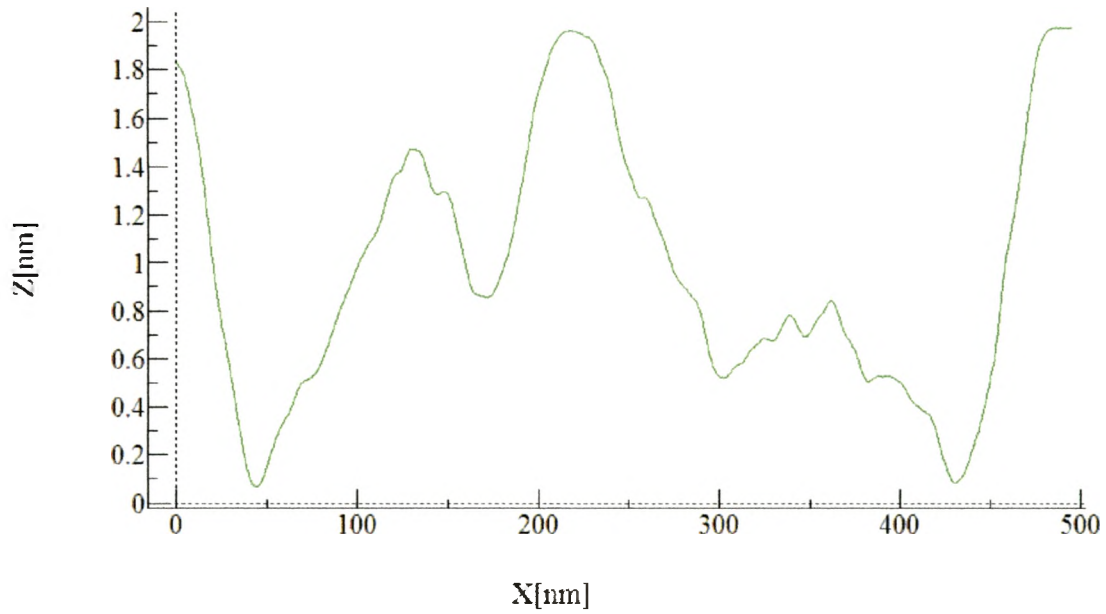
42. 3-D AFM Surface Image of Nylon 6 at 0.5 % Clay Loading at Time Zero.



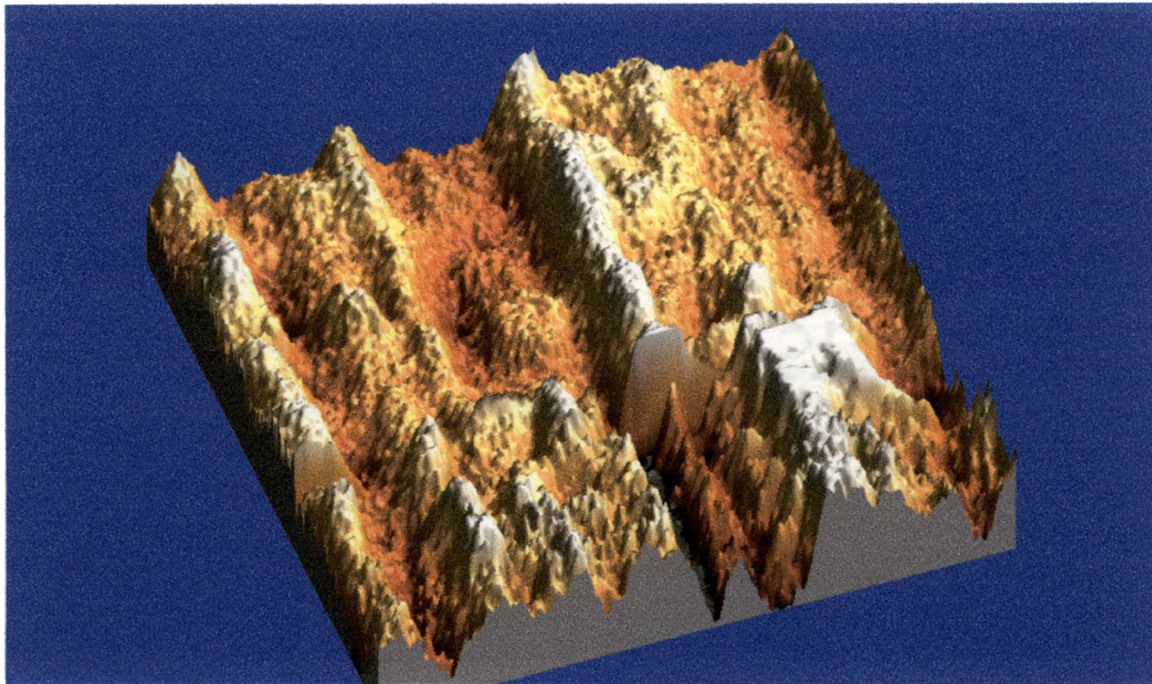
43. 2-D AFM Surface Image of Nylon 6 at 0.5 % Clay Loading at Time Zero, green and blue lines represent topographical surface measurement.



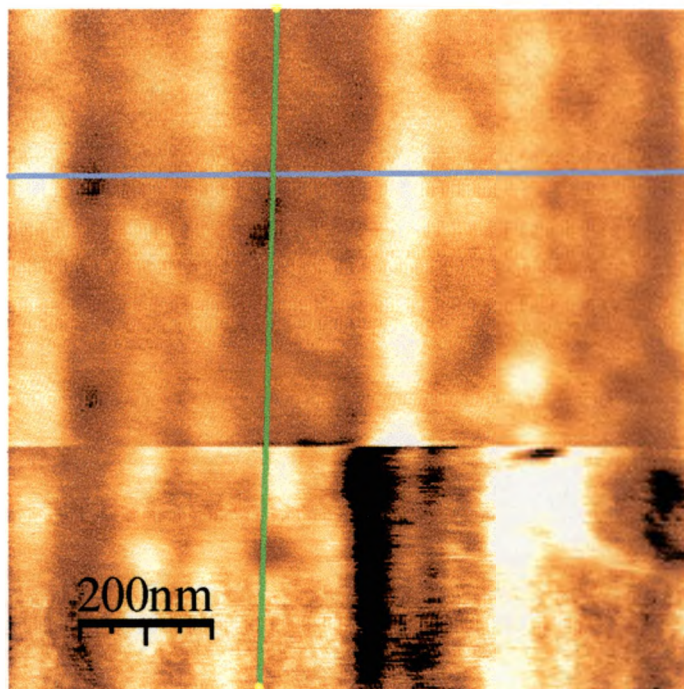
44. Topographical analysis of Nylon 6 at 0.5 % Clay Loading at Time Zero, the graph represents the green line of 43.



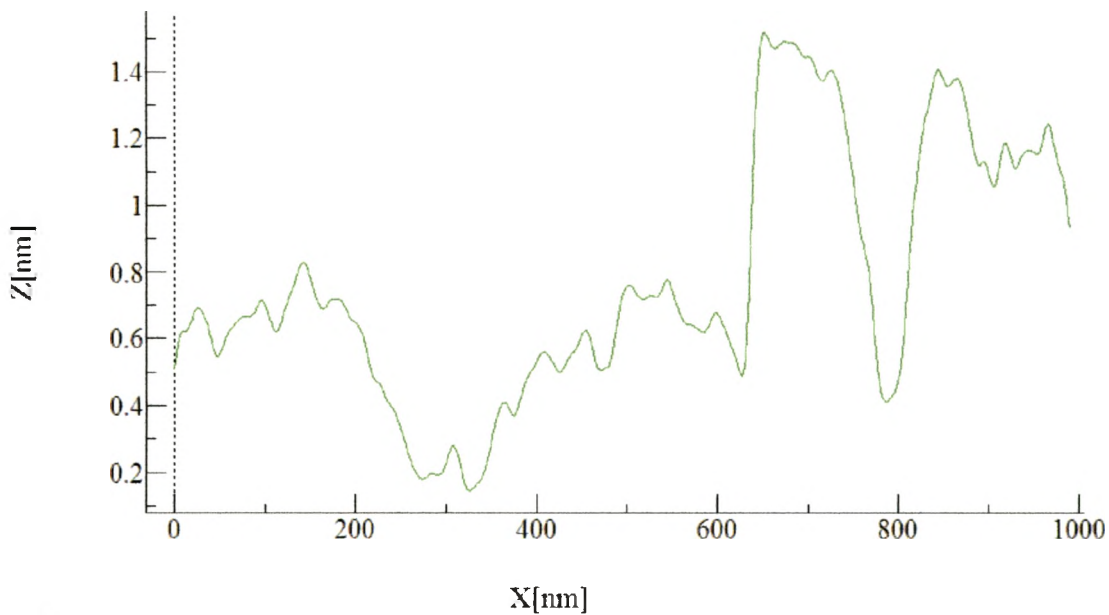
45. Topographical analysis of Nylon 6 at 0.5 % Clay Loading at Time Zero, the graph represents the blue line of 43.



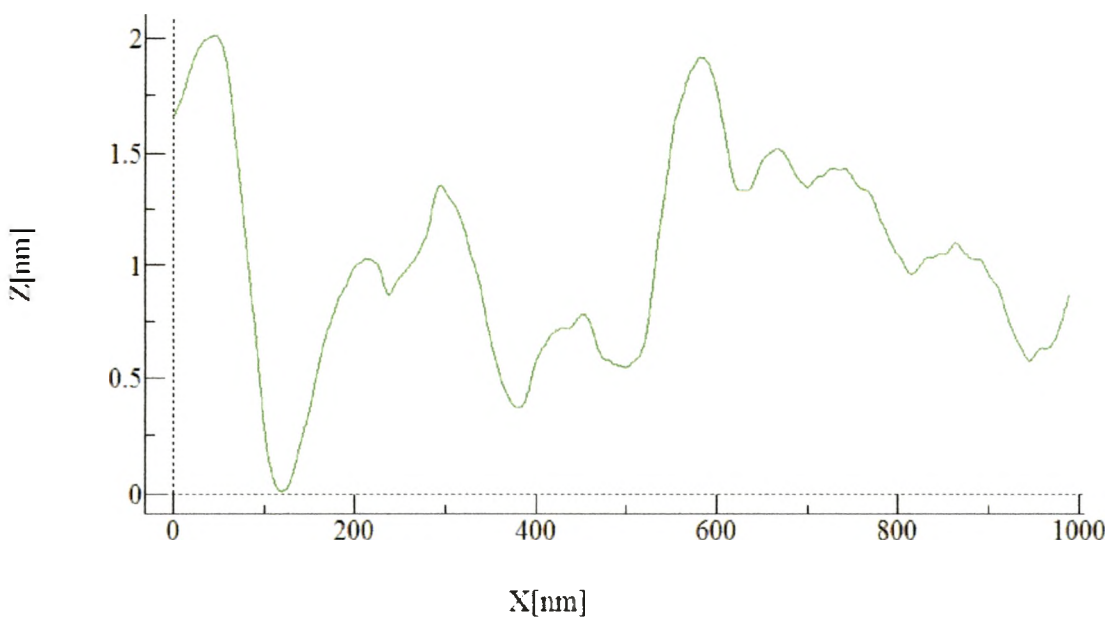
46. 3-D AFM Surface Image of Nylon 6 at 0.5 % Clay Loading at Time 30 Minutes.



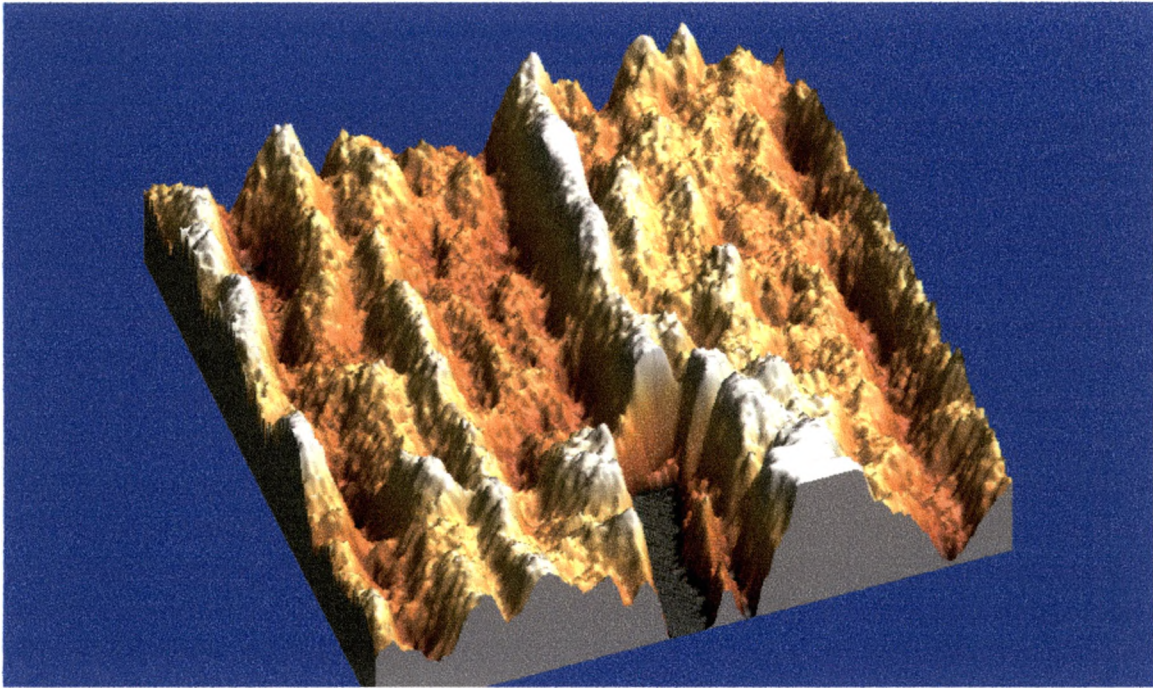
47. 2-D AFM Surface Image of Nylon 6 at 0.5 % Clay Loading at Time 30 Minutes, green and blue lines represent topographical surface measurement.



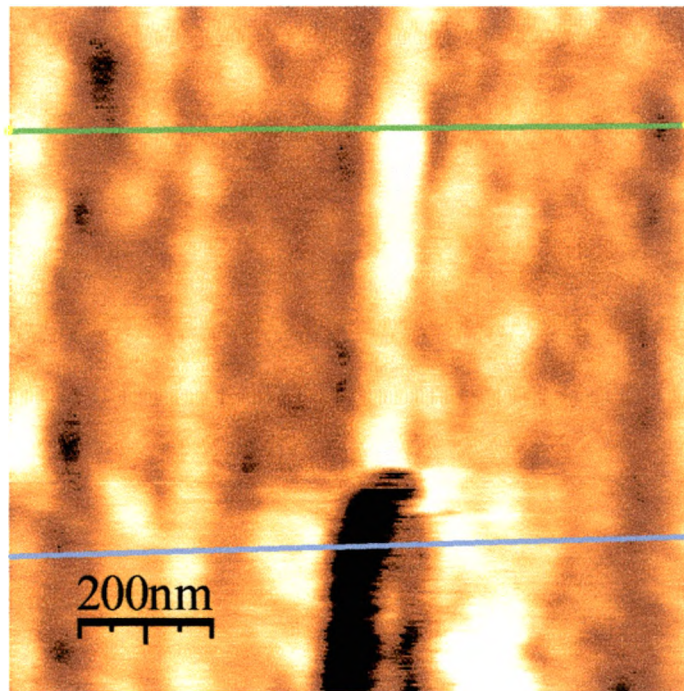
48. Topographical analysis of Nylon 6 at 0.5 % Clay Loading at Time 30 Minutes, the graph represents the green line of 47.



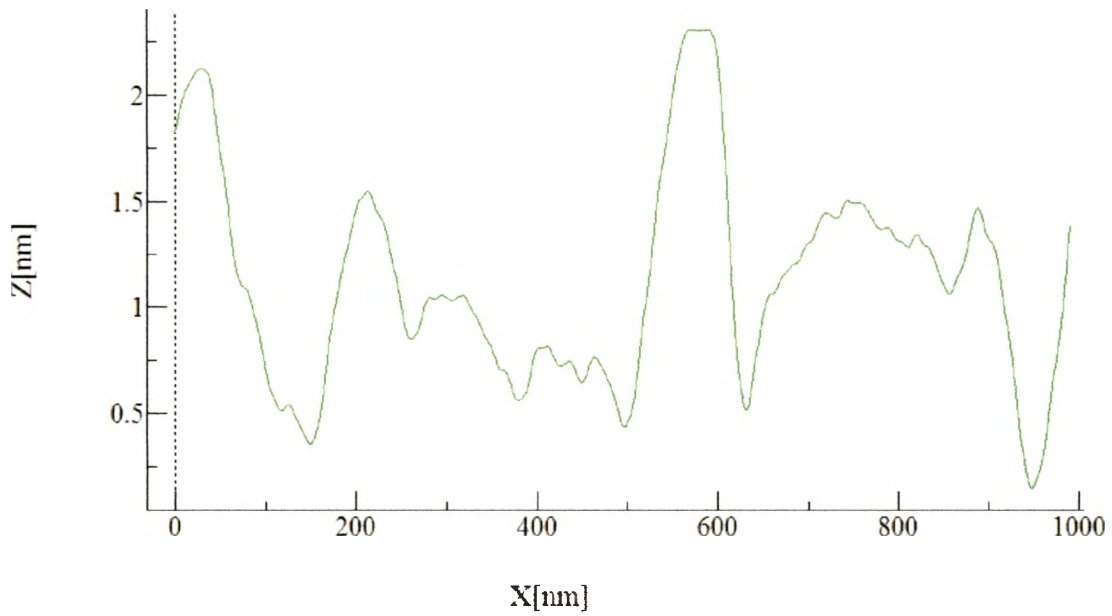
49. Topographical analysis of Nylon 6 at 0.5 % Clay Loading at Time 30 Minutes, the graph represents the blue line of 47.



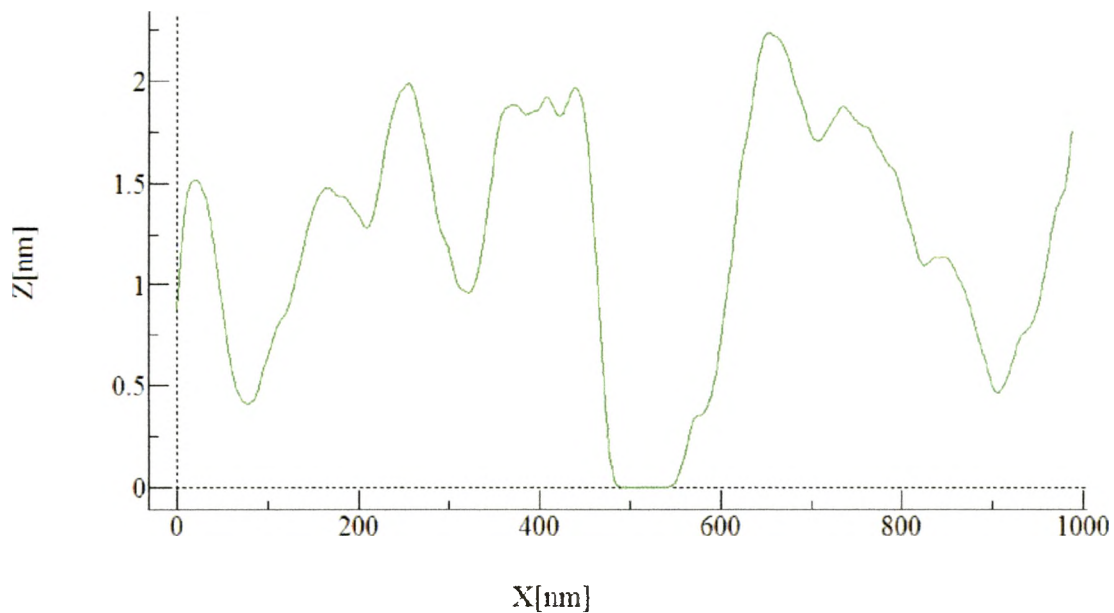
50. 3-D AFM Surface Image of Nylon 6 at 0.5 % Clay Loading at Time 1 Hour.



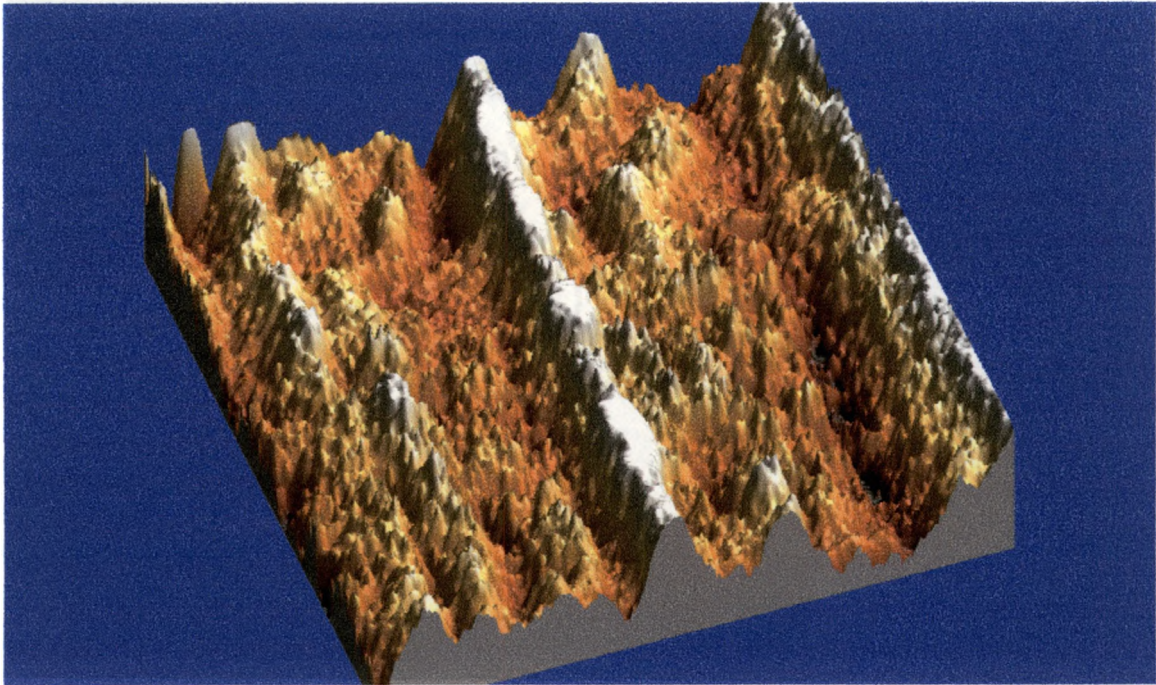
51. 2-D AFM Surface Image of Nylon 6 at 0.5 % Clay Loading at Time 1 Hour, green and blue lines represent topographical surface measurement.



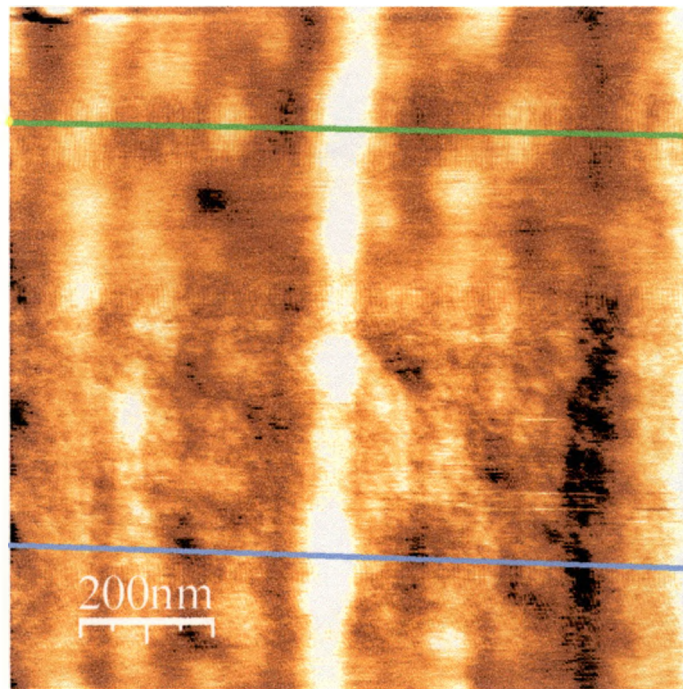
52. Topographical analysis of Nylon 6 at 0.5 % Clay Loading at Time 1 Hour, the graph represents the green line of 51.



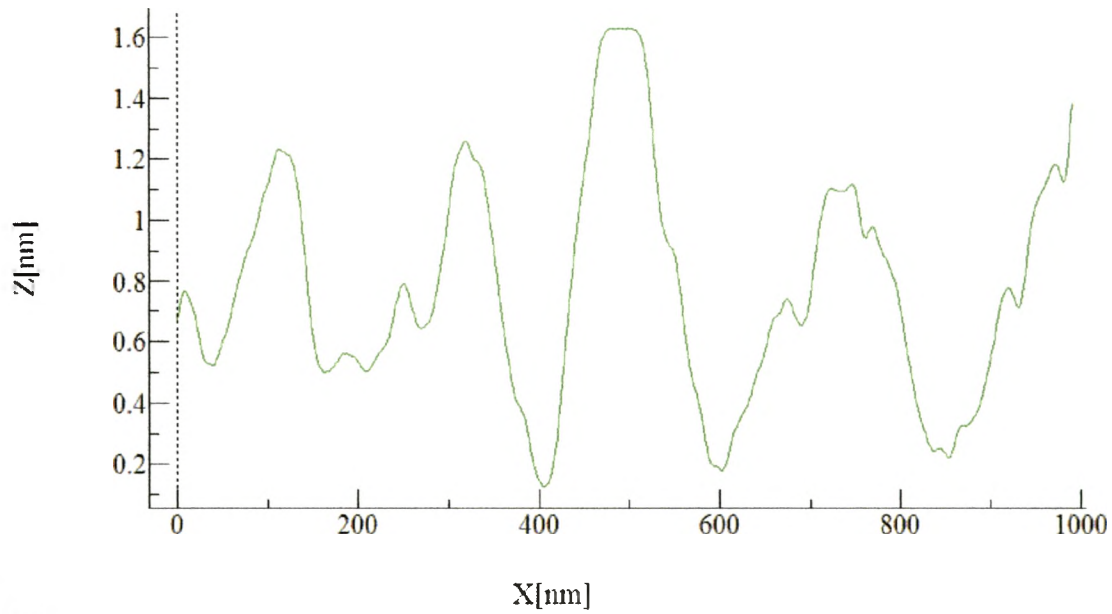
53. Topographical analysis of Nylon 6 at 0.5 % Clay Loading at Time 1 Hour, the graph represents the blue line of 51.



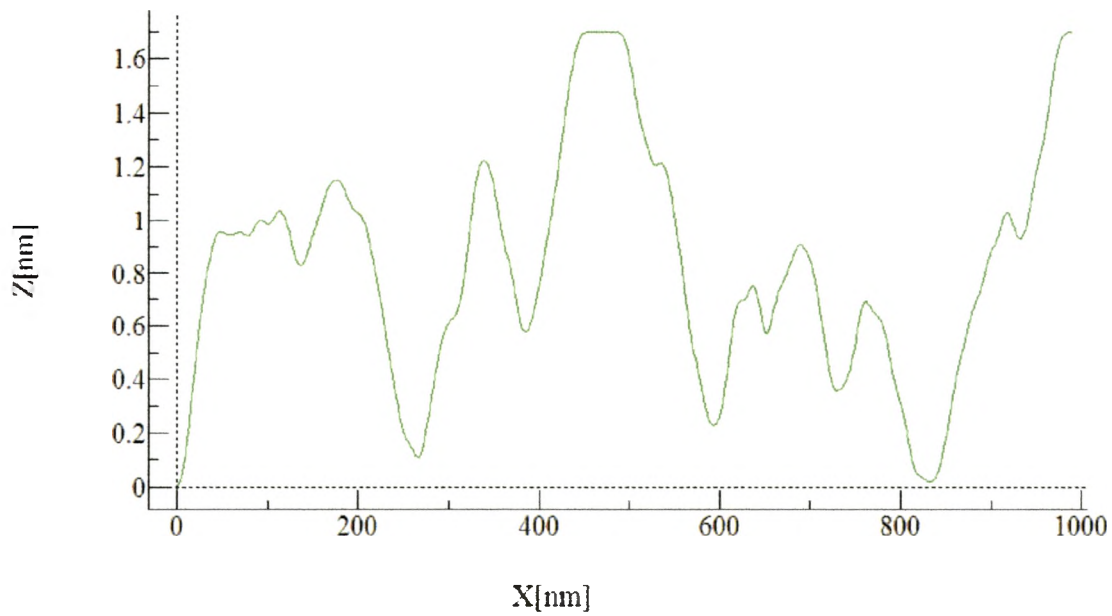
54. 3-D AFM Surface Image of Nylon 6 at 0.5 % Clay Loading at Time 2 Hours.



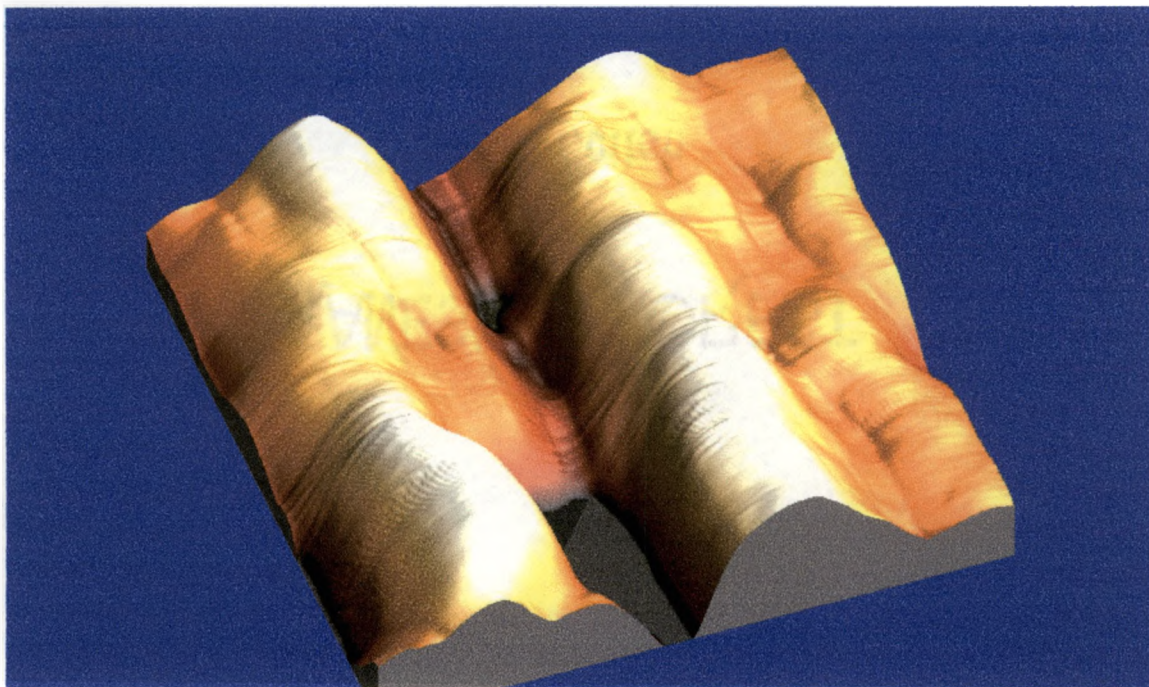
55. 2-D AFM Surface Image of Nylon 6 at 0.5 % Clay Loading at Time 2 Hours, green and blue lines represent topographical surface measurement.



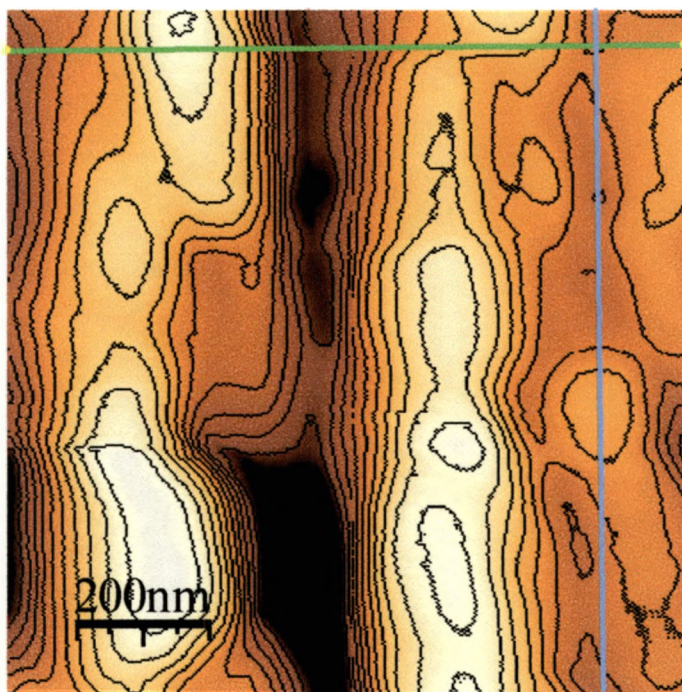
56. Topographical analysis of Nylon 6 at 0.5 % Clay Loading at Time 2 Hours, the graph represents the green line of 55.



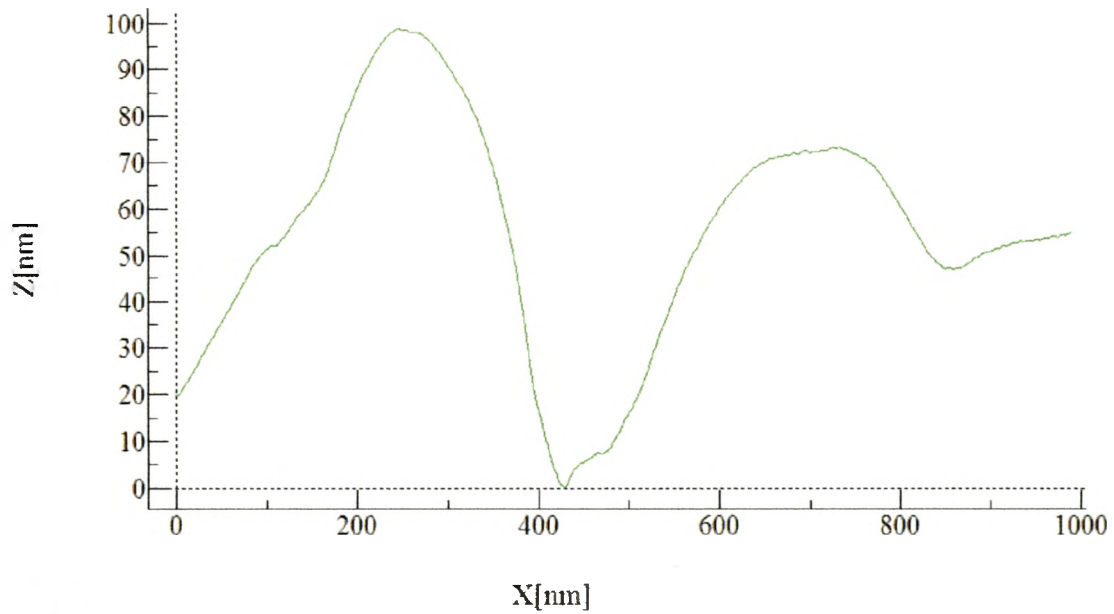
57. Topographical analysis of Nylon 6 at 0.5 % Clay Loading at Time 2 Hours, the graph represents the blue line of 55.



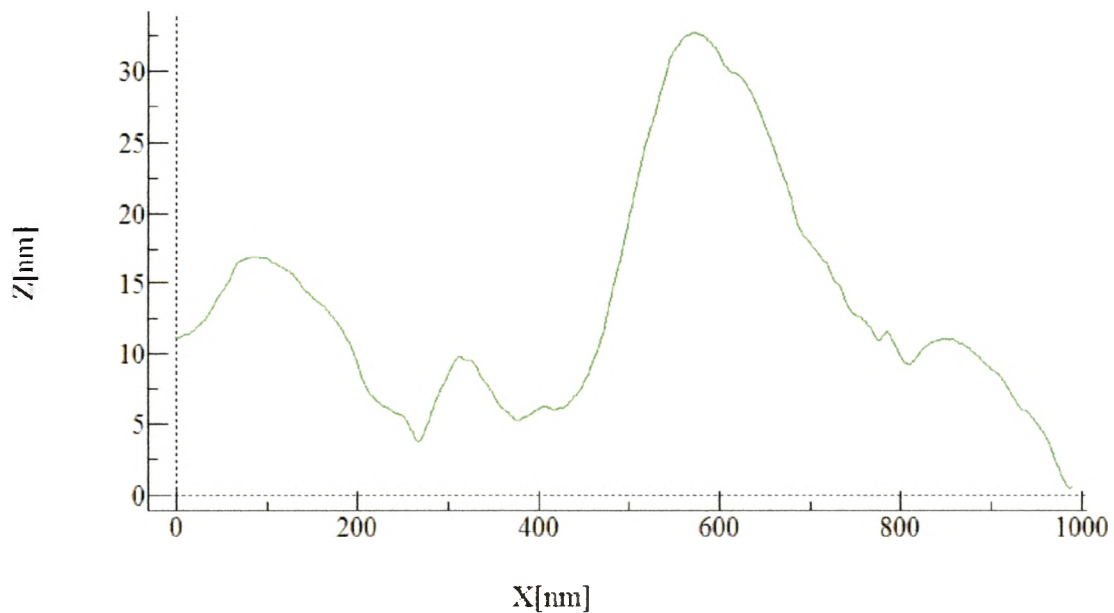
58. 3-D AFM Surface Image of Nylon 6 at 2 % Clay Loading at Time Zero.



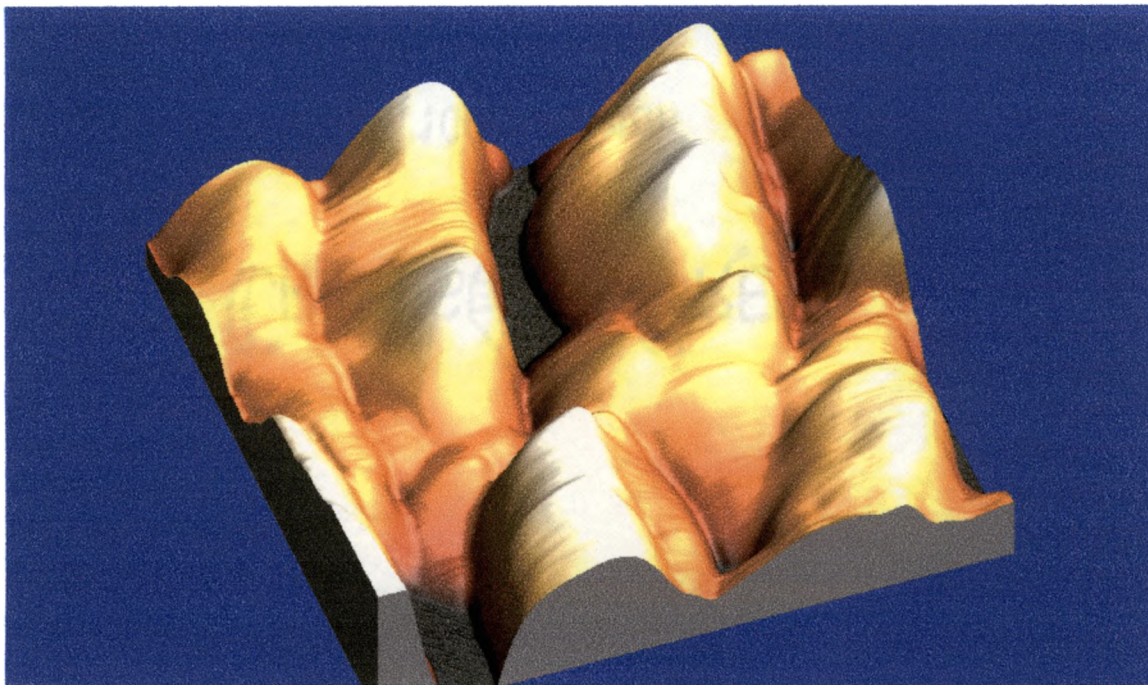
59. 2-D AFM Surface Image of Nylon 6 at 2 % Clay Loading at Time Zero, green and blue lines represent topographical surface measurement.



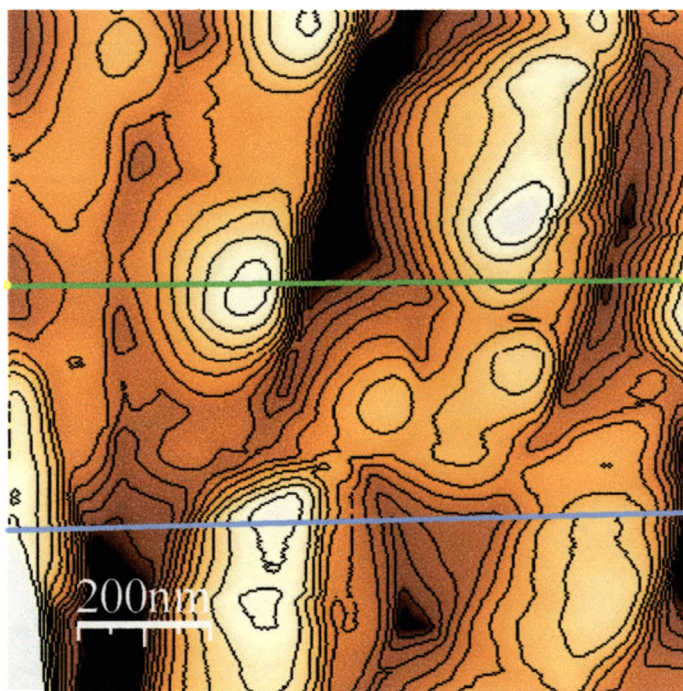
60. Topographical analysis of Nylon 6 at 2 % Clay Loading at Time Zero, the graph represents the green line of 59.



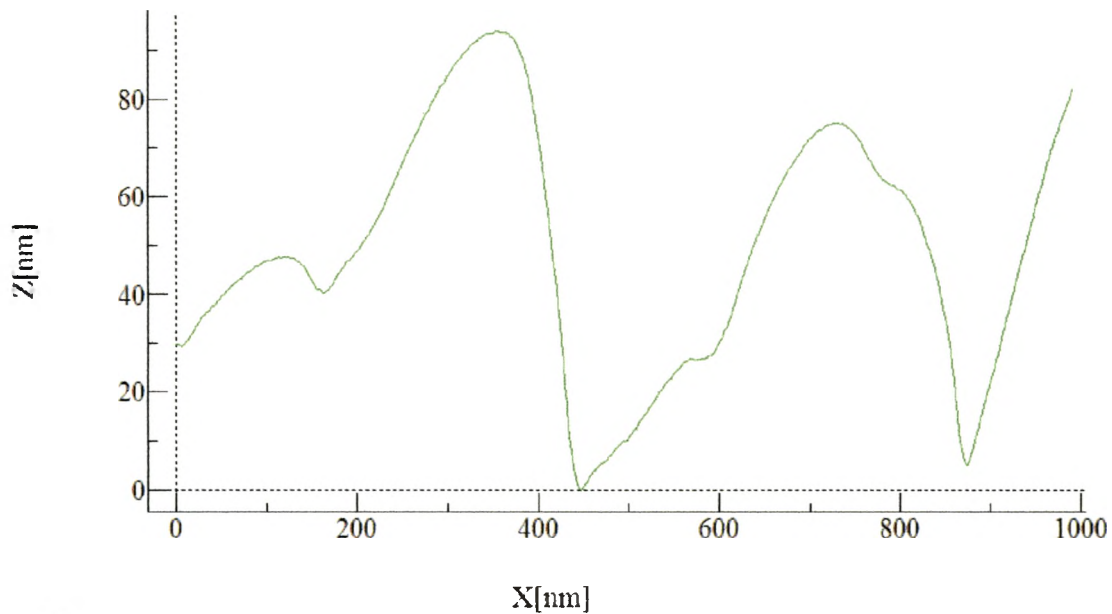
61. Topographical analysis of Nylon 6 at 2 % Clay Loading at Time Zero, the graph represents the blue line of 59.



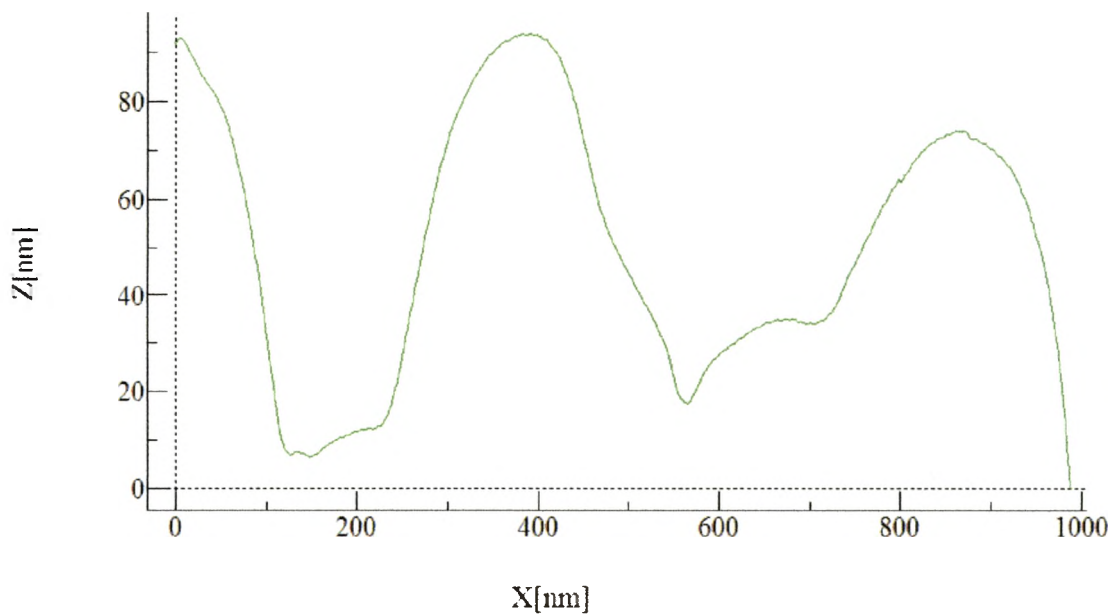
62. 3-D AFM Surface Image of Nylon 6 at 2 % Clay Loading at Time 30 Minutes.



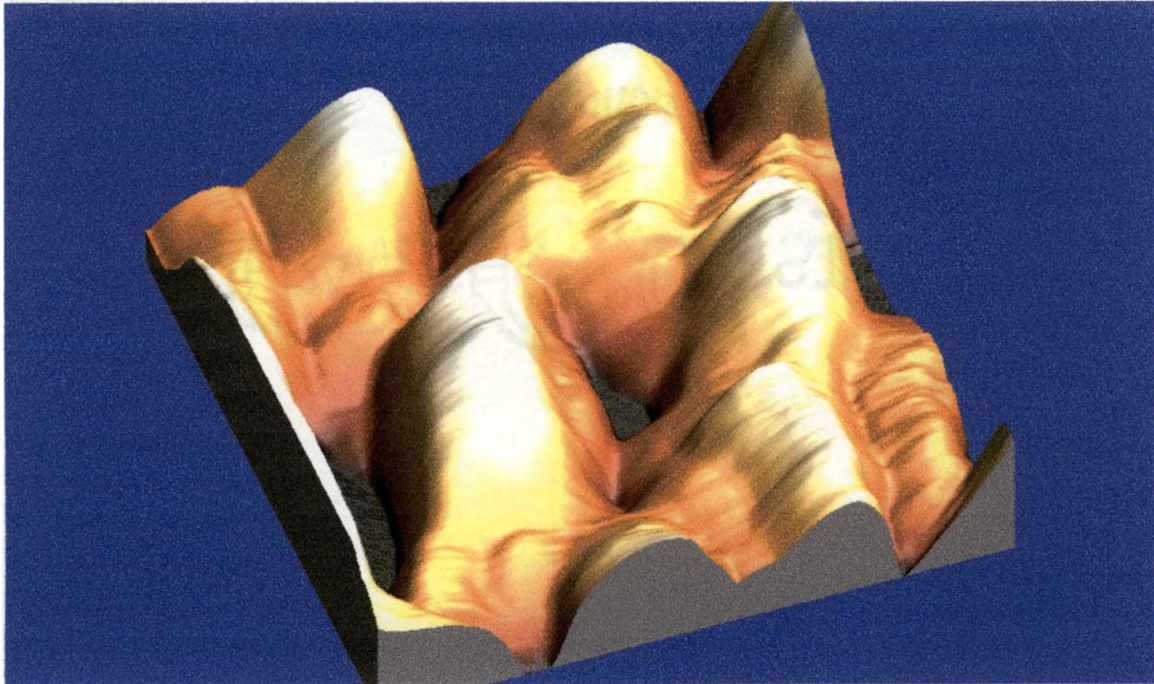
63. 2-D AFM Surface Image of Nylon 6 at 2 % Clay Loading at Time 30 Minutes, green and blue lines represent topographical surface measurement.



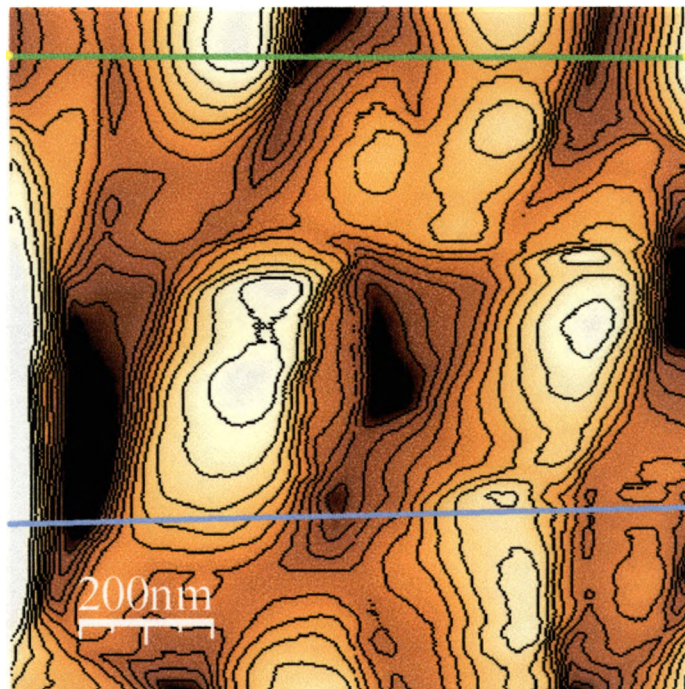
64. Topographical analysis of Nylon 6 at 2 % Clay Loading at Time 30 Minutes, the graph represents the green line of 63.



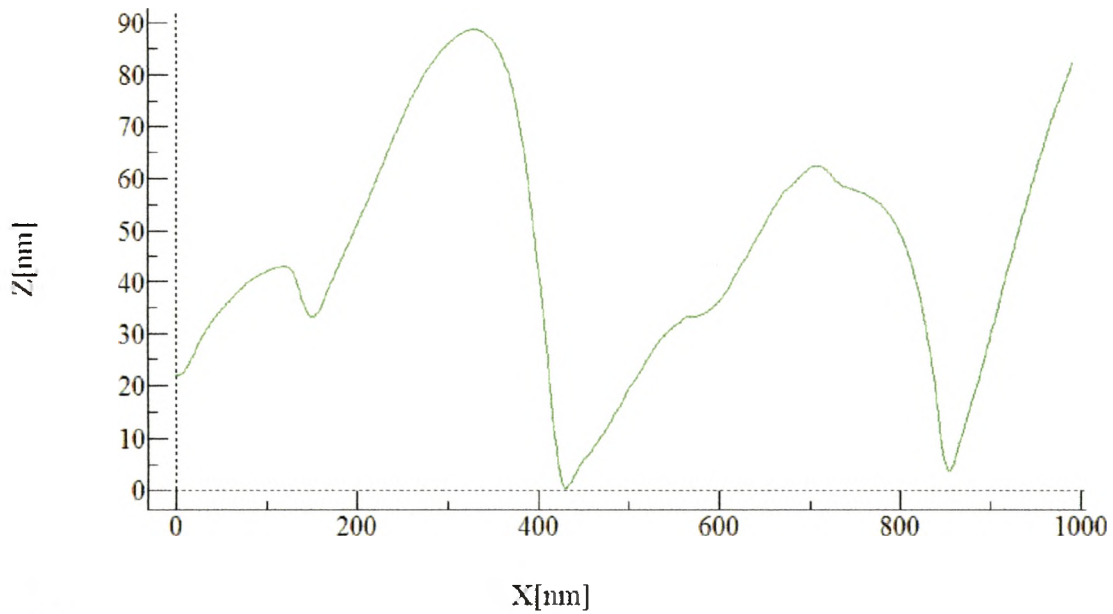
65. Topographical analysis of Nylon 6 at 2 % Clay Loading at Time 30 Minutes, the graph represents the blue line of 63.



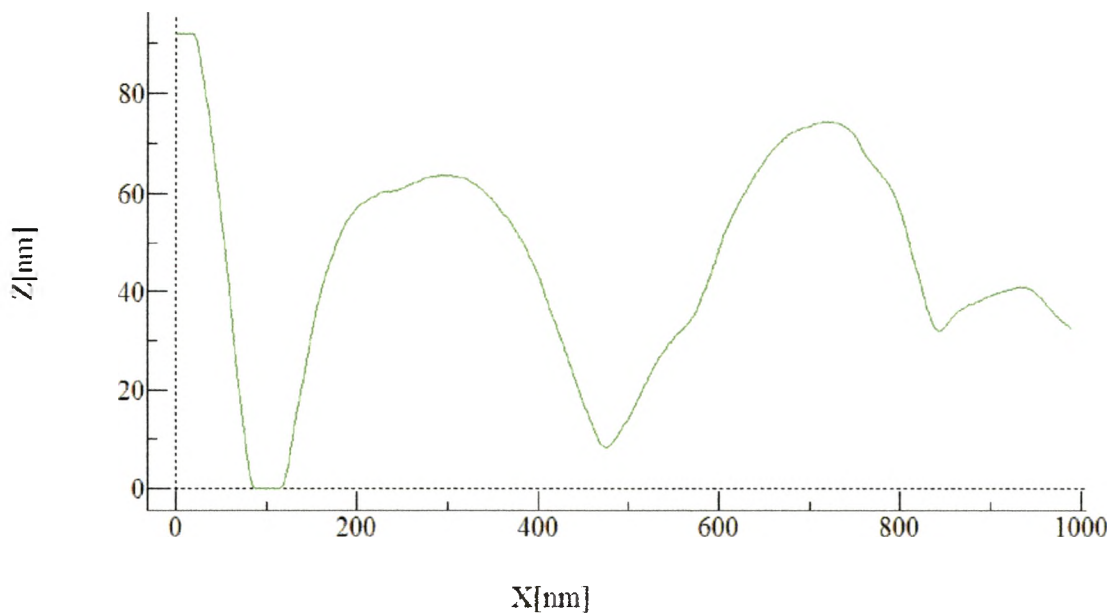
66. 3-D AFM Surface Image of Nylon 6 at 2 % Clay Loading at Time 1 Hour.



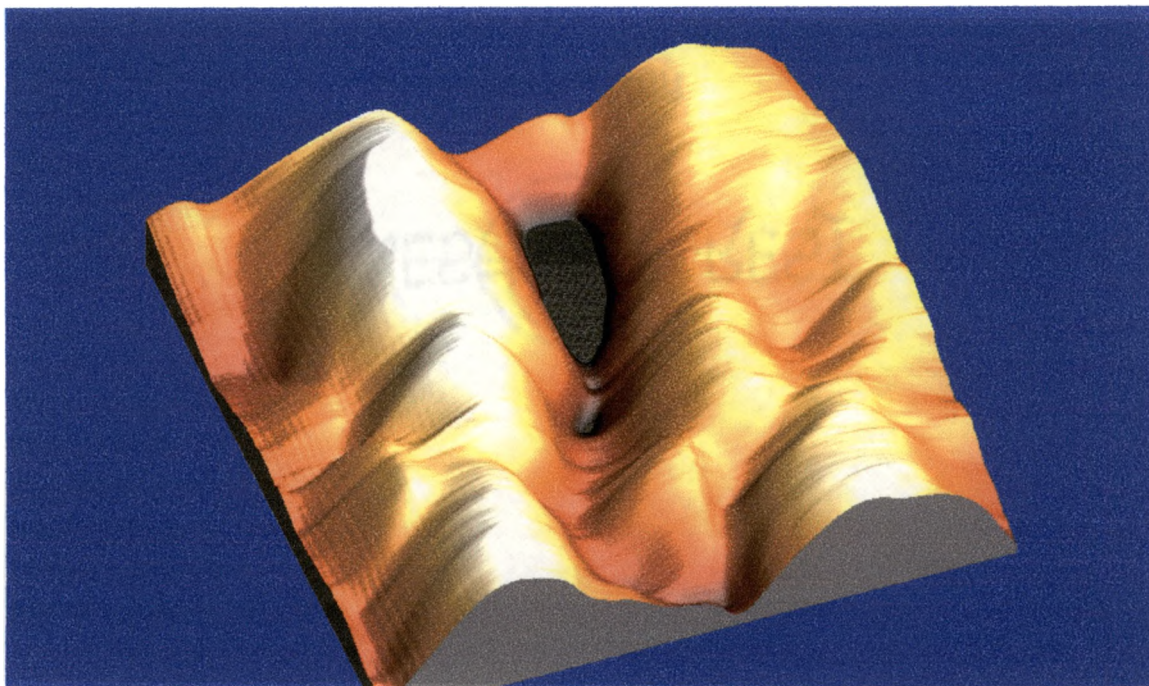
67. 2-D AFM Surface Image of Nylon 6 at 2 % Clay Loading at Time 1 Hour, green and blue lines represent topographical surface measurement.



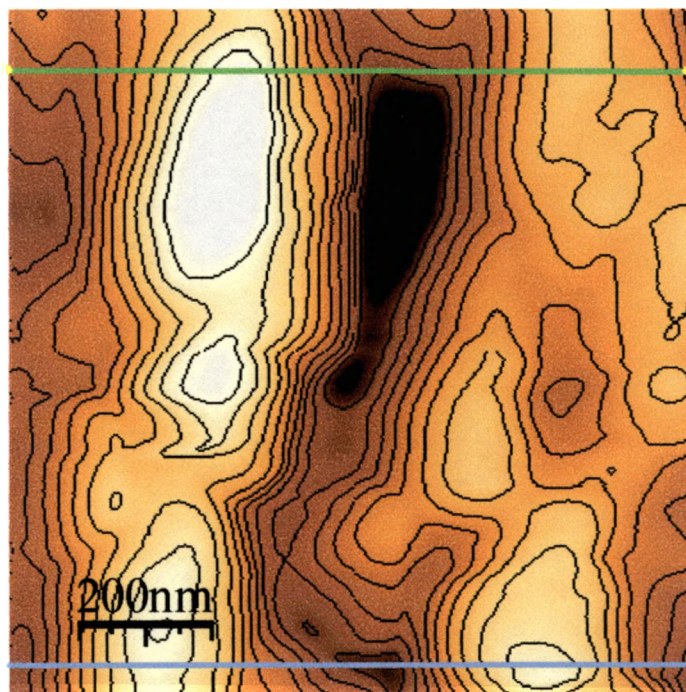
68. Topographical analysis of Nylon 6 at 2 % Clay Loading at Time 1 Hour, the graph represents the green line of 67.



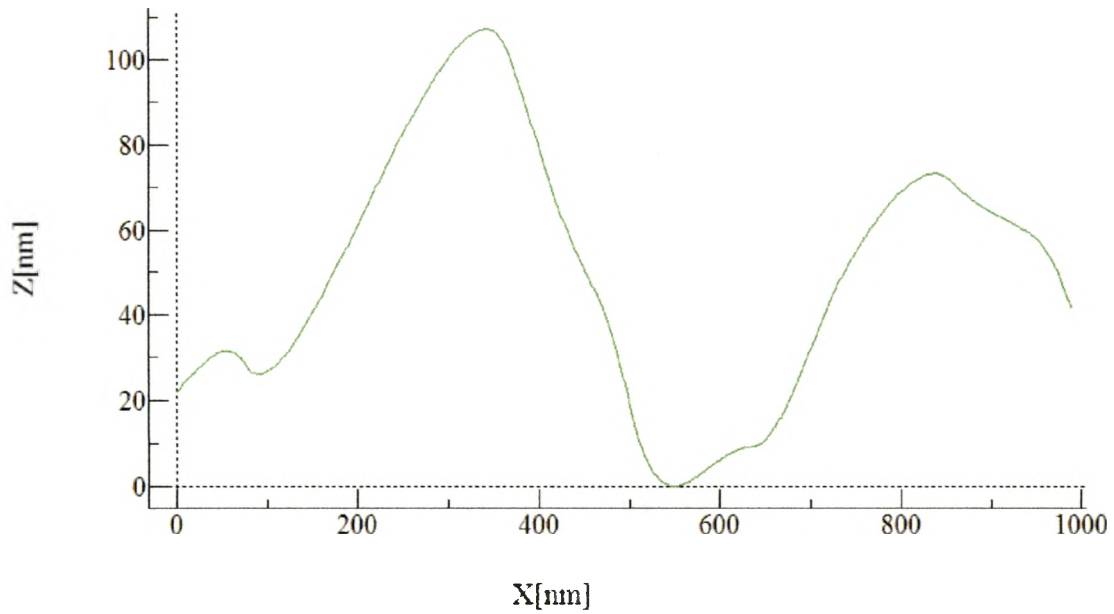
69. Topographical analysis of Nylon 6 at 2 % Clay Loading at Time 1 Hour, the graph represents the blue line of 67.



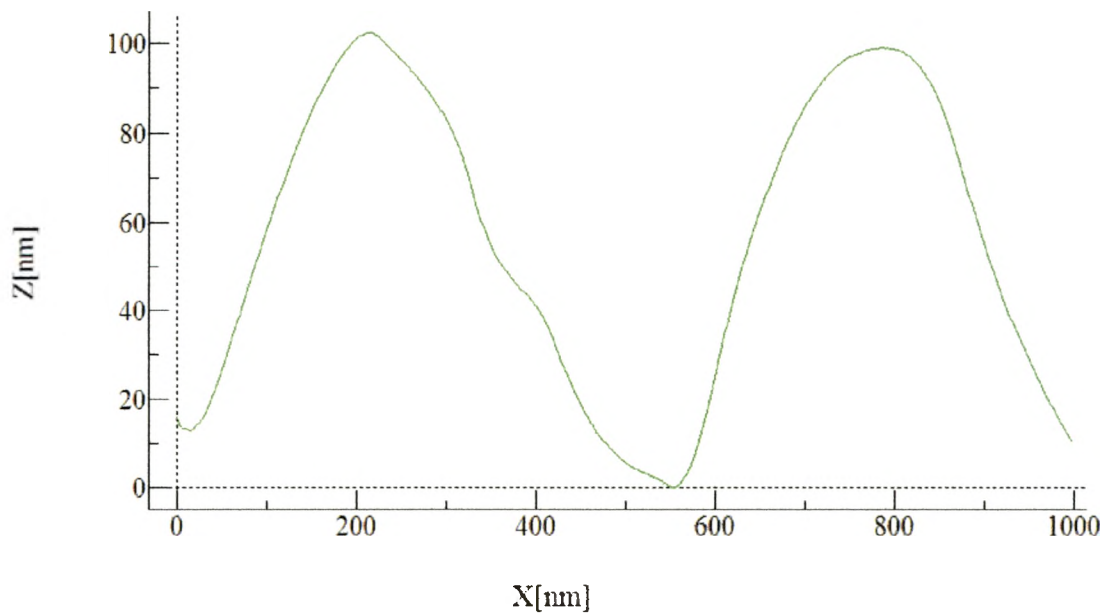
70. 3-D AFM Surface Image of Nylon 6 at 2 % Clay Loading at Time 2 Hours.



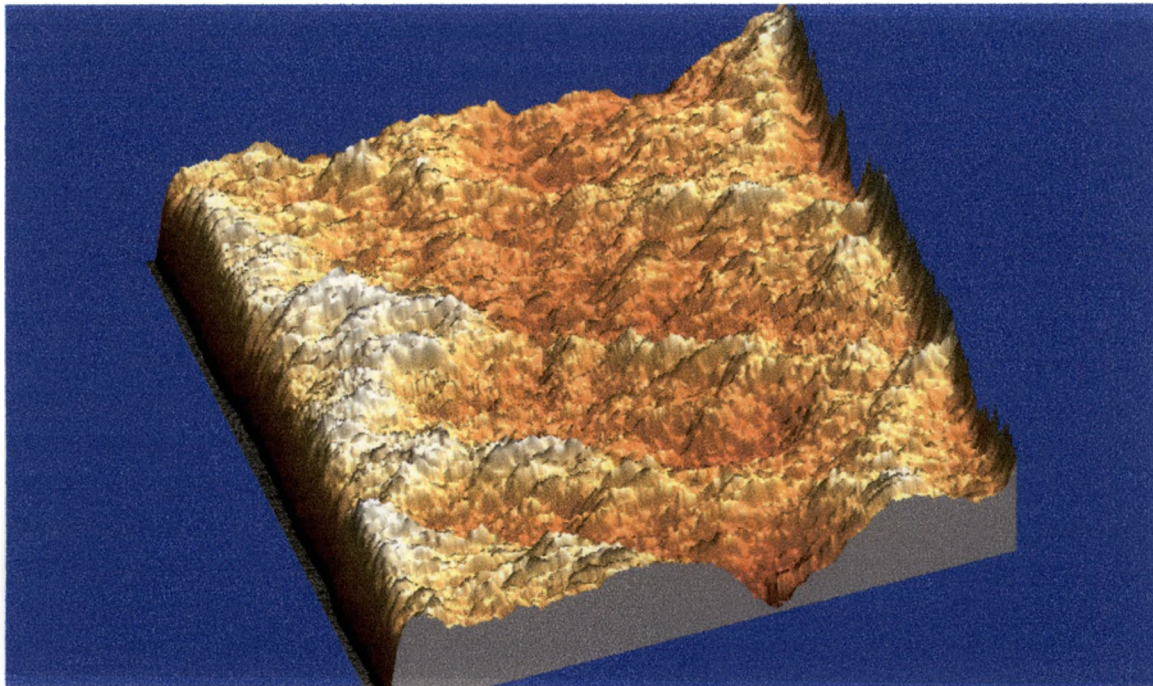
71. 2-D AFM Surface Image of Nylon 6 at 2 % Clay Loading at Time 2 Hours, green and blue lines represent topographical surface measurement.



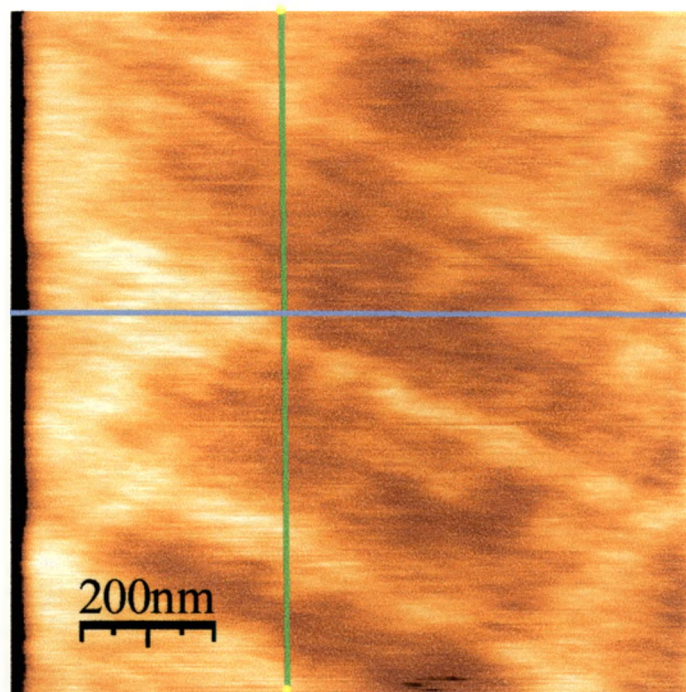
72. Topographical analysis of Nylon 6 at 2 % Clay Loading at Time 2 Hours, the graph represents the green line of 71.



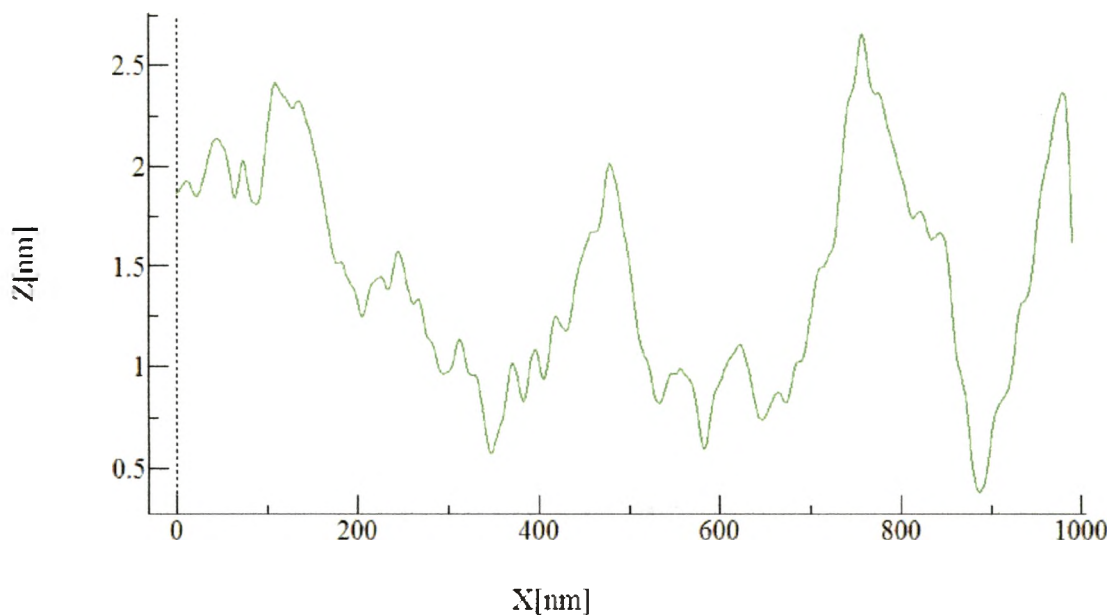
73. Topographical analysis of Nylon 6 at 2 % Clay Loading at Time 2 Hours, the graph represents the blue line of 71.



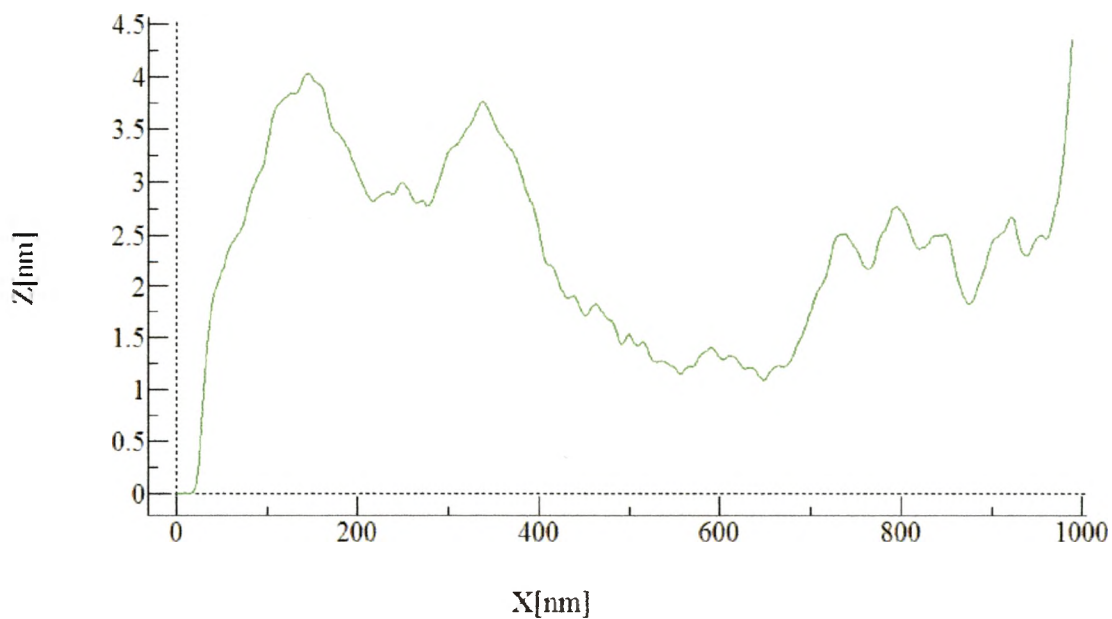
74. 3-D AFM Surface Image of Nylon 6 at 5 % Clay Loading at Time Zero.



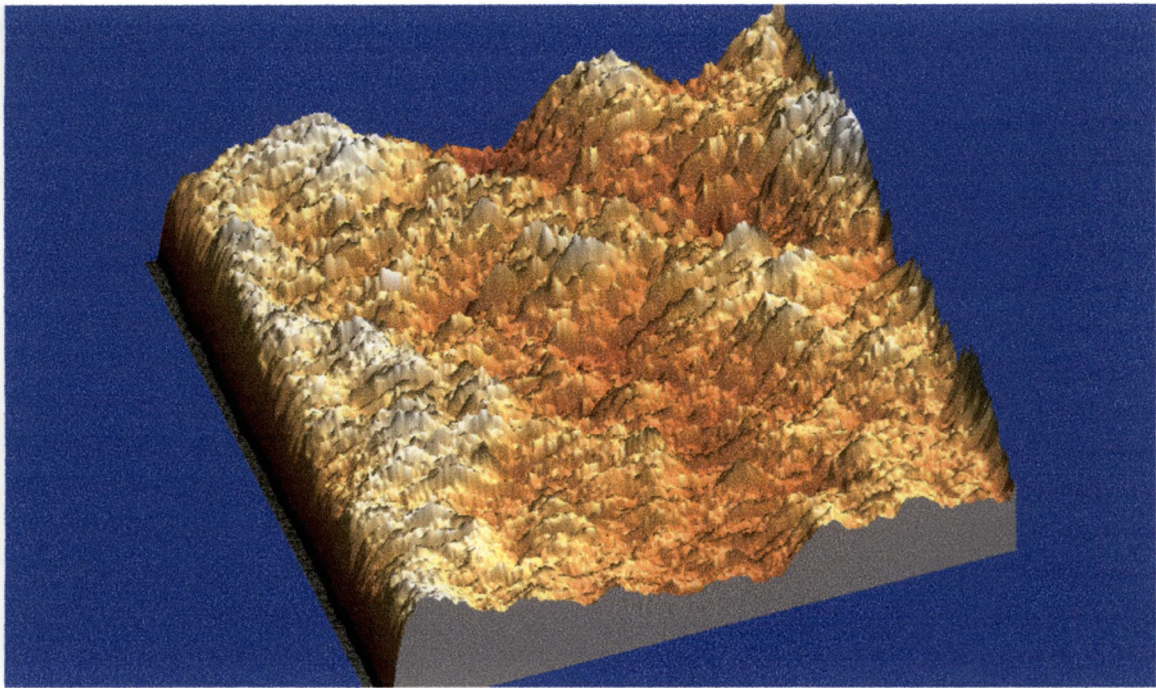
75. 2-D AFM Surface Image of Nylon 6 at 5 % Clay Loading at Time Zero, green and blue lines represent topographical surface measurement.



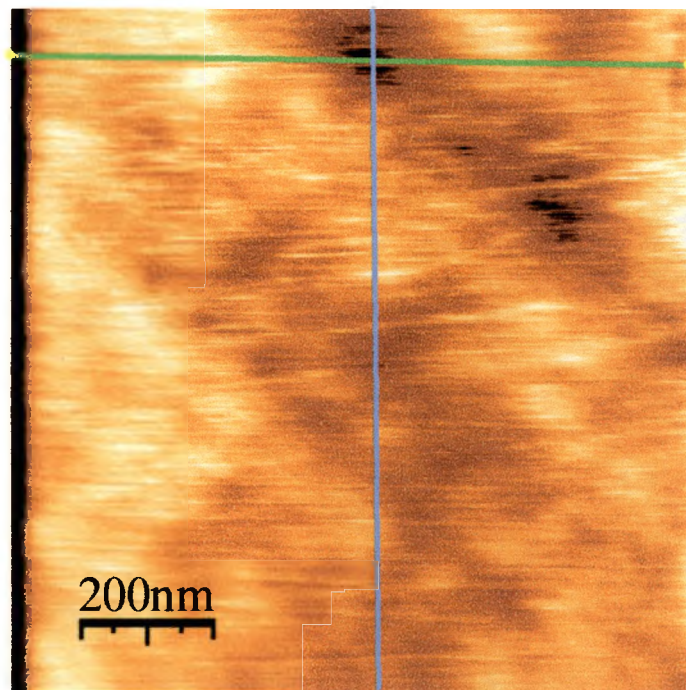
76. Topographical analysis of Nylon 6 at 5 % Clay Loading at Time Zero, the graph represents the green line of 75.



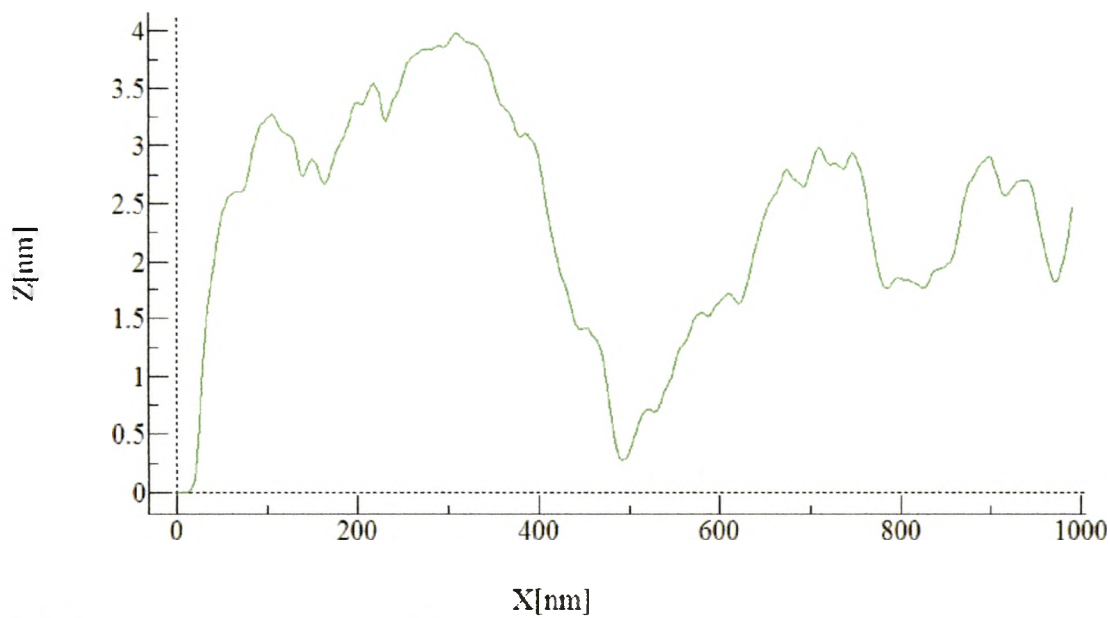
77. Topographical analysis of Nylon 6 at 5 % Clay Loading at Time Zero, the graph represents the blue line of 75.



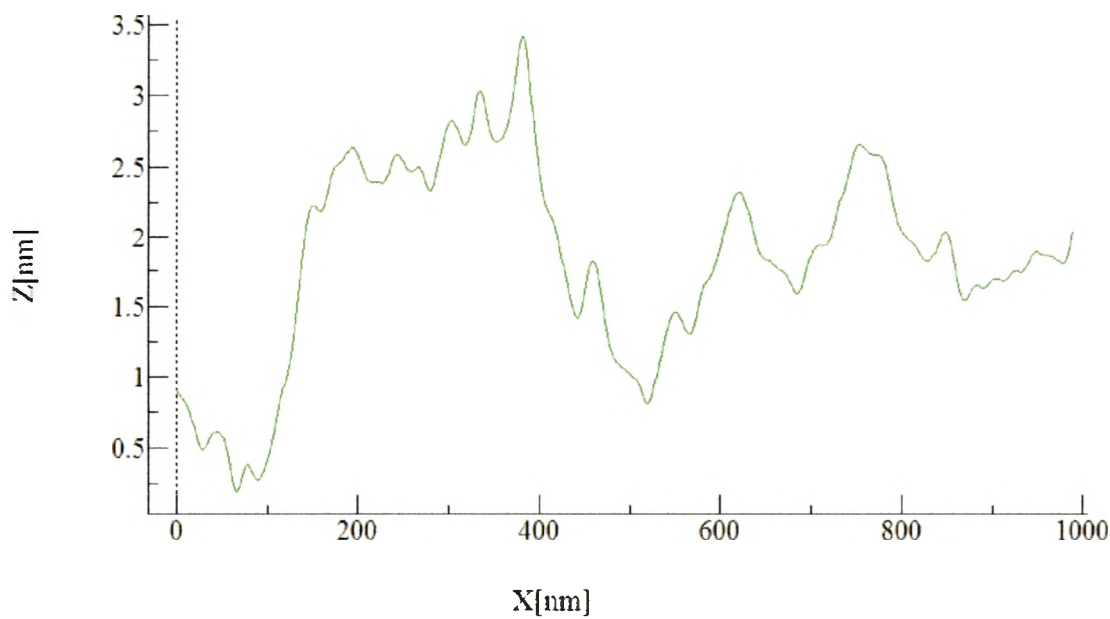
78. 3-D AFM Surface Image of Nylon 6 at 5 % Clay Loading at Time 1 Hour.



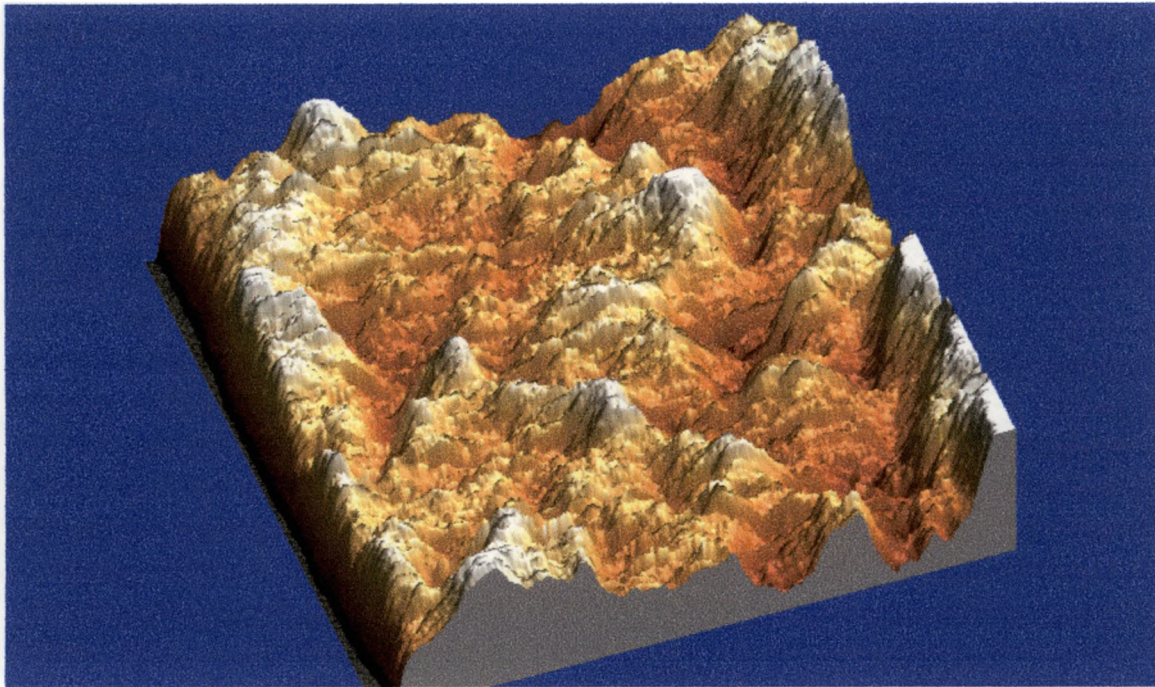
79. 2-D AFM Surface Image of Nylon 6 at 5 % Clay Loading at Time 1 Hour, green and blue lines represent topographical surface measurement.



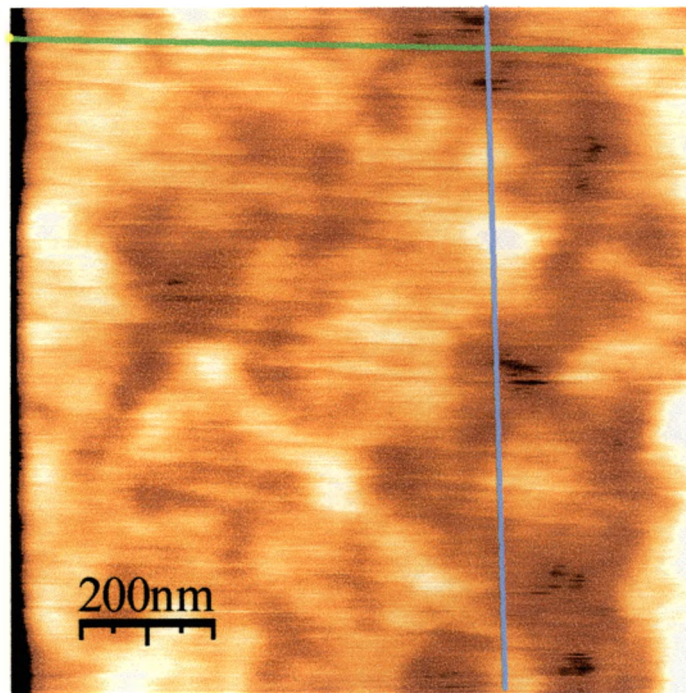
80. Topographical analysis of Nylon 6 at 5 % Clay Loading at Time 1 Hour, the graph represents the green line of 79.



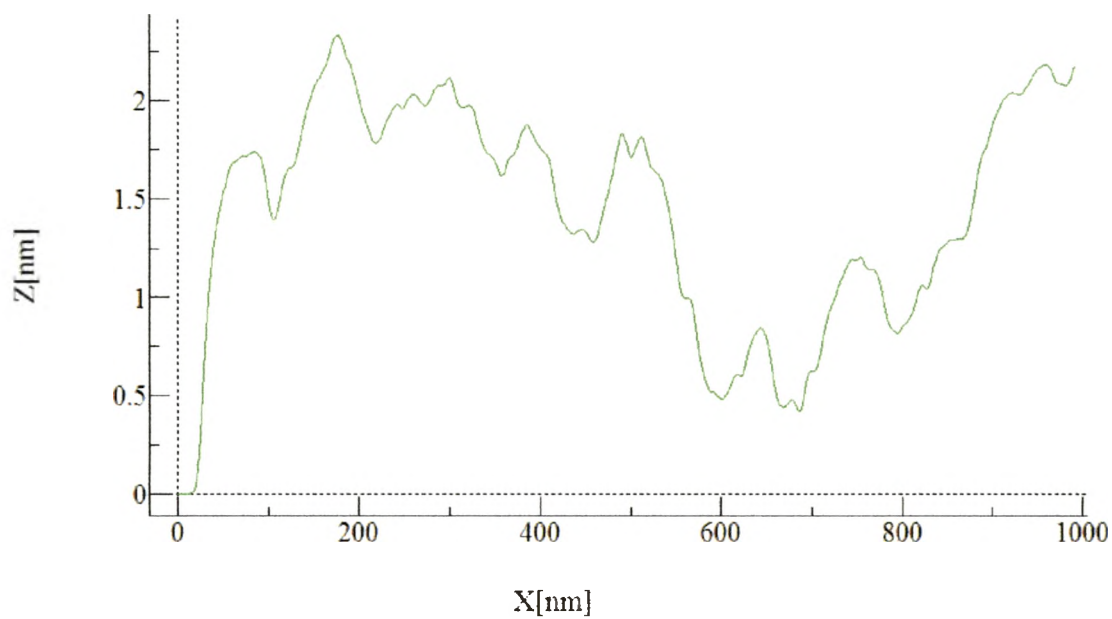
81. Topographical analysis of Nylon 6 at 5 % Clay Loading at Time 1 Hour, the graph represents the blue line of 79.



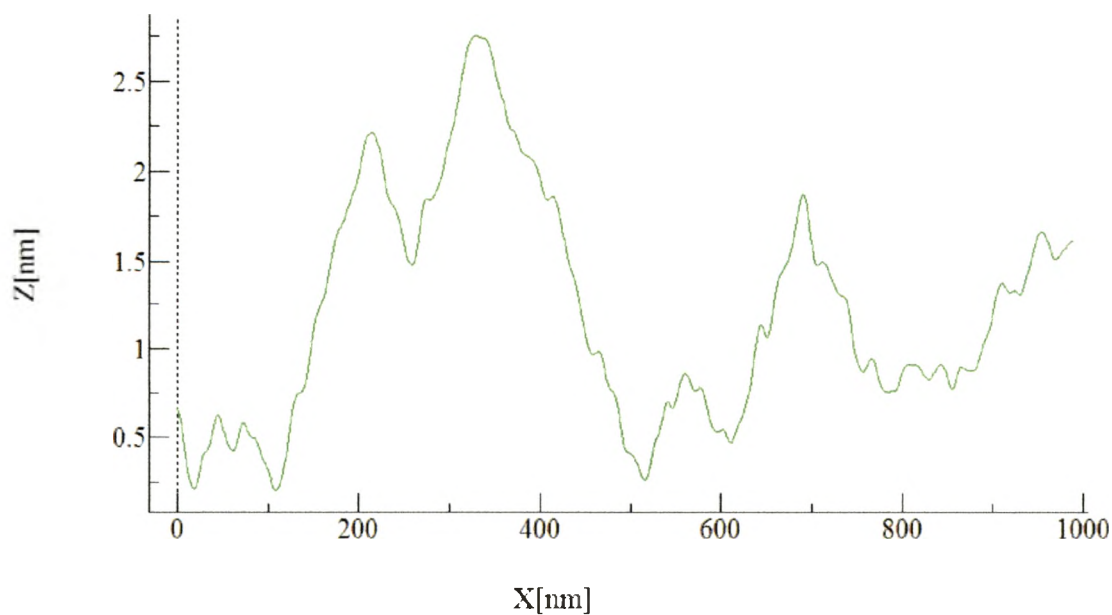
82. 3-D AFM Surface Image of Nylon 6 at 5 % Clay Loading at Time 2 Hours.



83. 2-D AFM Surface Image of Nylon 6 at 5 % Clay Loading at Time 2 Hours, green and blue lines represent topographical surface measurement.



84. Topographical analysis of Nylon 6 at 5 % Clay Loading at Time 2 Hours, the graph represents the green line of 82.



85. Topographical analysis of Nylon 6 at 5 % Clay Loading at Time 2 Hours, the graph represents the blue line of 82.

REFERENCES

1. Giannelis, E.P.; *Appl. Organometal. Chem.* **1998**, 12, 675-680.
2. Liu, X.; Wu, Q.; *Macromol. Mater. Eng.* **2002**, 3, 287.
3. Tortora, M.; Gorrasi, G.; Vittoria, V.; Galli, G.; Ritrovati, S.; Chiellini, E.; *Polymer.* **2002**, 43, 6147-6157.
4. Theng, B. K. G.; *Formation and properties of clay-polymer complexes*, Elsevier, Amsterdam, **1979**, pp 133.
5. Shephard, P.D.; Golemba, F.J.; Maine, F.W.; *Adv. Chem. Ser.* **1974**, 134, 41.
6. Fujiwara, S.; Sakamoto, T.; T. Japanses patent Application No. 109998 (1976) (assigned to Unichika K.K., Japan).
7. Okada, A.; Kawasumi, M.; Usuki, A.; Kojima, Y.; Kurauchi, T.; Kamigaito, O; *Mater. Res. Soc. Proc.* **1990**, 171, 45.
8. Pinnavaia, T.J.; Beall, G.W.; *Polymer-Clay Nanocomposites*, Wiley: New York, 2000, pp 267-279.
9. Messersmith, P.B.; Giannelis, E.P.; *J. Polym. Sci. Polym. Chem.* **1995**, 33, 1047.
10. Gilman, J.W.; *Appl. Clay Sci.* **1999**, 15, 31.
11. Lan, T.; Pinnavaia, T.J.; *Chem. Mater.* **1994**, 6, 2216.
12. Gaudel-Siri, A.; Brocorens, P.; Siri, D., Gardebien, F.; Bredas, J.L.; Lazzaroni, R.; *Langmuir* **2003**, 19, 8287.
13. Endell, K.; Hofmann, U.; Wilm, D.; *Ber. Dtsch. Kerman Ges.* **1933**, 14, 407-438.
14. Hofmann, U.; Endell, K.; Wilm, D.; *Z Kristallogr* **1933**, 86, 340-348.
15. Hofmann, U.; Endell, K.; Wilm, D.; *Angew. Chem.* **1934**, 47, 539-558.
16. Theng, B.K.G.; *Formation and Properties of Clay-Polymer Complexes*, Elsevier Scientific Publishing Company: Amsterdam, 1979, pp 10-14.

17. Fornes, T.D.; Paul, D.R.; *Polymer* **2003**, *44*, 4993.
18. Sinha, R.S.; Okamoto, M.; *Prog. Polym. Sci.* **2003**, *28*, 1539-1641.
19. Grim, R.E.; *Clay Mineralogy*, 1968 New York.
20. Xavier K.; (Division of Polymer Engineering). Lulea University of Technology.
21. Gant, F.M.; Brunk, H.A.; Kota, A.K.; *Journal of Composite Material.* **2004**, *38*, 1873.
22. Caeff.ces.clemson.edu “Nanocomposite Polymer Film Technology” – [Website]. Copyright 2005
<https://caeff.ces.clemson.edu/education/reuprog/reu/posters00/bonner.pdf>
[Accessed June 21, 2006].
23. Azom.com. “Clay-Based Nanocomposites.” – [Website]. Copyright 2000-2006.
<http://www.azom.com/details.asp?ArticleID=936> [Accessed May 20, 2006].
24. Neilsen, L.E.; *J. Macromol. Sci.* **1967**, *5(A1)*, 929 .
25. Bhaskar, A.; Master of Science Thesis, University of Florida, **2003**.
26. Lan, T.; Karviratna, P.D.; Pinnavaia, T.J.; *Chem. Mater.* **1994**, *6*, 572.
27. Gu, J.; Master of Science Thesis, Michigan State University, **1997**.
28. Spurr, A.R.; *J. Ultrastructure Res.*, **1969**, *26*, 311.
29. 2SPI.com “SPI-Chem™ Low Viscosity "Spurr" Kits” – [Website]. Copyright 2006.
http://www.2spi.com/catalog/chem/instructions_spurr_kits.html [Accessed May 1, 2006].
30. Kojima, Y.; Matsuoka, T.; Takahashi, H.; Kurauchi, T.; *J. Appl. Polym.* **1994**, *51* 683.
31. Kojima, Y.; Usuki, A.; Kuwasumi, M.; Okada, A.; Fukushima, Y.; Kurauchi, T.; Kamigaito, *J. Mater Res.* **1996**, *8* 1185.
32. Mathias, L.J.; Davis, R.D.; Jarrett, W.L.; *Macromolecules* **1999**, *32*, 7958.
33. Liu, L.; Qi, Z.; Zhu, X.; *J. Appl. Poly. Sci.* **1999**, *71*, 1133.
34. Liu, X.; Wu, Q, W.; Berglund, L.A.; Qi, Z.; *Macromol. Mater. Eng.* **2002**, *287*, 515.
35. Wu, Q.; Liu, X.; Berglund, L.A.; *Macromol. Rapid Commun.* **2001**, *22*, 1438.

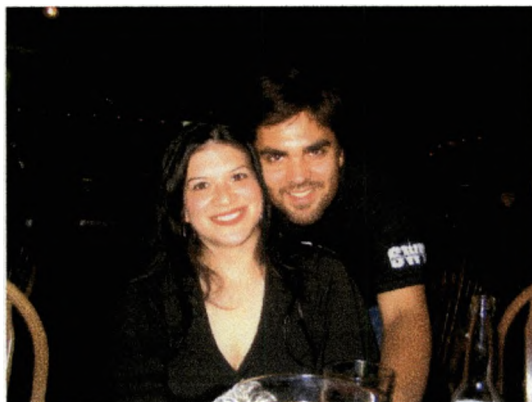
36. Holmes, D.R.; Bunn, C.W.; Smith, D.J.; *J. Polym. Sci.* **1955**, 17, 159.
37. Arimoto, H.; Ishibashi, M.; Hirai, M.; Chatani, Y.; *J. Polym. Sci.* **1965**, 3, 317.
38. Malta, V.; Cojazzi, G.; Fichera, A.; Ajo, D.; Zanetti, R.; *Eur Polym. J.* **1979**, 15, 765.
39. Salem, D.R.; Weighmann, H.D.; *Polym. Commun.* **1989**, 30, 336.
40. Murthy, N.S.; Minor, H.; *Polym. Commun.* **1991**, 32, 297.
41. Youyong, L.; Goddard, W.A.; *Macromolecules* **2002**, 35, 8440.

VITA

Daniel Adame was born in McAllen, Texas, on June 1, 1979, the son of Santiago Adame Hernandez and Evangelina Luna de Adame and the sibling of Karina Yvette Adame, Jesus Santiago Adame, and David Adame. After graduating from La Joya High School in La Joya, Texas, in 1997, he entered The University of Texas-Pan American in Edinburg, Texas. He later attended Southwest Texas State University in San Marcos and received the degree of Bachelor of Science in Chemistry in May of 2004. He entered the Graduate College at Texas State University-San Marcos in August of 2004.

Permanent Address: 167 Scott Lane

Mission Texas, 78572



This thesis was typed by Daniel Adame.